Germline biallelic mutation affecting the transcription factor Helios causes pleiotropic defects of immunity

Shahin, Tala

2021-11

Shahin , T , Kuehn , H S , Shoeb , M R , Gawriyski , L , Giuliani , S , Repiscak , P , Hoeger , B , Petronczki , O Y , Bal , S K , Zoghi , S , Dmytrus , J , Seruggia , D , Castanon , I , Rezaei , N , Varjosalo , M , Halbritter , F , Rosenzweig , S D & Boztug , K 2021 , ' Germline biallelic mutation affecting the transcription factor Helios causes pleiotropic defects of immunity ' , Science immunology , vol. 6 , no. 65 , 3981 . https://doi.org/10.1126/sciimmunol.abe3981

http://hdl.handle.net/10138/352881
https://doi.org/10.1126/sciimmunol.abe3981

unspecified
acceptedVersion

ScienceImmunology

template updated: July 5 2016

Title: Germline biallelic mutation affecting the transcription factor Helios causes pleiotropic defects of immunity

Authors: Tala Shahin,[1,2,3,4] Hye Sun Kuehn,[5] Mohamed R. Shoeb,[1] Lisa Gawriyski,[6] Sarah Giuliani,[1,2] Peter Repiscak,[1] Birgit Hoeger,[1,2] Özlem Yüce Petronczki,[1,2] Sevgi Köstel Bal,[1,2] Samaneh Zoghi,[1,2] Jasmin Dmytrus,[1,2] Davide Seruggia,[1] Irinka Castanon,[1] Nima Rezaei,[7,8,9] Markku Varjosalo,[6] Florian Halbritter,[1] Sergio Rosenzweig,[5] Kaan Boztug[1,2,3,4,*]

Affiliations:

[1]St. Anna Children's Cancer Research Institute (CCRI), Vienna, Austria

[2]Ludwig Boltzmann Institute for Rare and Undiagnosed Diseases, Vienna, Austria

[3]CeMM Research Center for Molecular Medicine of the Austrian Academy of Sciences, Vienna, Austria

[4]Department of Pediatrics and Adolescent Medicine, Medical University of Vienna, Vienna, Austria

[5]Immunology Service, Department of Laboratory Medicine, Clinical Center, National Institutes of Health, Bethesda, Maryland, 20814, USA

[6]Institute of Biotechnology, Helsinki Institute of Life Science, Proteomics Unit, University of Helsinki, Helsinki, Finland

[7]Research Center for Immunodeficiencies, Children's Medical Center, Tehran University of Medical Sciences, Tehran, Iran

[8]Department of Immunology, School of Medicine, Tehran University of Medical Sciences, Tehran, Iran

[9]Network of Immunity in Infection, Malignancy and Autoimmunity (NIIMA), Universal Scientific Education and Research Network (USERN), Tehran, Iran

*Corresponding author. Email: kaan.boztug@ccri.at (K.B.)

One sentence summary: Biallelic germline mutation affecting Helios disrupts interactions with epigenetic remodelers, leading to an altered T-cell transcriptional state and immunodeficiency.

Abstract

Helios, a member of the Ikaros family of transcription factors, is predominantly expressed in developing thymocytes, activated T cells and regulatory T cells (T_{regs}). Studies in mice have emphasized its role in maintenance of T_{reg} immunosuppressive functions through stabilizing *Foxp3* expression and silencing the *Il2* locus. However, its contribution to human immune homeostasis and the precise mechanisms by which Helios regulates other T-cell subsets remain unresolved. Here, we investigate a patient with recurrent respiratory infections and hypogammaglobulinemia and identify a germline homozygous missense mutation in *IKZF2* encoding Helios (p.Ile325Val). We show that Helios^{I325V} retains DNA-binding and dimerization properties, but loses interaction with several partners, including epigenetic remodelers. We find that while patient T_{regs} show increased IL-2 production, patient conventional T cells have decreases accessibility of the *IL2* locus, and consequently reduced IL-2 production. Reduced chromatin accessibility is not exclusive to the *IL2* locus, but involves a variety of genes associated with T-cell activation. Indeed, single-cell RNA-sequencing of peripheral blood mononuclear cells revealed gene expression signatures indicative of a shift towards pro-inflammatory, effector-like status in patient $CD8^+$ T cells.

Moreover, patient $CD4^+$ T cells exhibited a pronounced defect in proliferation with delayed expression of surface check-point inhibitors, suggesting an impaired onset of the T-cell activation program. Collectively, we identified a novel germline-encoded inborn error of immunity and uncovered a cell-specific Helios-dependent epigenetic regulation. Binding of Helios with specific partners mediates this regulation, which is ultimately necessary for the transcriptional programs that enable T-cell homeostasis in health and disease.

Introduction

The Ikaros family of transcription factors comprises five members, Ikaros (encoded by *IKZF1*), Helios (*IKZF2*), Aiolos (*IKZF3*), Eos (*IKZF4*) and Pegasus (*IKZF5*). Three of these zinc finger proteins, Ikaros, Helios and Aiolos, have been shown to be involved in the intricate gene-regulatory network that governs hematopoiesis, cell-fate decisions and cellular function, particularly in cells of the adaptive arm of immunity (*1*, *2*). As transcription factors, they bind to their consensus DNA sequences through N-terminal zinc finger domains, whereas homodimerization and heterodimerization to other family members is facilitated by the two C-terminal zinc finger domains (*3*). In addition, they bind and recruit other transcriptional modulators as well as chromatin modifiers, such as the nucleosome remodeling (NuRD) complex (*4*, *5*). These interactions mediate their activating and repressive effects on target genes, including lineage-defining factors and cell cycle regulators (*4*).

While being expressed broadly in hematopoietic cells, several studies using different mouse models have revealed a critical role for Ikaros and Aiolos in the regulation of B-cell differentiation, activation and proliferation (*6–9*). Ikaros has additionally been shown to play an important role during T- and NK-cell development (*10–12*). Helios, on the other hand, is primarily expressed in

T cells, particularly in developing thymocytes, activated T cells, regulatory T cells (T_{regs}) and mucosa-associated invariant T (MAIT) cells (*13–19*). In both mice and humans, approximately 70-80% of the T_{reg} pool expresses Helios (*20*). Thornton et al. have shown that in mice, Helios$^+$ T_{regs} have more stable Foxp3 expression, thereby maintaining T_{reg}-specific demethylated regions and supporting full suppressive capacity (*21*). In line with this, mice with a conditional deletion of Helios in T_{regs} eventually developed systemic autoimmunity as a result of a reduction in the viability and stability of Helios-deficient T_{regs} due to increased apoptosis and defective T_{reg} effector functions (*22*, *23*).

Helios is upregulated upon CD4$^+$ and CD8$^+$ T-cell activation and proliferation in both murine and human cells, suggesting roles beyond T_{regs} (*15*, *19*, *24*). Yet, despite the almost complete early postnatal lethality of Helios null mice, viable adult mice were smaller in size, but had no defects in T-cell or T_{reg}-cell development or function (*25*). It has been suggested that other Ikaros family members can compensate for the Helios deficiency in developing thymocytes. On the other hand, the lack of Helios in activated T cells might be balanced by its loss in T_{regs}, explaining the absence of an overt immune activation in these mice (*26*). While all these studies have been informative, the precise roles of Helios in different immune cell subsets together with its contribution to human disease remain elusive.

Human germline autosomal dominant mutations in *IKZF1* have been identified, leading to a spectrum of clinical manifestations. Mutations in the DNA-binding or dimerization domains of Ikaros, leading to haploinsufficiency, were associated with loss of B cells and concomitant hypogammaglobulinemia, a predisposition to B-cell acute lymphoblastic leukemia and/or autoimmunity (*27–31*). Dominant-negative mutations were found to be more severe, with profound defects in T cells and myeloid cells (*32*). Very recently, two patients with a germline

monoallelic mutation in *IKZF3* have been reported, demonstrating impaired Ikaros function, hence phenocopying B-cell defects characteristic of patients with dominant negative mutations in *IKZF1* (*33*). Here, we characterize a previously unknown, inborn errors of immunity caused by a biallelic missense mutation in *IKZF2,* identified in an immunodeficient patient with T-cell aberrations. We study the pathobiological consequences of the germline *IKZF2* mutation and identify impaired interaction of Helios with several chromatin remodelers and transcription factors, resulting in global epigenetic changes translating to aberrant T-cell phenotype and function.

Results

Identification of a homozygous missense variant in *IKZF2*

We studied a 17-year-old Iranian male index patient who was born to a consanguineous family (Fig. 1A). He has a failure to thrive, with a very low body weight of 20 kg and a short stature (112 cm), both measured at the age of 13 (body mass index (BMI) Z-score of -2.11, below the 3rd percentile). He consistently suffered from joint pains, where a radiography of the left wrist at the time showed evidence of osteopenia with fraying of the distal ulna and radius, and a bone age of 9.5 years. He was additionally diagnosed with hypothyroidism and is on substitution therapy. The patient has a history of recurrent infections, including sinusitis, otitis media and lower respiratory tract infections with productive coughs and bronchiectasis, leading to multiple pneumonias that were accompanied by fevers, and required several hospitalizations since childhood. For the majority of these infectious episodes, no causative agent was isolated, however the patient benefited from antibiotics. Lab results indicated consistent leukopenia (white blood cell count of 2.89 g/l, reference: 4-11 g/l) and hypogammaglobulinemia with low antibody titers against Tetanus and Diphtheria vaccinations (table S1), for which he is given a monthly dose of intravenous

immunoglobulin (IVIG). No autoantibodies were present (table S1) and both direct and indirect Coombs tests were negative.

To investigate the underlying molecular etiology in our patient, we performed whole exome sequencing (WES) as well as segregation analysis and identified a homozygous missense variant in the *IKZF2* gene (ENST00000457361.1:c.973A>G, ENSP00000410447.1:p.Ile325Val), encoding the Helios transcription factor (Fig. 1B and table S2). The variant lies in the region between the two main zinc finger domains of the protein, the DNA binding domain and homo/heterodimerization domain (Fig. 1C). Genome3D (*34*) predicts this region to contain another non-classical zinc finger domain (FYVE/PHD or Zinc/RING finger) with high confidence (90%) where the variant lies, that could play a role in the mediation of specific protein interactions (*35*). There have been no reported homozygous cases of this variant in the gnomAD (*36*) database (last accessed 14.07.2021). The missense variant is predicted damaging according to functional prediction tools (table S2), and notably the isoleucine at that particular position is highly conserved across species (Fig. 1D). As a measurement of intolerance to loss-of-function mutations, the pLI score (*37*) of *IKZF2* is extremely high (0.99), indicating essentiality of this gene. Collectively, this suggested that the p.I325V homozygous variant in Helios has a high possibility for being disease causing.

Aberrant immune cell phenotype

To investigate the consequences of the germline *IKZF2* mutation on immune cell subset composition, we performed immune phenotyping on patient peripheral blood mononuclear cells (PBMCs) at 13 and 14 years of age. We observed a marked reduction of relative and absolute numbers of both B ($CD19^{+}$) and NK ($CD3^{-}CD19^{-}CD16^{+}CD56^{dim}$) cells (Fig. 2A), with an apparent

progressive decline in B-cell counts over time (table S1). When evaluating the patient B-cell subsets, we noted a reduction in the frequencies of class-switched (CSM) and non-switched memory (non-SM) B cells as well as plasmablasts, with a higher frequency of transitional B cells, indicative of a B-cell maturation defect (Fig. 2B and fig. S1). In addition, the innate-like $CD19^{+}CD38^{lo}CD21^{lo}$ B-cell subset, typically expanded in chronic immune stimulation, was remarkably higher in the patient (fig. S1) (*38*). Within the T-cell fraction, we observed a reduction in $CD4^{+}$ T cells, with an inverted CD4/CD8 ratio (Fig. 2, A and C, fig. S2A and table S1). While the frequency of naïve and memory T cells within the patient's $CD4^{+}$ population were within normal range, $CD8^{+}$ T cells were predominantly effector memory ($CD45RA^{-}CCR7^{-}$; mean of 73% in patient vs. 25% in controls) that expressed a high level of CD57, indicative of their terminally differentiated state (*39*) (Fig. 2, C and D and fig. S2A). Consistent with this, we observed a concomitant shift to highly differentiated $CD8^{+}CD27^{-}CD28^{-}$ T cells in the patient (fig. S2A). On the other hand, patient T_{regs} (gated on both $CD127^{-}CD25^{+}FOXP3^{+}$ and $CD25^{+}FOXP3^{+}$) were present and showed normal expression of Helios, albeit in a lower abundance within the $CD4^{+}$ T-cell population compared to controls (mean of 1.56% vs. 5.00%; Fig. 2E and fig. S2B). T-follicular helper cells (T_{fh}) of the patient were within normal range (Fig. 2F and fig. S3A), however the frequencies of other T-cell populations were altered, with a higher frequency of γδ T cells in the patient (Fig. 2G and fig. S3A). We noted a reduced frequency of the innate-like, invariant natural killer T cells (iNKT) and mucosa-associated invariant T cells, in line with Hetemäki and colleagues' data on two patients with a heterozygous Helios (p.R200X) mutation (Fig. 2G and fig. S3B). Given the evident aberrations in the frequencies of several immune subsets leading to the combined immunodeficiency in the index patient in our study, we next sought to investigate the molecular mechanisms by which the biallelic variant in *IKZF2* affects protein function.

Functional and biochemical assessment of Helios^{I325V}

To assess the effects of the p.I325V mutation on the ability of Helios to bind DNA, we performed a chemiluminescent electromobility shift assay (EMSA). Nuclear extracts from the human embryonic kidney cell line, HEK293T, overexpressing wild-type (Helios^{WT}) or mutant Helios (Helios^{I325V}), were incubated with DNA probes containing an Ikaros consensus-binding sequence (IK-bs1), including the canonical motif GGGAA, to which Helios also binds (*14*, *40*). Both Helios^{WT} and Helios^{I325V} showed a similar level of dimer and multimer formation on the IK-bs1 probe (Fig. 3A). We next sought to visualize the binding of the Helios^{WT} and Helios^{I325V} to pericentromeric heterochromatin (PC-HC) regions and assess their cellular localization by immunofluorescence staining in NIH3T3 murine fibroblast cells. Images show the ability of Helios^{I325V} to localize to the nucleus and form a similar number of foci at PC-HC regions compared to Helios^{WT} (Fig. 3B). Therefore, we concluded that the p.I325V in Helios does not alter its DNA-binding capacity.

We next assessed the ability of Helios^{I325V} to form dimers with the WT or mutant counterpart, as well as to other members of the Ikaros family, by co-immunoprecipitation experiments. Helios^{I325V} was able to form homo- and heterodimers with Ikaros, Aiolos and Eos (Fig. 3C and fig. S4A). As the mutation does not lie in either the DNA-binding or the dimerization domains, the functional intactness of these two domains is expected. Yet, in the process of activating or repressing genes, Helios also binds to other transcription factors and chromatin modifiers, including members of the nucleosome remodeling (NuRD) complex such as histone deacetylase 1 (HDAC1) (*5*). Indeed, co-immunoprecipitation experiments revealed a marked reduction in the ability of Helios^{I325V} to bind to HDAC1 (Fig. 3D). As SUMOylation of Ikaros participates in the regulation of HDAC binding

(*41*), the SUMOylation of Helios by SUMO2 was assessed after overexpressing a SUMO2 construct with Helios^{WT} or Helios^{I325V} in HEK293T cells. Analysis by Western blot showed no defect in SUMOylation (fig. S4B). Hence, the loss in HDAC1 binding caused by the missense mutation could be due to steric hindrance, leading to our subsequent evaluation of the effects of Helios^{I325V} on all protein interactions.

Helios^{I325V} leads to disrupted interactions with epigenetic remodelers

The mediation of appropriate interactions between transcription factors and chromatin remodelers at required genomic loci during different stages of cell development is crucial for transcriptionally priming cells into a particular fate (*4*, *42*). As many interactions are transient, or require the assembly of several proteins or complexes together, we sought to probe all these interactions by using BioID-MS, a biotinylation-proximity labelling technique, coupled with liquid chromatography mass spectrometry (LC-MS) (*43*, *44*). Moreover, given the loss of binding of Helios^{I325V} to HDAC1 (Fig. 3D), we wanted to globally identify the disrupted interactions caused by the mutation. Complementing previous attempts that identified direct physical interaction partners of Helios (*5*), here we expanded Helios' interactome with 170 dynamic interactors following stringent statistical analysis (SAINTexpress, Bayesian false discovery rate (BFDR) < 0.05). We performed enrichment analysis to reveal enriched protein complexes from the complex database CORUM (Fisher's exact test, p.adjust < 0.05) (*45*)(fig. 4A and table S3). As expected, the majority of interactors consisted of transcription factors and histone modifiers, including known interactors from the NuRD complex (*5*). We also identified unknown interactions with members of the ATAC complex of histone acetyltransferases, and with proteins involved in cell

cycle regulation and cell division (PLK1 and GTSE1) as well as DNA repair (NIPBL, BLM, BRCA1 and BRCA2) (Fig. 4A).

Comparing the detected interactors from Helios^{WT} to those of the mutant, we found that Helios^{I325V} gains 11 interactors, loses 39 and has significantly ($p<0.05$, Student's t-test) reduced association to 17 proteins (depicted by different colors in Fig. 4A). Lost interactors included histone remodelers, such as HDAC3, GATAD2A, GATAD2B, KMT2D and components of the ATAC complex (TADA2A, KAT2A and SGF29), as well as cell cycle regulators, including GTSE1 and PLK1 (Fig. 4, A and B, and fig. S5). Enrichment analysis using Gene Ontology terms (*46*) indicated deregulation of transcription, histone acetylation, DNA methylation, cell cycle and DNA repair caused by the mutant (Fig. 4C and fig. S6). Quantitative analysis of the interactome data using MaxQuant software confirmed that the mutant protein significantly loses interaction with the cell cycle regulators BRCA1 and GTSE1, and shows significantly reduced cooperation with several transcriptional and chromatin regulators (fig. S7, A and B and table S3). Collectively, this suggests that although the p.I325V mutation lies outside of Helios zinc finger domains, with DNA-binding and dimerization abilities remaining intact, specific Helios functions might be affected through an altered interactome; this is either due to a disruption in physical interactions or in the recruitment of Helios, or its partners, to the required genomic loci. Therefore, defects in the epigenetic regulation of particular loci are highly plausible, ultimately leading to transcriptional deregulation.

RNA sequencing reveals changes in transcriptional states of immune cell populations

Given the disturbance in the protein interaction network caused by Helios^{I325V}, we sought to systematically assess transcriptional changes that could culminate in the different cellular states

observed in the patient's lymphocytes. We performed droplet-based scRNA-seq on PBMCs from the patient, taken at 14 years of age. For comparison, we included PBMCs from four healthy controls, comprising two adults (C1, male; C2, female) and two age-matched controls (C3, male; C4, female). This analysis yielded a total of 25,081 cells passing quality control (table S4). Low-dimensional projection using uniform manifold approximation and projections (UMAP) (*47*) and graph-based clustering confirmed the presence of the expected PBMC populations (Fig. 5A, fig. S8 and table S5). Based on the expression of known marker genes, we label meta-cluster 1 as a monocyte cluster (*CD68*), meta-cluster 2 as a T and NK-cell cluster (*CD3D*/*E* and *KLRB1*), cluster 3 as B cells (*CD79A*), cluster 4 as myeloid dendritic cells (DCs; *CLEC10A*) and cluster 6 as plasmacytoid DCs (*GZMB*; fig. S9A). Subpopulations of meta-clusters were further characterized (fig. S8). As for T cells, we show that cells of cluster 2a identify as naïve T cells (*CCR7* and *TCF7*), whereas cells of clusters 2b and 2c express genes associated with an NK-cell, central memory or effector T-cell phenotype (*GZMH*, *CTSW*, *NKG7* and *KLRD1*).

With respect to lymphocytic cell frequencies, we observed an almost complete absence of patient cells in the B-cell cluster 3 (Fig. 5B and fig. S9B). Moreover, a skewing of the patient T cells towards clusters 2b and 2c, and a loss of 2a, is apparent (fig. S9B). Both observations corroborate our previous findings based on flow cytometry (Fig. 2, A and C). Differential gene expression analysis (pairwise MAST (*48*); adj. $p \leq 0.05$, $|\log FC| \geq 0.25$; table S6) between the patient and control cells within the constituent clusters of meta-clusters 1 (i.e., 1a and 1b) and 2 (i.e., 2a, 2b and 2c) was performed (Fig. 5C, fig. S10, A-C and table S6). This analysis revealed an upregulation of genes associated with inflammation, indicating that both monocytes and T cells are in an activated and effector state. For instance, within the effector T-cell and NK-cell cluster 2c, these genes include multiple components of the TCR activation complex (*CD8A*/*B*, *CD3D/G,*

CD2 and *CD6*), the pro-inflammatory genes *GZMH*, *IL32* and *CCL5*, an interferon-related antiviral gene, *ISG20*, as well as glycolytic pathway genes *PGK1* and *LDHA*. In addition, anti-inflammatory genes *TSC22D3*, *TNFAIP3* and *ZFP36* were upregulated, possibly as an auto-regulatory consequence to the inflammatory response.

In contrast to the above, the "naïve T-cell" cluster 2a showed a paucity of patient cells (Fig. 5, B and fig. S9B). However, the isolated patient-centric cluster 5 was shown to express genes present in cluster 2a, suggesting that they are naïve $CD4^+$ T cells of the patient (Fig. 5, A and B and fig. S8). We confirmed this assumption by performing a principal component analysis that clearly grouped cells from cluster 5 to the "naïve" T-cell cluster 2a (fig. S9C). Analysis of the top differentially regulated genes between clusters 2a and 5 identified eight upregulated genes (Fig. 5D, and table S6). The anti-inflammatory gene *TSC22D3* is upregulated in cells of cluster 5 as well, suggesting maintenance of a suppressive state. This state is further supported by the elevated expression of protein phosphatases *DUSP1* and *PPP1R15A,* which play a role in dampening the mitogen-activated protein kinase (MAPK) pathway and protein translation, respectively (*49*, *50*). Upon induction by glucocorticoids, *TSC22D3*, encoding GILZ (glucocorticoid-induced leucine zipper), plays a key role in the inactivation of pathways including NFκB (*51*). We noted that the patient has not been administered any glucocorticoids before blood sampling. Interestingly, GILZ has also been shown to be induced under IL-2 deprivation, and functions to prevent apoptosis (*52*). This is consistent with the upregulation of the anti-apoptotic gene *BCL2* in cells of cluster 5. Therefore, besides the confirmed loss of B cells, transcriptomic analysis of the patient lymphocytic population revealed an increase in the inflammatory state of the predominant effector $CD8^+$ T-cell population, while pointing to a suppressed naïve $CD4^+$ T-cell population.

To analyze rare naïve B cells and T_{regs} in the patient peripheral blood, we sorted naïve B cells ($CD19^+CD27^-IgD^+$) and T_{regs} ($CD4^+CD25^{hi}CD127^-$) and performed transcriptome analysis using SMART-seq in the patient compared to three sex-matched controls (table S7) (*53*). Differential analysis identified a total of 584 differentially regulated genes in naïve B cells (Fig. 5E and table S8). Pathway analysis of the 385 upregulated genes confirmed the patient proinflammatory state, including increased granulocyte migration/chemotaxis and an upregulation of both the IL-8 cytokine pathway (*CXCL8*, *CXCL3*, *CCL4* and *CCL3*), and the pattern recognition receptor signaling (*TLR2*, *FCN1* and *FFAR2*) (fig. S11A and table S9). Conversely, pathways with the 199 downregulated genes indicated maturation defects of the patient B cells, with B-cell receptor activation as one of the top results (fig. S11A and table S9). Downregulated genes involve several immunoglobulin heavy and light chain genes, including *IGHV1-69*, *IGHV3-48*, *IGHV1-24*, *FCGR2C*, *IGLC3* and *IGLC2*, as well as the pre-B-cell receptor surrogate light chain, lambda-5 (encoded by *IGLL1)*, which is critical for B-cell development.

As previously mentioned, Helios is involved in maintaining the immunosuppressive role of T_{regs} by stabilizing Foxp3 (*21*). We found that 874 genes were differentially expressed in T_{regs} of the patient compared to healthy controls, of which 820 genes were downregulated (Fig. 5F). Of these, 83 genes (9.5%), such as *RPTOR*, *BCL6*, *CITED2* and *WDR5* had previously shown to be regulated by FOXP3 in T_{regs} (table S8 and S9) indicating compromised T_{reg}-cell identity (*54*). Several genes involved in epigenetic and chromatin regulation were additionally found to be significantly reduced in the patient T_{reg} cells (*KDM2B*, *KDM3A*, *KDM7A*, *KMT2B*, *EP300*, *WDR5*, *KANSL3* and *KANSL1L*), some of which we have shown significantly lose binding to $Helios^{I325V}$ (*KMT2D, GATAD2A* and *GATAD2B*) (Fig. 4A and table S8). These widespread transcriptional disturbances in the T_{regs} prompted us to assess their ability to repress the production of pro-inflammatory

cytokines upon T-cell stimulation. In line with Kim et al. (*22),* we noted an increase in the production of IL-2 and IFNγ by T_{regs} of the patient compared to controls, confirming the proinflammatory and dysregulated state of the patient identified in our RNA-seq data (Fig. 5G and fig. S11B).

Defective proliferation and IL-2 production by patient T cells

To investigate the deleterious effects of the mutation on patient T cells, as indicated by their dysregulated transcriptome, we performed a series of *in vitro* experiments to functionally assess T cell activation responses. We first measured the proliferative capacity of patient T cells by stimulating the TCR with CD3/CD28 beads and monitoring the dilution of a proliferation marker. We observed a defect in the ability of the patient's $CD4^+$ and $CD8^+$ T cells to proliferate by the third day compared to the healthy sister and unrelated controls (mean of 30.3% vs. 80.0-87.0% and 7.8% vs. 54.0-78.0% proliferated cells, respectively; Fig. 6, A and B, and fig. S12). Yet, in patient $CD4^+$ T cells, this stimulation led to a normal increase in the percentage of cells upregulating the activation marker CD25 (*IL2RA*) and Helios. No significant reduction of Helios expression was detected in the patient cells (Fig. 6C and fig. S12). Stimulation with an anti-CD3 monoclonal antibody (OKT3) alone or phytohemagglutinin (PHA) showed no proliferation in both $CD4^+$ and $CD8^+$ T cells of the patient at day 3, which was accompanied by a reduction in CD25 upregulation (fig. S14A, B and C).

By day 8 after stimulation with CD3/CD28 beads, patient $CD4^+$ T cells have proliferated (Fig. 6A, B and C and fig. S13). As Helios is upregulated upon T-cell activation and proliferation (*19*), we hypothesized a delay in the onset of a downstream transcriptional program in the patient T cells. To address this, we assessed the expression of exhaustion markers and check-point inhibitors, such

as PD-1, TIGIT, LAG3, TIM3 and AITR/GITR, which are typically upregulated upon TCR activation. Our results indicated no increase in the expression of these markers at basal level (Fig. 6D and fig. S13A and B). However, we observed a delay in their upregulation, particularly in the $CD4^+$ T cells of the patient, measured at day 2, day 4 and day 7 post-TCR activation (Fig. 6D and fig. S13A and B), alluding to dysregulated and delayed activation of the downstream transcriptional program upon TCR stimulation. This was confirmed using IL-2-dependent expanded T-lymphoblasts, where we excluded an upstream defect in proximal TCR signaling by performing intracellular calcium flux assay and assessing the phosphorylation of signaling molecules p65, p38 and ERK (fig. S14D and E). Only p-AKT, which is downstream of TCR, CD28 and IL-2 signaling, was not sufficiently increased upon stimulation with CD3/CD28 beads and IL-2 (fig. S14E).

We next assessed cytokine production upon T-cell stimulation that is further downstream and a result of transcriptional activation. After a 5-hour stimulation of PBMCs with PMA and ionomycin, we noticed a decrease in IL-2 producing $CD4^+$ and $CD8^+$ T cells (mean of 6.7% vs. 23.2% and 1.2% vs 26.9% in patient and controls cells respectively; Fig. 6E and fig. S15). However, production of T-helper cell specific cytokines, IFNγ, IL-4 and IL-17A, by $CD4^+$ T cells as well as IFNγ by $CD8^+$ T cells were unaffected (fig. S16A and B). Stimulation of patient PBMCs with CD3/CD28 beads also showed a reduction in IL-2 secretion into the supernatant when compared to controls (fig. 6F). To address whether this reduction in IL-2 production affects cellular apoptosis, we withdrew supplementary IL-2 given to sustain the growth of T-lymphoblasts. While all control cells initiated apoptosis within 24 hours, patient T-lymphoblasts showed higher levels of survival at this time-point (fig. 6G). Reduced capacity patient T-lymphoblasts to produce IL-2 was confirmed, upon PMA and ionomycin stimulation (fig. 6H). To

demonstrate causality of the Helios^{I325V} mutation in causing this phenotype, we generated CRISPR-Cas9 edited patient T-lymphoblasts, correcting the mutation in *IKZF2* and thus reconstituting it to wildtype (fig. S17A). We successfully generated one patient wildtype CD8^{+} clone (P-WT) and assessed its ability to produce IL-2 upon stimulation. Indeed, reconstitution of the patient mutation to wildtype rescued the defect in IL-2 production (Fig. 6H and fig. S17B), directly implicating the mutation in Helios (p.I325V) in the downstream control of the *Il2* locus in conventional T-cells. Collectively, the delay in the onset of proliferation and expression of check-point inhibitors, and defective IL-2 production as a result of Helios^{I325V}, indicated a dysregulation in the downstream transcriptional activation of genes ensuring full T-cell activation. As data from our proteomic analysis demonstrated that the mutation in Helios leads to a loss or gain of interactions to chromatin remodelers and transcriptional factors (Fig. 4A), we next decided to assess the changes in the epigenetic state of conventional T cells of the patient upon stimulation.

Epigenetic analysis of patient T cells identifies global chromatin changes due to Helios^{I325V}

In T$_{regs}$, Helios is known to repress the *Il2* locus by inducing deacetylation of core histones in the *Il2* promoter (*55*). In conventional T cells, in which Helios is upregulated upon T-cell activation, the concerted action of multiple chromatin remodelers and transcription factors, including NFAT and the AP-1 complex, is required to initiate transcription of *Il2*. Based on our previous observations, we hypothesized an increased repression of the *Il2* promoter in the patient T cells mediated by the loss of Helios^{I325V} interactions with activators of the *Il2* promoter, including members of the ATAC complex, such as GCN5, which has been shown to be involve in IL-2 production (*56*) (Fig. 4A). Therefore, we performed an assay for transposase-accessible chromatin with high-throughput sequencing (ATAC-seq) on T-lymphoblasts of the patient and two male

controls, upon stimulation with PMA and ionomycin for 2 hours, to initiate downstream epigenetic and transcriptional changes. Our analysis identified 21,627 peaks common to at least two samples ("consensus peaks") and 2,099 peaks unique to patient-derived T-lymphoblasts. As expected, the majority of all peaks (more than 35%) were found around promoter regions (within 1,000 base pairs of an annotated transcription start site) (fig. S18A and B). Focusing on consensus peaks at promoters, we identified 233 differentially accessible regions between patient and control T-lymphoblasts (abs(log2FC)>log2(1.5)), 141 of which had decreased accessibility compared to the controls (Fig. 7A, table S10). Enrichment analysis implicated many of the genes associated with these promoters in leukocyte adhesion and activation (Fig. 7B). Confirming our previous findings, we noted reduced accessibility of the *Il2* promoter in the patient T-lymphoblasts, indicating increased repression of this locus (Fig. 7A and C). Other promoters with reduced accessibility included genes involved in IL-2 signaling (e.g., *STAT5A*), as well as those involved in T-cell activation (e.g., *IL7R*, *CCR2*, *CRTAM*, *IFNG*, *TESPA1*, *CD44*, *ZAP70*, *TCF7*, *LY9*, *VAV1*, *CD7* and *IKZF2*; Fig. 7A, table S10). These data corroborate our findings on reduced IL-2 production caused by Helios^{I325V} in patient T cells, with an evident failure to open chromatin regions required for T-cell activation, which we speculate lead to the observed delay in proliferation. Collectively, these data strengthen a role for Helios in the transcriptional regulation of certain genomic loci downstream of TCR signaling in conventional T cells.

Discussion

We describe a novel human inborn error of immunity (IEI) caused by a homozygous missense mutation in *IKZF2*, encoding Helios, manifesting with combined immunodeficiency. Studies in murine model systems have shown Helios expression in developing thymocytes and subsets of the

T-cell lineage, including Tregs, MAIT cells and activated conventional $CD4^+$ and $CD8^+$ T cells (*13*, *14*). Consistent with this, the index patient in our study had profound T-cell defects, evidenced by $CD4^+$ T-cell lymphopenia, expansion of terminal-effector $CD8^+$ T cells, reduction in Tregs and absence of invariant T cells (iNKT and MAIT cells). Interestingly, despite the low expression of Helios in B cells (*13*, *14*), our patient also exhibited a progressive loss of B cells over time, accompanied with a reduction in peripheral memory B cells and plasmablasts, and an increase in transitional B cells, indicative of a B-cell maturation defect. Indeed, transcriptional analysis of the patient naïve B cells revealed a downregulation of genes involved in B-cell development and differentiation. Given the paucity of peripheral B cells in the patient, it was impossible (and beyond the scope of our study) to investigate in detail how the p.I325V mutation in Helios may affect B-cell maturation and/or development, and also to explore whether this is an intrinsic phenotype of $Helios^{I325V}$-mutant B cells or secondary to aberrant T-B interaction, for instance T follicular cells dysfunction.

The Ikaros family of transcription factors has key roles in hematopoiesis, immune cell development and homeostasis. The $Helios^{I325V}$ mutation is positioned between the two zinc-finger domains. Consistent with this, the $Helios^{I325V}$ mutant version does not affect DNA binding or homodimerization and heterodimerization to other Ikaros family members. However, we find that the p.I325V mutation in Helios does play a role in the destabilization of interactions with several binding partners. This is in line with the observation that this region, where the mutation lies, is predicted to contain a non-classical zinc-finger domain (*34*). Our interaction proteomics analysis expands the network of Helios interactors and identifies alterations in that network caused by the p.I325V mutation. For instance, we show that Helios interacts with cell cycle regulators, such as GTSE1 and PLK1 *(57)* and with transcription factors and histone modifiers, including known

interactors from the NuRD complex and unknown as the ATAC complex, with histone acetyltransferase activity (*58*). Similar to other IEIs caused by germline mutations in genes encoding for transcription factors with a key role in regulation of hematopoiesis such as GATA2 (*67*) or the Ikaros family transcription factor *IKZF1* itself (*68-69*), it is well possible that a phenotypic range of Helios-mutant patients with immunodeficiency may depend on the specific mutation and functional domain affected by individual Helios mutations. Future studies identifying other mutations in Helios should therefore aim to define the precise consequences of individual Helios mutations to enable genotype-phenotype correlations.

In regulatory T cells, Helios is responsible to maintain their immunosuppressive functions (*22*, *23*). Indeed, Helios, together with Foxp3, silences the *Il2* locus by promoting epigenetic modifications, in particular through histone deacetylation (*55*). Consistent with this, we observe an increase in IL-2 production in Helios^{I325V} Treg cells from our patient and a significant decrease in expression of genes involved in epigenetic and chromatin regulation, confirming the role of Helios as an *IL2* repressor in T_{regs} (*55*). Intriguingly, in conventional T cells, the picture is different: Helios^{I325V} conventional T cells from our patient exhibit a significant decrease in IL-2 production upon stimulation with reduced accessibility to the *Il2* locus. We speculate that this reduced accessibility is driven by Helios^{I325V}, which is line with the observation that Helios^{I325V} loses interactions with crucial epigenetic remodelers, such as HDAC1 and HDAC3, as well as TADA2A, KAT2A/KAT2B and SGF29, members of SAGA-like complexes, including the ATAC complex (*58*). To date, several lines of evidence support these observations: in the context of T-cell activation, Gao et al. have shown that a conditional knock-out of KAT2A (or GCN5) in T cells leads to impaired proliferation and reduced IL-2 production upon TCR stimulation, revealing its importance in the acetylation of the *Il2* promoter (*56*). Conversely, studies have shown that the *Il2*

promoter is silenced by Ikaros in resting $CD4^+$ T cells to maintain an anergic state, while Eos is required for IL-2 production in activated T cells (*59–61*).

Patient conventional T cells also show defective proliferation due to a delayed response to TCR stimulation, particularly in $CD4^+$ T cells. Proximal TCR signaling remained largely intact, suggesting that the changes in chromatin accessibility is not exclusive of the *Il2* locus, but involves a variety of genes, resulting in changes in gene expression. Supporting this idea, our ATAC-seq findings reveal decreased accessibility of genes involved in T-cell activation, while scRNA seq analysis show dysregulated transcriptome, mainly in the patient expanded pool of $CD8^+$ effector T-cells, indicative of their chronically activated and terminal effector state. Taken together, these findings imply a role of Helios in the regulation of chromatin accessibility to certain loci in activated conventional T cells through interactions with epigenetic remodelers, while pointing towards a higher level of regulation of the *Il2* promoter that is cell-type dependent (*55*). These mechanistic insights add to our understanding of how Ikaros family members exert their activating or repressive effects on gene transcription and strengthen their role in the regulation of IL-2 production.

In sum, we have identified a novel type of inborn error of immunity and characterized the deleterious effects of the biallelic mutation in Helios, p.I325V, leading to a dysregulated epigenome and transcriptome in T cells. Our work highlights the importance of conserving proteomic interactions to maintain Helios function. Beyond Tregs and enabled by a point-mutation leading to disrupted interactions, we have been able to further corroborate the less well-known role of Helios in conventional T cells, mediating the epigenetic changes required to ensure IL-2 production as well as timely activation and proliferation of T cells. Due to some functional redundancy between Ikaros family members and in addition to the identification of additional

Helios-mutant patients mentioned above, more studies targeting specific domains and residues in Helios in both cell lines and animal models (e.g., rather than performing conditional knock-outs), will be necessary to comprehensively delineate its role in epigenetic and transcriptional regulation, in the context of its interactions with various multimeric complexes (*26*).

Materials and methods

Study design

The objective of this study was to investigate the role of Helios on human immune homeostasis. For this purpose, we performed an array of functional and multi-omic experiments on primary material from the patient carrying a germline-encoded homozygous mutation in Helios, after genetic analysis. Furthermore, we made use of cellular models to investigate the effects of the mutation on Helios function using biochemical and proteomic approaches, all of which are described below.

Study approval

Samples from the patient, his family members and other healthy controls were obtained following an informed written consent and approval from the ethics committee of Tehran University of Medical Sciences as well as the Institutional Review Board of the Medical University of Vienna.

Immunophenotyping and Helios staining

Cryopreserved PBMCs from the patient and healthy controls were thawed and stained with fluorescent antibodies (table S9) for determining frequencies of T, B and NK-cell subpopulations. Helios and FOXP3 staining were performed using the eBioscience™ Foxp3/transcription factor staining buffer set (#00552300, ThermoFisher) according to manufacturer's protocol. Stained cells were acquired with an LSRFortessa™ or FACSCanto™ II (BD Biosciences). FlowJo™ v.10 was used to analyze the data and Prism v.8 (GraphPad) was used to produce graphs. Gating strategies are shown in fig. S1, S2, S3, S12 and S16. All adult healthy controls were aged 25-40 with representation of both males and females. Two age-matched controls were additionally included in immunophenotyping studies and scRNA-sequencing.

LightShift chemiluminescent EMSA

To assess the ability of Helios variants to bind to DNA, HEK293T cells (ATTC; CRL-1573) were transfected with pCMV6-C-Myc-Flag-Helios WT or mutant. All HEK293T transfections were done using the Effectene® Transfection Reagent (Qiagen) following the manufacturer's protocol. Gel mobility shift assays were performed with LightShift Chemiluminescent EMSA kit (Thermo Fisher Scientific) as previously described (*32*). Ikaros consensus-binding sequence 1 (IK-bs1) was used for EMSA assay (forward: 5′-BIOTIN- TCAGCTTTTGGGAATACCCTGTCA; reverse: 5′-BIOTIN- TGACAGGGTATTCCCAAAAGCTGA).

Immunofluorescence microscopy

To assess the ability of Helios variants to form foci around pericentromeric heterochromatin, NIH3T3 cells adherent on glass slides in 6-well plates were transfected with pCMV6-C-Myc-Flag-Helios WT or mutant using the X-tremeGENE™ 9 DNA Transfection Reagent (Sigma Aldrich), following manufacturer's protocol. After 20 hours of transfection, cells were fixed with 4% formaldehyde (#28908, Thermo Scientific) for 15 minutes, permeabilized (0.1% Triton X-100 in PBS) for 10 minutes and blocked (0.1% Triton X-100 and 10% FBS in PBS) for 30 minutes at room temperature. Cells were then incubated with Helios (D8W4X, CST 42427S) antibody for 2 hours, stained with Rabbit IgG-Alexa Fluor 488 secondary antibody (#A11034, Invitrogen) for 1 hour (both in blocking buffer in the dark) and then with DAPI (#63351, Roth). Coverslips were mounted in Fluorescent Mounting Medium (Dako). Axio Imager M2-1 (Zeiss) microscope was used to acquire the images with a 40x objective. The number of foci per cell for the WT and mutant

were quantified using Cell Profiler (https://cellprofiler.org). We used the Speckle Counting CellProfiler Pipeline provided on the website and modified it further to add a filtering step where only transfected cells were analyzed.

Co-immunoprecipitation (Co-IP)

The ability of Helios variants to homo/heterodimerize and bind to protein interaction partners was assessed by Co-IP studies. HEK293T cells were co-transfected with Strep-HA-Helios WT or mutant, together with the indicated plasmids. After 24 hours, cells were washed with PBS and lysed with IP lysis buffer (50 mM Tris (pH 7.5), 150 mM NaCl, 2 mM EDTA, 0.5% Triton X-100, 1 mM PMSF and protease inhibitor cocktail) for 30 minutes on ice. Lysates were centrifuged for 10 minutes at 13,000 rpm; some was taken for input. Rest of lysates were incubated with Strep-Tactin® Sepharose® 50% suspension (IBA) by rotating at 4 °C for 2 hours. Sepharose beads were then washed three times with lysis buffer and resuspended with 1.5X SDS loading buffer. Beads and input were analyzed by running on 8% SDS-PAGE and Western blotting with the following primary antibodies: Helios (D8W4X, Cell Signaling), HDAC1 (ab7028, Abcam), HA-HRP (HA-7, Sigma Aldrich), FLAG (F7425, Sigma Aldrich), Myc-tag (71D10, Cell Signaling) and GAPDH (G-9, Santa Cruz).

Interaction proteomics

BioID and LC-MS

The method followed has been outlined in detail by Liu et al. (*44*). In brief, Flip-In T-Rex HEK293 cell lines were co-transfected with C-terminally MAC-tagged Helios-WT or Helios-I325V or GFP

(with nuclear localization signal) together with the pOG44 vector for stable expression. Positive clones were selected and amplified. Tetracyclin and biotin induction was done on three biological replicates for 24 hours after which the samples were harvested. This was followed by affinity purification using a harsh lysis buffer. Lysates were cleared and loaded onto Bio-Rad spin columns with Strep-Tactin beads (IBA), followed by stringent washes and elution. The eluate was then reduced, alkylated, trypsin digested, desalted and dried as described, followed by reconstitution in 0.1% TFA and 1% Acetonitrile. Analysis of the sample was performed on a Q-Exactive mass spectrometer with an EASY-nLC 1000 system via an electrospray ionization sprayer (Thermo Fisher Scientific), using Xcalibur version 3.0.63. Database search was performed with Proteome Discoverer 1.4 (Thermo Scientific) using the SEQUEST search engine on the Reviewed human proteome in UniProtKB/SwissProt databases (http://www.uniprot.org, downloaded May 2020). All reported data were based on high-confidence peptides assigned in Proteome Discoverer (FDR < 0.05).

Identification of statistical confidence of interactions

Significance Analysis of INTeractome (SAINT)-express version 3.6.3 and Contaminant Repository for Affinity Purification (CRAPome, http://www.crapome.org, (*62*)) were used to discover statistically significant interactions from the LC-MS data. Final results represent proteins with a BFDR score lower than 0.05, and present in all three replicates. MaxQuant version 1.6.10.43 with the Andromeda search engine was used to compare differences in LFQ intensity between WT and I325V samples, two-tailed two-sample equal variance Student's t-test was performed and p-values lower than 0.05 were considered significant.

Overrepresentation Analysis and visualization

Overrepresentation analysis of statistically significant interactions in Gene Ontology was done with the R package enrichR (*46*) and overrepresentation of prey proteins in CORUM database (*45*) was done using Fisher's exact test and multiple testing correction in an in-house R-script. Interaction network was made with Cytoscape version 3.8.0.

Proliferation assay and T-cell exhaustion

Cryopreserved PBMCs from the patient and controls were assessed for the ability of T cells to proliferate. PBMCs were stained with Violet proliferation dye (VPD) 450 (BD Horizon) as per manufacturer's protocol and plated on 96-well plates. Cells were then stimulated with Dynabeads™ Human T-Activator CD3/CD28 (Gibco), 1 μg/mL anti-CD3 (OKT3, eBioscience), 1 μg/mL Phytohemagglutinin (PHA), or left unstimulated. On day 3 post-stimulation, cells were stained with CD3, CD4 and CD8-directed antibodies and proliferation was assessed by flow cytometry using the FACSCanto™ or LSRFortessa™ (BD). For measuring the expression of exhaustion markers upon stimulation with CD3/CD28 Dynabeads, surface staining of T cells was performed on ice using antibodies against PD-1, TIGIT, LAG3, AITR/GITR and TIM3 (table S9) at the basal state (day 0) and at different time-points when cells were harvested (day 2, 4 and 7). Cells were then washed and assessed by flow cytometry.

Intracellular cytokine production and IL-2 release

IL-2 cytokine production was analyzed by stimulating $0.2x10^6$ total PBMCs for 5 h with Phorbol 12-myristate 13-acetate (PMA, 0.2 mM) and Ionomycin (1 μg/mL) and adding Brefeldin A during the final 2.5 h of the stimulation. Cells were stained for T-cell surface markers (CD3, CD4, CD8,

CD45RA and CCR7) on ice for 30 mins. Subsequently, cells were fixed, permeabilized and stained with IL-2, IL-4, IL17A and/or IFNγ antibodies (table S7). FACSCanto™ II (BD) was used for flow cytometry analysis. T-lymphoblasts were also analyzed in the same way for IL-2 production after 16 h of PMA/ionomycin stimulation and addition of Brefeldin A during the final 4 h. Surface staining was done with CD3, CD4 and CD8. LSRFortessa™ (BD) was used for acquisition. Gating strategies are shown in supplementary figures and positive cytokine gates were set using the unstimulated controls. IL-2 release was assessed after harvesting cell-free supernatant following 24 h stimulation of $0.1x10^6$ PBMCs on 96-well U-bottom plates with CD3/CD28 Dynabeads™ using the Luminex 200 system (R&D Systems, following manufacturer's protocol).

Generation of CRISPR-Cas9 edited patient T-lymphoblasts with wildtype *IKZF2*

One million patient-derived PBMCs were stimulated on an α-CD3-coated well of a 24-well plate in T-cell media (RPMI media (Gibco) supplemented with 5% human serum, Hepes (20 mM), penicillin/streptomycin (10 µg/mL), sodium pyruvate (1mM) and non-essential amino acids (1X; all four from Gibco) with IL-2 (100 IU/mL). After 66 hours, cells were harvested and transfected using the NEPA21 electroporator with recombinant Cas9 nuclease (IDT), a sgRNA including the patient variant "G" underlined (AGTCACCTACCTTGGAGCTG) and the following single-stranded oligo donor (ssODN; synthesized by IDT as Ultramer™ DNA oligo) with the wildtype variant "A" shown underlined and the silent PAM change "A**G**G >A**A**G" in bold:

AGGCTGAGCTGATGCAGTCTCATATGATGGACCAAGCCATCAACAATGCAATCACCT

ACCTTGGAGCTG**AAG**CCCTTCACCCTCTGATGCAGCACCCGCC

After transfection, cells were left to expand in T-cell media with IL-2 for a week. This was followed by single-cell cloning of CRISPR-edited cells into a 384-well plate in T-cell media with

feeder cells (irradiated PBMCs from a blood donor), PHA (2 μg/mL) and IL-2 (200 IU/mL). After 10 days, clones were selected and re-expanded on a 96-well plate using feeder cells, PHA and IL-2, after which clones were genotyped by sanger sequencing using the same variant validation primers above.

Single-cell RNA sequencing

Frozen PBMCs from the patient and four controls were thawed, washed in RPMI media and resuspended in sterile PBS with 0.04% bovine serum albumin (BSA). A single-cell suspension was obtained by passing one million cells into a 5 mL FACS tube through a cell strainer and sorting for the live lymphocytes and monocytes based on the forward and side-scatter using the FACSAria™ Fusion (BD). Single-cell RNA-seq was then performed on the live samples using the 10x Genomics Chromium Controller with the Chromium Single Cell 3' Reagent Kit (v3 chemistry) following the manufacturer's instructions. After quality control, libraries were sequenced on the Illumina HiSeq 4000 platform in 2x75bp paired-end mode. Table S4 includes an overview of sequencing data and performance metrics. We used the CellRanger v3.0.2 software (10x Genomics) for demultiplexing and alignment to GRCh38 human reference transcriptome. The R statistics software was used to analyze the processed data. For optimal reproducibility, we used a Docker container containing R and all dependent libraries pre-installed (*cancerbits/dockR:mo-ikzf2-v1* available from https://hub.docker.com/r/cancerbits/dockr). Briefly, CellRanger outputs were loaded into R to perform quality control (removing cells with less than 1,000 genes, mitochondrial content more than 10%, or $\log_{10}$ doublet score >3 [calculated using the function *doubletCells* from scran (*63*) v1.14.6]) and downstream analysis using Seurat (*64*) v3.1.5. Each dataset was normalized (function *SCTransform* (*65*)) to generate corrected, log-transformed counts, and Pearson residuals by

regressing out mitochondrial content. We then used these normalized data to integrate all datasets using Harmony (*66*) v1.0. Integrated data was used for low-dimensional projection using UMAP (*47*) based on the top 30 principal components and for clustering cells (resolution = 0.2). Differential gene expression (DGE) analysis for this rare disease dataset suffers from lack of replication. In an attempt to reduce the impact of inter-individual differences (which would confound comparisons with variable number of cells from different individuals on both sides of a comparison), we used a stratified comparison scheme in which we performed comparisons per pair of individuals and focused on consistent differences across all pairwise comparisons. Specifically, statistics from sample-wise DGE tests were combined using the minimum log fold change ("worst fold change") and Fisher's method for p-values. Ribosomal proteins and cluster-sample strata with less than 50 cells were excluded from DGE analysis. We used MAST as a statistical test with FDR-adjusted p-value threshold of $q < 0.05$ and log fold change ≥ 0.25. Genes identified with the same direction of change in 75% of comparisons for between-cluster and 100% of comparisons for within-cluster comparisons were recorded as differentially expressed genes (table S6).

Supplementary Materials

Fig. S1. Gating strategy for B cell flow cytometry

Fig. S2. Gating strategy for T cell flow cytometry.

Fig. S3. Gating strategy for the identification of CD4+ folicullar helper, iNKT and MAIT cells by flow cytometry.

Fig. S4. Interaction with other Ikaros members and Sumoylation.

Fig. S5. CORUM analysis of interactors from Helios^{WT} and Helios^{I325V} BioID.

Table S7. SMART-seq metrics.

Table S8. Differential gene expression analysis data for SMART-seq.

Table S9. GO term enrichment analysis of SMART-seq output.

Table S10. ATAC-seq metrics and differential accessibility analysis.

Table S11. List of fluorescent antibodies used for flow cytometry.

Table S12. Raw data file

References

1. L. B. John, A. C. Ward, The Ikaros gene family: Transcriptional regulators of hematopoiesis and immunity. *Mol. Immunol.* **48**, 1272–1278 (2011).
2. B. Heizmann, P. Kastner, S. Chan, The Ikaros family in lymphocyte development. *Curr. Opin. Immunol.* **51**, 14–23 (2018).
3. Y. Fan, D. Lu, A. B. Pharmaceutica Sinica, The Ikaros family of zinc-finger proteins. *Acta Pharm. Sin. B*. **6**, 513–521 (2016).
4. K. Georgopoulos, The making of a lymphocyte: the choice among disparate cell fates and the IKAROS enigma. *Genes Dev.* **31**, 439–450 (2017).
5. R. Sridharan, S. T. Smale, Predominant interaction of both Ikaros and Helios with the NuRD complex in immature thymocytes. *J. Biol. Chem.* **282**, 30227–38 (2007).
6. K. P, T. M, D. A, K. P, C. S, Ikaros Is Critical for B Cell Differentiation and Function. *Eur. J. Immunol.* **32** (2002), doi:10.1002/1521-4141(200203)32:3<720::AID-IMMU720>3.0.CO;2-P.
7. D. Reynaud, I. A. Demarco, K. L. Reddy, H. Schjerven, E. Bertolino, Z. Chen, S. T. Smale, S. Winandy, H. Singh, Regulation of B cell fate commitment and immunoglobulin heavy-chain gene rearrangements by Ikaros. *Nat. Immunol.* **9**, 927–936 (2008).
8. J. H. Wang, N. Avitahl, A. Cariappa, C. Friedrich, T. Ikeda, A. Renold, K. Andrikopoulos, L. Liang, S. Pillai, B. A. Morgan, K. Georgopoulos, Aiolos regulates B cell activation and maturation to effector state. *Immunity*. **9**, 543–553 (1998).
9. S. Ma, S. Pathak, M. Mandal, L. Trinh, M. R. Clark, R. Lu, Ikaros and Aiolos Inhibit Pre-B-Cell Proliferation by Directly Suppressing c-Myc Expression. *Mol. Cell. Biol.* **30**, 4149–4158 (2010).
10. S. Winandy, L. Wu, J. H. Wang, K. Georgopoulos, Pre-T cell receptor (TCR) and TCR-controlled checkpoints in T cell differentiation are set by Ikaros. *J. Exp. Med.* **190**, 1039–1048 (1999).
11. E. Kleinmann, A.-S. Geimer Le Lay, M. Sellars, P. Kastner, S. Chan, Ikaros Represses the Transcriptional Response to Notch Signaling in T-Cell Development. *Mol. Cell. Biol.* **28**, 7465–7475 (2008).
12. J. H. Wang, A. Nichogiannopoulou, L. Wu, L. Sun, A. H. Sharpe, M. Bigby, K. Georgopoulos, Selective defects in the development of the fetal and adult lymphoid system in mice with an Ikaros null mutation. *Immunity*. **5**, 537–549 (1996).
13. C. M. Kelley, T. Ikeda, J. Koipally, N. Avitahl, L. Wu, K. Georgopoulos, B. A. Morgan, Helios, a novel dimerization partner of Ikaros expressed in the earliest hematopoietic progenitors. *Curr. Biol.* **8**, 508–15 (1998).
14. K. Hahm, B. S. Cobb, A. S. McCarty, K. E. Brown, C. A. Klug, R. Lee, K. Akashi, I. L. Weissman, A. G. Fisher, S. T. Smale, Helios, a T cell-restricted Ikaros family member that quantitatively associates with Ikaros at centromeric heterochromatin. *Genes Dev.* **12**, 782–96 (1998).
15. K. Serre, C. Bénézech, G. Desanti, S. Bobat, K.-M. Toellner, R. Bird, S. Chan, P. Kastner, A. F. Cunningham, I. C. M. Maclennan, E. Mohr, Helios is associated with CD4 T cells differentiating to T helper 2 and follicular helper T cells in vivo independently of Foxp3 expression. *PLoS One*. **6**, e20731 (2011).
16. D. Getnet, J. F. Grosso, M. V. Goldberg, T. J. Harris, H.-R. Yen, T. C. Bruno, N. M. Durham, E. L. Hipkiss, K. J. Pyle, S. Wada, A role for the transcription factor Helios in

human CD4+CD25+ regulatory T cells. *Mol. Immunol.* **47**, 1595–1600 (2010).
17. E. Leeansyah, J. Svärd, J. Dias, M. Buggert, J. Nyström, M. F. Quigley, M. Moll, A. Sönnerborg, P. Nowak, J. K. Sandberg, Arming of MAIT Cell Cytolytic Antimicrobial Activity Is Induced by IL-7 and Defective in HIV-1 Infection. *PLOS Pathog.* **11**, e1005072 (2015).
18. J. Dias, C. Boulouis, J.-B. Gorin, R. H. G. A. van den Biggelaar, K. G. Lal, A. Gibbs, L. Loh, M. Y. Gulam, W. R. Sia, S. Bari, W. Y. K. Hwang, D. F. Nixon, S. Nguyen, M. R. Betts, M. Buggert, M. A. Eller, K. Broliden, A. Tjernlund, J. K. Sandberg, E. Leeansyah, The CD4 $^{-}$ CD8 $^{-}$ MAIT cell subpopulation is a functionally distinct subset developmentally related to the main CD8 $^{+}$ MAIT cell pool. *Proc. Natl. Acad. Sci.* **115**, E11513–E11522 (2018).
19. T. Akimova, U. H. Beier, L. Wang, M. H. Levine, W. W. Hancock, Helios expression is a marker of T cell activation and proliferation. *PLoS One*. **6**, e24226 (2011).
20. A. M. Thornton, P. E. Korty, D. Q. Tran, E. A. Wohlfert, P. E. Murray, Y. Belkaid, E. M. Shevach, Expression of Helios, an Ikaros Transcription Factor Family Member, Differentiates Thymic-Derived from Peripherally Induced Foxp3 + T Regulatory Cells . *J. Immunol.* **184**, 3433–3441 (2010).
21. A. M. Thornton, J. Lu, P. E. Korty, Y. C. Kim, C. Martens, P. D. Sun, E. M. Shevach, Helios + and Helios − Treg subpopulations are phenotypically and functionally distinct and express dissimilar TCR repertoires. *Eur. J. Immunol.* **49**, 398–412 (2019).
22. H.-J. Kim, R. A. Barnitz, T. Kreslavsky, F. D. Brown, H. Moffett, M. E. Lemieux, Y. Kaygusuz, T. Meissner, T. A. W. Holderried, S. Chan, P. Kastner, W. N. Haining, H. Cantor, Stable inhibitory activity of regulatory T cells requires the transcription factor Helios. *Science (80-.).* **350**, 334–339 (2015).
23. M. Sebastian, M. Lopez-Ocasio, A. Metidji, S. A. Rieder, E. M. Shevach, A. M. Thornton, Helios Controls a Limited Subset of Regulatory T Cell Functions. *J. Immunol.* **196**, 144–155 (2016).
24. E. M. Ross, D. Bourges, T. V. Hogan, P. A. Gleeson, I. R. van Driel, Helios defines T cells being driven to tolerance in the periphery and thymus. *Eur. J. Immunol.* **44**, 2048–2058 (2014).
25. Q. Cai, A. Dierich, M. Oulad-Abdelghani, S. Chan, P. Kastner, Helios Deficiency Has Minimal Impact on T Cell Development and Function. *J. Immunol.* **183**, 2303–2311 (2009).
26. A. M. Thornton, E. M. Shevach, Helios: still behind the clouds. *Immunology*. **158**, 161–170 (2019).
27. H. S. Kuehn, B. Boisson, C. Cunningham-Rundles, J. Reichenbach, A. Stray-Pedersen, E. W. Gelfand, P. Maffucci, K. R. Pierce, J. K. Abbott, K. V Voelkerding, S. T. South, N. H. Augustine, J. S. Bush, W. K. Dolen, B. B. Wray, Y. Itan, A. Cobat, H. S. Sorte, S. Ganesan, S. Prader, T. B. Martins, M. G. Lawrence, J. S. Orange, K. R. Calvo, J. E. Niemela, J.-L. Casanova, T. A. Fleisher, H. R. Hill, A. Kumánovics, M. E. Conley, S. D. Rosenzweig, Loss of B Cells in Patients with Heterozygous Mutations in IKAROS. *N. Engl. J. Med.* **374**, 1032–1043 (2016).
28. D. J. Bogaert, H. S. Kuehn, C. Bonroy, K. R. Calvo, J. Dehoorne, A. V. Vanlander, M. De Bruyne, U. Cytlak, V. Bigley, F. De Baets, E. De Baere, S. D. Rosenzweig, F. Haerynck, M. Dullaers, A novel IKAROS haploinsufficiency kindred with unexpectedly late and variable B-cell maturation defects. *J. Allergy Clin. Immunol.* **141**, 432-435.e7 (2018).

29. Z. Eskandarian, M. Fliegauf, A. Bulashevska, M. Proietti, R. Hague, C. R. Smulski, D. Schubert, K. Warnatz, B. Grimbacher, Assessing the Functional Relevance of Variants in the IKAROS Family Zinc Finger Protein 1 (IKZF1) in a Cohort of Patients With Primary Immunodeficiency. *Front. Immunol.* **10**, 568 (2019).
30. C. J. Nunes-Santos, H. S. Kuehn, S. D. Rosenzweig, IKAROS Family Zinc Finger 1–Associated Diseases in Primary Immunodeficiency Patients. *Immunol. Allergy Clin. North Am.* **40** (2020), pp. 461–470.
31. H. S. Kuehn, J. E. Niemela, J. Stoddard, S. Ciullini Mannurita, T. Shahin, S. Goel, M. Hintermeyer, R. Jimenez Heredi, M. Garofalo, L. Lucas, S. Singh, A. Tondo, Z. D. Jacobs, W. Gahl, S. Latour, J. Verbsky, J. Routes, C. Cunningham-Rundles, K. Boztug, E. Gambineri, T. A. Fleisher, S. Chandrakasan, S. Rosenzweig, Germline IKAROS dimerization haploinsufficiency causes hematologic cytopenias and malignancies. *Blood* (2020), doi:10.1182/blood.2020007292.
32. D. Boutboul, H. S. Kuehn, Z. Van de Wyngaert, J. E. Niemela, I. Callebaut, J. Stoddard, C. Lenoir, V. Barlogis, C. Farnarier, F. Vely, N. Yoshida, S. Kojima, H. Kanegane, A. Hoshino, F. Hauck, L. Lhermitte, V. Asnafi, P. Roehrs, S. Chen, J. W. Verbsky, K. R. Calvo, A. Husami, K. Zhang, J. Roberts, D. Amrol, J. Sleaseman, A. P. Hsu, S. M. Holland, R. Marsh, A. Fischer, T. A. Fleisher, C. Picard, S. Latour, S. D. Rosenzweig, Dominant-negative IKZF1 mutations cause a T, B, and myeloid cell combined immunodeficiency. *J. Clin. Invest.* **128**, 3071–3087 (2018).
33. M. Yamashita, H. S. Kuehn, K. Okuyama, S. Okada, Y. Inoue, N. Mitsuiki, K. Imai, M. Takagi, H. Kanegane, M. Takeuchi, N. Shimojo, M. Tsumura, A. K. Padhi, K. Y. J. Zhang, B. Boisson, J.-L. Casanova, O. Ohara, S. D. Rosenzweig, I. Taniuchi, T. Morio, A variant in human AIOLOS impairs adaptive immunity by interfering with IKAROS. *Nat. Immunol. 2021 227*. **22**, 893–903 (2021).
34. T. E. Lewis, I. Sillitoe, A. Andreeva, T. L. Blundell, D. W. A. Buchan, C. Chothia, D. Cozzetto, J. M. Dana, I. Filippis, J. Gough, D. T. Jones, L. A. Kelley, G. J. Kleywegt, F. Minneci, J. Mistry, A. G. Murzin, B. Ochoa-Montaño, M. E. Oates, M. Punta, O. J. L. Rackham, J. Stahlhacke, M. J. E. Sternberg, S. Velankar, C. Orengo, Genome3D: Exploiting structure to help users understand their sequences. *Nucleic Acids Res.* **43**, D382–D386 (2015).
35. J. M. Matthews, M. Sunde, Zinc fingers - Folds for many occasions. *IUBMB Life*. **54** (2002), pp. 351–355.
36. K. J. Karczewski, L. C. Francioli, G. Tiao, B. B. Cummings, J. Alföldi, Q. Wang, R. L. Collins, K. M. Laricchia, A. Ganna, D. P. Birnbaum, L. D. Gauthier, H. Brand, M. Solomonson, N. A. Watts, D. Rhodes, M. Singer-Berk, E. M. England, E. G. Seaby, J. A. Kosmicki, R. K. Walters, K. Tashman, Y. Farjoun, E. Banks, T. Poterba, A. Wang, C. Seed, N. Whiffin, J. X. Chong, K. E. Samocha, E. Pierce-Hoffman, Z. Zappala, A. H. O'Donnell-Luria, E. V. Minikel, B. Weisburd, M. Lek, J. S. Ware, C. Vittal, I. M. Armean, L. Bergelson, K. Cibulskis, K. M. Connolly, M. Covarrubias, S. Donnelly, S. Ferriera, S. Gabriel, J. Gentry, N. Gupta, T. Jeandet, D. Kaplan, C. Llanwarne, R. Munshi, S. Novod, N. Petrillo, D. Roazen, V. Ruano-Rubio, A. Saltzman, M. Schleicher, J. Soto, K. Tibbetts, C. Tolonen, G. Wade, M. E. Talkowski, T. G. A. D. Consortium, B. M. Neale, M. J. Daly, D. G. MacArthur, Variation across 141,456 human exomes and genomes reveals the spectrum of loss-of-function intolerance across human protein-coding genes. *bioRxiv*, 531210 (2019).

37. M. Lek, K. J. Karczewski, E. V. Minikel, K. E. Samocha, E. Banks, T. Fennell, A. H. O'Donnell-Luria, J. S. Ware, A. J. Hill, B. B. Cummings, T. Tukiainen, D. P. Birnbaum, J. A. Kosmicki, L. E. Duncan, K. Estrada, F. Zhao, J. Zou, E. Pierce-Hoffman, J. Berghout, D. N. Cooper, N. Deflaux, M. DePristo, R. Do, J. Flannick, M. Fromer, L. Gauthier, J. Goldstein, N. Gupta, D. Howrigan, A. Kiezun, M. I. Kurki, A. L. Moonshine, P. Natarajan, L. Orozco, G. M. Peloso, R. Poplin, M. A. Rivas, V. Ruano-Rubio, S. A. Rose, D. M. Ruderfer, K. Shakir, P. D. Stenson, C. Stevens, B. P. Thomas, G. Tiao, M. T. Tusie-Luna, B. Weisburd, H. H. Won, D. Yu, D. M. Altshuler, D. Ardissino, M. Boehnke, J. Danesh, S. Donnelly, R. Elosua, J. C. Florez, S. B. Gabriel, G. Getz, S. J. Glatt, C. M. Hultman, S. Kathiresan, M. Laakso, S. McCarroll, M. I. McCarthy, D. McGovern, R. McPherson, B. M. Neale, A. Palotie, S. M. Purcell, D. Saleheen, J. M. Scharf, P. Sklar, P. F. Sullivan, J. Tuomilehto, M. T. Tsuang, H. C. Watkins, J. G. Wilson, M. J. Daly, D. G. MacArthur, H. E. Abboud, G. Abecasis, C. A. Aguilar-Salinas, O. Arellano-Campos, G. Atzmon, I. Aukrust, C. L. Barr, G. I. Bell, S. Bergen, L. Bjørkhaug, J. Blangero, D. W. Bowden, C. L. Budman, N. P. Burtt, F. Centeno-Cruz, J. C. Chambers, K. Chambert, R. Clarke, R. Collins, G. Coppola, E. J. Córdova, M. L. Cortes, N. J. Cox, R. Duggirala, M. Farrall, J. C. Fernandez-Lopez, P. Fontanillas, T. M. Frayling, N. B. Freimer, C. Fuchsberger, H. García-Ortiz, A. Goel, M. J. Gómez-Vázquez, M. E. González-Villalpando, C. González-Villalpando, M. A. Grados, L. Groop, C. A. Haiman, C. L. Hanis, A. T. Hattersley, B. E. Henderson, J. C. Hopewell, A. Huerta-Chagoya, S. Islas-Andrade, S. B. Jacobs, S. Jalilzadeh, C. P. Jenkinson, J. Moran, S. Jiménez-Morale, A. Kähler, R. A. King, G. Kirov, J. S. Kooner, T. Kyriakou, J. Y. Lee, D. M. Lehman, G. Lyon, W. MacMahon, P. K. Magnusson, A. Mahajan, J. Marrugat, A. Martínez-Hernández, C. A. Mathews, G. McVean, J. B. Meigs, T. Meitinger, E. Mendoza-Caamal, J. M. Mercader, K. L. Mohlke, H. Moreno-Macías, A. P. Morris, L. A. Najmi, P. R. Njølstad, M. C. O'Donovan, M. L. Ordóñez-Sánchez, M. J. Owen, T. Park, D. L. Pauls, D. Posthuma, C. Revilla-Monsalve, L. Riba, S. Ripke, R. Rodríguez-Guillén, M. Rodríguez-Torres, P. Sandor, M. Seielstad, R. Sladek, X. Soberón, T. D. Spector, S. E. Tai, T. M. Teslovich, G. Walford, L. R. Wilkens, A. L. Williams, Analysis of protein-coding genetic variation in 60,706 humans. *Nature*. **536**, 285–291 (2016).
38. K. Thorarinsdottir, A. Camponeschi, I. Gjertsson, I. L. Mårtensson, CD21-/low B cells: A Snapshot of a Unique B Cell Subset in Health and Disease. *Scand. J. Immunol.* **82** (2015), pp. 254–261.
39. M. Strioga, V. Pasukoniene, D. Characiejus, CD8+CD28- and CD8+CD57+ T cells and their role in health and disease. *Immunology*. **134** (2011), pp. 17–32.
40. L. Sun, H. Kerawalla, X. Wu, M. S. Lehnert, F. M. Uckun, Expression of a Unique Helios Isoform in Human Leukemia Cells. *Leuk. Lymphoma*. **43**, 841–849 (2002).
41. P. Gómez-del Arco, J. Koipally, K. Georgopoulos, Ikaros SUMOylation: switching out of repression. *Mol. Cell. Biol.* **25**, 2688–97 (2005).
42. K. Georgopoulos, Haematopoietic cell-fate decisions, chromatin regulation and ikaros. *Nat. Rev. Immunol.* **2**, 162–174 (2002).
43. K. J. Roux, D. I. Kim, M. Raida, B. Burke, A promiscuous biotin ligase fusion protein identifies proximal and interacting proteins in mammalian cells. *J. Cell Biol.* **196**, 801–810 (2012).
44. X. Liu, K. Salokas, F. Tamene, Y. Jiu, R. G. Weldatsadik, T. Öhman, M. Varjosalo, An AP-MS- and BioID-compatible MAC-tag enables comprehensive mapping of protein

interactions and subcellular localizations. *Nat. Commun.* **9** (2018), doi:10.1038/s41467-018-03523-2.
45. M. Giurgiu, J. Reinhard, B. Brauner, I. Dunger-Kaltenbach, G. Fobo, G. Frishman, C. Montrone, A. Ruepp, CORUM: the comprehensive resource of mammalian protein complexes-2019. *Nucleic Acids Res.* **47**, 559–563 (2018).
46. M. V. Kuleshov, M. R. Jones, A. D. Rouillard, N. F. Fernandez, Q. Duan, Z. Wang, S. Koplev, S. L. Jenkins, K. M. Jagodnik, A. Lachmann, M. G. McDermott, C. D. Monteiro, G. W. Gundersen, A. Ma'ayan, Enrichr: a comprehensive gene set enrichment analysis web server 2016 update. *Nucleic Acids Res.* **44**, W90–W97 (2016).
47. L. McInnes, J. Healy, J. Melville, UMAP: Uniform Manifold Approximation and Projection for Dimension Reduction (2018) (available at http://arxiv.org/abs/1802.03426).
48. G. Finak, A. McDavid, M. Yajima, J. Deng, V. Gersuk, A. K. Shalek, C. K. Slichter, H. W. Miller, M. J. McElrath, M. Prlic, P. S. Linsley, R. Gottardo, MAST: A flexible statistical framework for assessing transcriptional changes and characterizing heterogeneity in single-cell RNA sequencing data. *Genome Biol.* **16**, 278 (2015).
49. O. M. Seternes, A. M. Kidger, S. M. Keyse, Dual-specificity MAP kinase phosphatases in health and disease. *Biochim. Biophys. Acta - Mol. Cell Res.* **1866**, 124–143 (2019).
50. M. H. Brush, D. C. Weiser, S. Shenolikar, Growth Arrest and DNA Damage-Inducible Protein GADD34 Targets Protein Phosphatase 1α to the Endoplasmic Reticulum and Promotes Dephosphorylation of the α Subunit of Eukaryotic Translation Initiation Factor 2. *Mol. Cell. Biol.* **23**, 1292–1303 (2003).
51. B. Di Marco, M. Massetti, S. Bruscoli, A. Macchiarulo, R. Di Virgilio, E. Velardi, V. Donato, G. Migliorati, C. Riccardi, Glucocorticoid-induced leucine zipper (GILZ)/NF-kB interaction: role of GILZ homo-dimerization and C-terminal domain. *Nucleic Acids Res.* **35**, 517–528 (2007).
52. M. L. Asselin-Labat, M. David, A. Biola-Vidamment, D. Lecoeuche, M. C. Zennaro, J. Bertoglio, M. Pallardy, GILZ, a new target for the transcription factor FoxO3, protects T lymphocytes from interleukin-2 withdrawal-induced apoptosis. *Blood*. **104**, 215–223 (2004).
53. S. Picelli, O. R. Faridani, Å. K. Björklund, G. Winberg, S. Sagasser, R. Sandberg, Full-length RNA-seq from single cells using Smart-seq2. *Nat. Protoc.* **9**, 171–181 (2014).
54. F. Birzele, T. Fauti, H. Stahl, M. C. Lenter, E. Simon, D. Knebel, A. Weith, T. Hildebrandt, D. Mennerich, Next-generation insights into regulatory T cells: Expression profiling and FoxP3 occupancy in Human. *Nucleic Acids Res.* **39**, 7946–7960 (2011).
55. I. Baine, S. Basu, R. Ames, R. S. Sellers, F. Macian, Helios induces epigenetic silencing of Il2 gene expression in regulatory T cells, doi:10.4049/jimmunol.1200792.
56. B. Gao, Q. Kong, Y. Zhang, C. Yun, S. Y. R. Dent, J. Song, D. D. Zhang, Y. Wang, X. Li, D. Fang, The Histone Acetyltransferase Gcn5 Positively Regulates T Cell Activation. *J. Immunol.* **198**, 3927–3938 (2017).
57. S. Zitouni, C. Nabais, S. C. Jana, A. Guerrero, M. Bettencourt-Dias, Polo-like kinases: Structural variations lead to multiple functions. *Nat. Rev. Mol. Cell Biol.* **15** (2014), pp. 433–452.
58. G. Spedale, H. T. M. Timmers, W. W. M. P. Pijnappel, ATAC-king the complexity of SAGA during evolution. *Genes Dev.* **26**, 527–541 (2012).
59. R. M. Thomas, N. Chunder, C. Chen, S. E. Umetsu, S. Winandy, A. D. Wells, Ikaros Enforces the Costimulatory Requirement for IL2 Gene Expression and Is Required for

Anergy Induction in CD4 + T Lymphocytes . *J. Immunol.* **179**, 7305–7315 (2007).
60. S. Bandyopadhyay, M. Duré, M. Paroder, N. Soto-Nieves, I. Puga, F. Macián, Interleukin 2 gene transcription is regulated by Ikaros-induced changes in histone acetylation in anergic T cells. *Blood*. **109**, 2878–2886 (2007).
61. S. A. Rieder, A. Metidji, D. D. Glass, A. M. Thornton, T. Ikeda, B. A. Morgan, E. M. Shevach, Eos Is Redundant for Regulatory T Cell Function but Plays an Important Role in IL-2 and Th17 Production by CD4 + Conventional T Cells . *J. Immunol.* **195**, 553–563 (2015).
62. D. Mellacheruvu, Z. Wright, A. L. Couzens, J. P. Lambert, N. A. St-Denis, T. Li, Y. V. Miteva, S. Hauri, M. E. Sardiu, T. Y. Low, V. A. Halim, R. D. Bagshaw, N. C. Hubner, A. Al-Hakim, A. Bouchard, D. Faubert, D. Fermin, W. H. Dunham, M. Goudreault, Z. Y. Lin, B. G. Badillo, T. Pawson, D. Durocher, B. Coulombe, R. Aebersold, G. Superti-Furga, J. Colinge, A. J. R. Heck, H. Choi, M. Gstaiger, S. Mohammed, I. M. Cristea, K. L. Bennett, M. P. Washburn, B. Raught, R. M. Ewing, A. C. Gingras, A. I. Nesvizhskii, The CRAPome: A contaminant repository for affinity purification-mass spectrometry data. *Nat. Methods*. **10**, 730–736 (2013).
63. A. T. L. Lun, D. J. McCarthy, J. C. Marioni, A step-by-step workflow for low-level analysis of single-cell RNA-seq data with Bioconductor. *F1000Research*. **5**, 2122 (2016).
64. A. Butler, P. Hoffman, P. Smibert, E. Papalexi, R. Satija, Integrating single-cell transcriptomic data across different conditions, technologies, and species. *Nat. Biotechnol.* **36**, 411–420 (2018).
65. C. Hafemeister, R. Satija, Normalization and variance stabilization of single-cell RNA-seq data using regularized negative binomial regression. *Genome Biol.* **20** (2019), doi:10.1186/s13059-019-1874-1.
66. I. Korsunsky, N. Millard, J. Fan, K. Slowikowski, F. Zhang, K. Wei, Y. Baglaenko, M. Brenner, P. ru Loh, S. Raychaudhuri, Fast, sensitive and accurate integration of single-cell data with Harmony. *Nat. Methods*. **16**, 1289–1296 (2019).
67. C.E. Chong, P. Venugopal, P.H. Stokes, Y.K. Lee, P.J. Brautigan, D.T.O. Yeung, M. Babic, G.A. Engler, S.W. Lane, M. Klingler-Hoffmann, J.M. Matthews, R.J. D'Andrea, A.L. Brown, C.N. Hahn, H.S. Scott. Differential effects on gene transcription and hematopoietic differentiation correlate with GATA2 mutant disease phenotypes. Leukemia. **32(1)**, 194-202 (2018)
68. A. Hoshino, S. Okada, K. Yoshida, N. Nishida, Y. Okuno, H. Ueno, M. Yamashita, T. Okano, M. Tsumura, S. Nishimura, et al. Abnormal hematopoiesis and autoimmunity in human subjects with germline IKZF1 mutations. J Allergy Clin Immunol. **140**, 223–231 (2016)
69. H.S. Kuehn, B. Boisson, C . Cunningham-Rundles, J. Reichenbach, A. Stray-Pedersen, E.W. Gelfand, P. Maffucci, K.R. Pierce, J.K. Abbott, K.V. Voelkerding, et al. Loss of B Cells in Patients with Heterozygous Mutations in IKAROS. N Engl J Med. **374**, 1032–1043 (2016)
70. E. Salzer, D. Cagdas, M. Hons, E. M. Mace, W. Garncarz, Ö. Y. Petronczki, R. Platzer, L. Pfajfer, I. Bilic, S. A. Ban, K. L. Willmann, M. Mukherjee, V. Supper, H. T. Hsu, P. P. Banerjee, P. Sinha, F. McClanahan, G. J. Zlabinger, W. F. Pickl, J. G. Gribben, H. Stockinger, K. L. Bennett, J. B. Huppa, L. Dupré, Ö. Sanal, U. Jäger, M. Sixt, I. Tezcan, J. S. Orange, K. Boztug, RASGRP1 deficiency causes immunodeficiency with impaired cytoskeletal dynamics. *Nat. Immunol.* **17**, 1352–1360 (2016).

71. H. Müller, R. Jimenez-Heredia, A. Krolo, T. Hirschmugl, J. Dmytrus, K. Boztug, C. Bock, VCF.Filter: interactive prioritization of disease-linked genetic variants from sequencing data. *Nucleic Acids Res.* **45**, W567–W572 (2017).
72. M. Kircher, D. M. Witten, P. Jain, B. J. O'Roak, G. M. Cooper, J. Shendure, A general framework for estimating the relative pathogenicity of human genetic variants. *Nat. Genet.* **46**, 310–5 (2014).
73. A. M. Bolger, M. Lohse, B. Usadel, Trimmomatic: A flexible trimmer for Illumina sequence data. *Bioinformatics*. **30**, 2114–2120 (2014).
74. A. Dobin, C. A. Davis, F. Schlesinger, J. Drenkow, C. Zaleski, S. Jha, P. Batut, M. Chaisson, T. R. Gingeras, STAR: Ultrafast universal RNA-seq aligner. *Bioinformatics*. **29**, 15–21 (2013).
75. Y. Liao, G. K. Smyth, W. Shi, FeatureCounts: An efficient general purpose program for assigning sequence reads to genomic features. *Bioinformatics*. **30**, 923–930 (2014).
76. A. B. Keenan, D. Torre, A. Lachmann, A. K. Leong, M. L. Wojciechowicz, V. Utti, K. M. Jagodnik, E. Kropiwnicki, Z. Wang, A. Ma'ayan, ChEA3: transcription factor enrichment analysis by orthogonal omics integration. *Nucleic Acids Res.* **47**, W212–W224 (2019).
77. J. P. Smith, M. R. Corces, J. Xu, V. P. Reuter, H. Y. Chang, N. C. Sheffield, PEPATAC: An optimized ATAC-seq pipeline with serial alignments. *bioRxiv* (2020), doi:10.1101/2020.10.21.347054.
78. R. C. Team, R: A Language and Environment for Statistical Computing (2021), (available at https://www.r-project.org/).
79. H. Wickham, M. Averick, J. Bryan, W. Chang, L. D. McGowan, R. François, G. Grolemund, A. Hayes, L. Henry, J. Hester, M. Kuhn, T. L. Pedersen, E. Miller, S. M. Bache, K. Müller, J. Ooms, D. Robinson, D. P. Seidel, V. Spinu, K. Takahashi, D. Vaughan, C. Wilke, K. Woo, H. Yutani, Welcome to the {tidyverse}. *J. Open Source Softw.* **4**, 1686 (2019).
80. M. Lawrence, W. Huber, H. Pagès, P. Aboyoun, M. Carlson, R. Gentleman, M. Morgan, V. Carey, Software for Computing and Annotating Genomic Ranges. *{PLoS} Comput. Biol.* **9** (2013), doi:10.1371/journal.pcbi.1003118.
81. T. S. Carroll, Z. Liang, R. Salama, R. Stark, I. de Santiago, Impact of artifact removal on ChIP quality metrics in ChIP-seq and ChIP-exo data. *Front. Genet.* **5**, 75 (2014).
82. H. M. Amemiya, A. Kundaje, A. P. Boyle, The ENCODE Blacklist: Identification of Problematic Regions of the Genome. *Sci. Rep.* **9**, 9354 (2019).
83. B. C. Team, B. P. Maintainer, TxDb.Hsapiens.UCSC.hg38.knownGene Annotation package for TxDb object(s) (2021).
84. M. I. Love, W. Huber, S. Anders, Moderated estimation of fold change and dispersion for RNA-seq data with DESeq2. *Genome Biol.* **15**, 1–21 (2014).
85. G. Yu, L.-G. Wang, Y. Han, Q.-Y. He, clusterProfiler: an R package for comparing biological themes among gene clusters. *Omi. A J. Integr. Biol.* **16**, 284–287 (2012).
86. O. Fornes, J. A. Castro-Mondragon, A. Khan, R. van der Lee, X. Zhang, P. A. Richmond, B. P. Modi, S. Correard, M. Gheorghe, D. Baranašić, W. Santana-Garcia, G. Tan, J. Chèneby, B. Ballester, F. Parcy, A. Sandelin, B. Lenhard, W. W. Wasserman, A. Mathelier, JASPAR 2020: update of the open-access database of transcription factor binding profiles. *Nucleic Acids Res.* **48**, D87–D92 (2019).
87. G. Tan, B. Lenhard, TFBSTools: an R/Bioconductor package for transcription factor binding site analysis. *Bioinformatics*. **32**, 1555–1556 (2016).

88. A. Schep, motifmatchr: Fast Motif Matching in R (2021).
89. A. N. Schep, B. Wu, J. D. Buenrostro, W. J. Greenleaf, chromVAR: inferring transcription-factor-associated accessibility from single-cell epigenomic data. *Nat. Methods* (2017), doi:10.1038/nmeth.4401.
90. B. Gel, E. Serra, karyoploteR: an R/Bioconductor package to plot customizable genomes displaying arbitrary data. *Bioinformatics*. **33**, 3088–3090 (2017).
91. K. Khan, M. Zech, A. T. Morgan, D. J. Amor, M. Skorvanek, T. N. Khan, M. S. Hildebrand, V. E. Jackson, T. S. Scerri, M. Coleman, K. A. Rigbye, I. E. Scheffer, M. Bahlo, M. Wagner, D. D. Lam, R. Berutti, P. Havránková, A. Fečíková, T. M. Strom, V. Han, P. Dosekova, Z. Gdovinova, F. Laccone, M. Jameel, M. R. Mooney, S. M. Baig, R. Jech, E. E. Davis, N. Katsanis, J. Winkelmann, Recessive variants in ZNF142 cause a complex neurodevelopmental disorder with intellectual disability, speech impairment, seizures, and dystonia. *Genet. Med.* **21**, 2532–2542 (2019).

Acknowledgments: We thank the patient and his family members for their participation in our study. We also thank the Biomedical Sequencing Facility (BSF at the CeMM Research Center of Molecular Medicine (CeMM) of the Austrian Academy of Sciences) for their single-cell RNA-seq service. **Funding**: This study has been supported by the European Research Council Consolidator Grant iDysChart (ERC grant agreement number: 820074) (to K.B.), a doctoral fellowship program (Cell Communication in Health and Disease (CCHD) from the Medical University of Vienna) (to K.B. and T.S.), the Austrian Science Fund FWF project T934-B30 (to B.H.), the Intramural Research Program, NIH Clinical Center, US National Institutes of Health (NIH) (to S.R.), and the Academy of Finland (nos. 288475 and 294173), the Sigrid Juselius Foundation, the Finnish Cancer Institute, and Biocenter Finland (to M.V.). **Author contributions**: T.S. performed most of the experiments on patient material, analyzed and interpreted the data. T.S., H.K., B.H. and S.G. performed the biochemical experiments. T.S. supervised S.G. M.S., under the supervision of F.H. analyzed the scRNA-seq data. PR with input from F.H. analyzed ATAC-seq and SMART-seq data. T.S. interpreted the scRNA-seq results, with input from S.Z. L.G. performed the BioID experiments and processed the mass spectrometry data. M.V. provided the laboratory resources for the BioID experiments and supervised L.G. O.Y.P. did the immunofluorescence stainings and analyzed the data on Cell Profiler. N.R. and S.Z. recruited the patient in Iran and assisted in the collection of medical data. S.K.B. assisted in medical data interpretations. J.D. identified the variant; S.Z. performed the segregation analysis. D.S. assisted with scientific interpretation. T.S., I.C. and K.B. wrote the manuscript with input from all co-authors. S.R. and H.K. provided the laboratory resources for some experiments and gave critical and valuable input into the study. K.B. coordinated the study, provided the laboratory resources, assisted in data interpretation and took overall responsibility of the study. **Competing interests**: The authors declare no competing

financial interests. **Data and material availability:** Raw and processed sequencing data for single-cell RNA-seq, bulk RNA-seq and ATAC-seq have been deposited at the European Genome-phenome Archive (EGA), which is hosted by the EBI and the CRG, under accession number EGAS00001005675. R codes used for the analysis of single-cell RNA-seq, bulk RNA-seq and ATAC-seq are available on GitHub: https://github.com/cancerbits/ikzf2. Raw data from LC-MS will be available in Massive (identifier number pending).

FIGURE LEGENDS

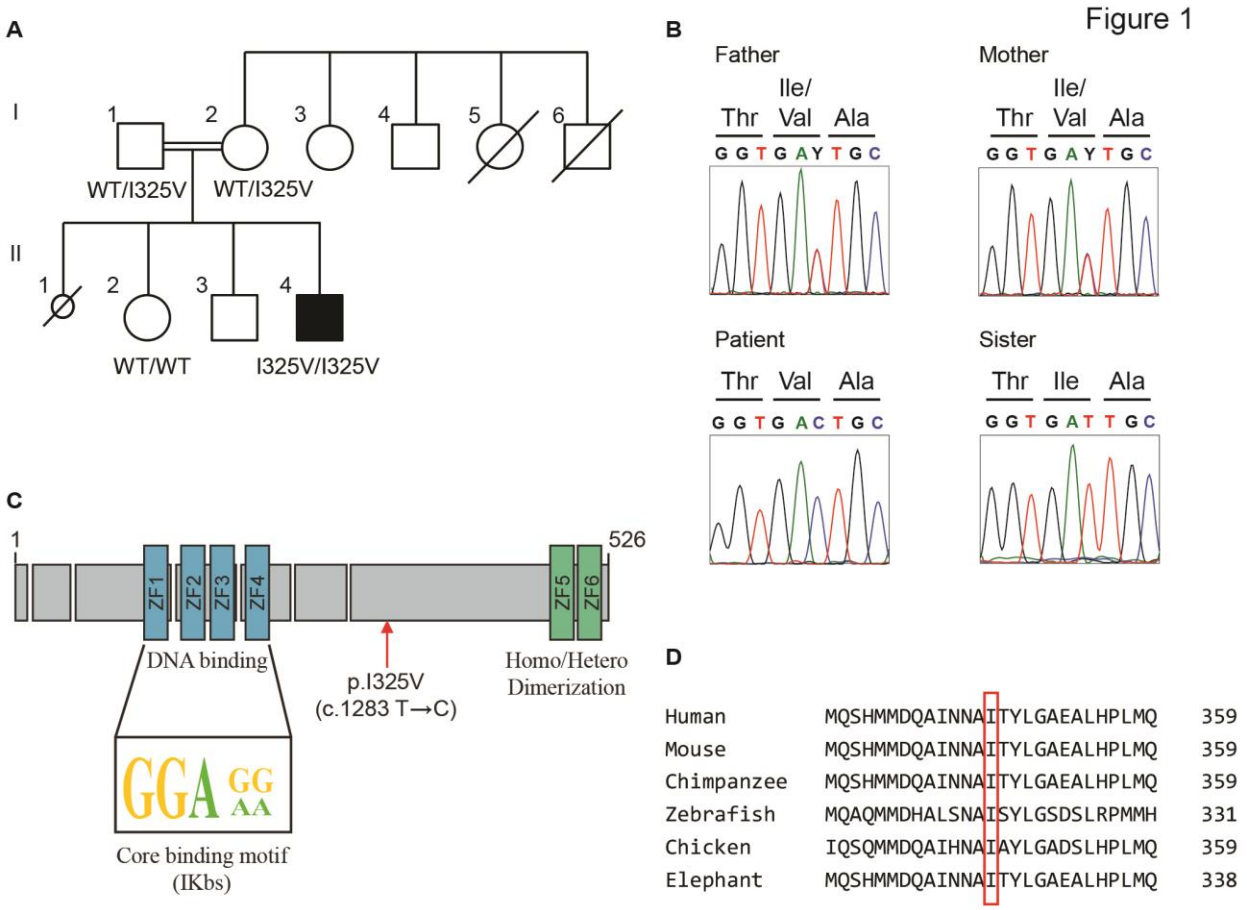

Fig. 1. Identification of a homozygous missense variant in *IKZF2*. **(A)** Family pedigree of the patient under study, showing consanguinity. The 17-year-old male patient (II-4) is the only affected member (filled square), but has a sibling who died *in utero* (small circle). **(B)** Chromatograms from Sanger sequencing showing the segregation of the C>T variant in *IKZF2* in the 4 family members, leading to an Isoleucine to Valine amino acid change. **(C)** Illustration of the Helios transcription factor, with four N-terminal zinc fingers responsible for DNA binding to the consensus sequence, and two C-terminal zinc fingers that form the homo/heterodimerization domain. Location of the missense variant (ENST00000457361.1:c.973A>G, ENSP00000410447.1:p.Ile325Val) is shown (red arrow). **(D)** Conservation of the Isoleucine amino acid at position 325 of the human transcript, across several species (red rectangular box).

Figure 2

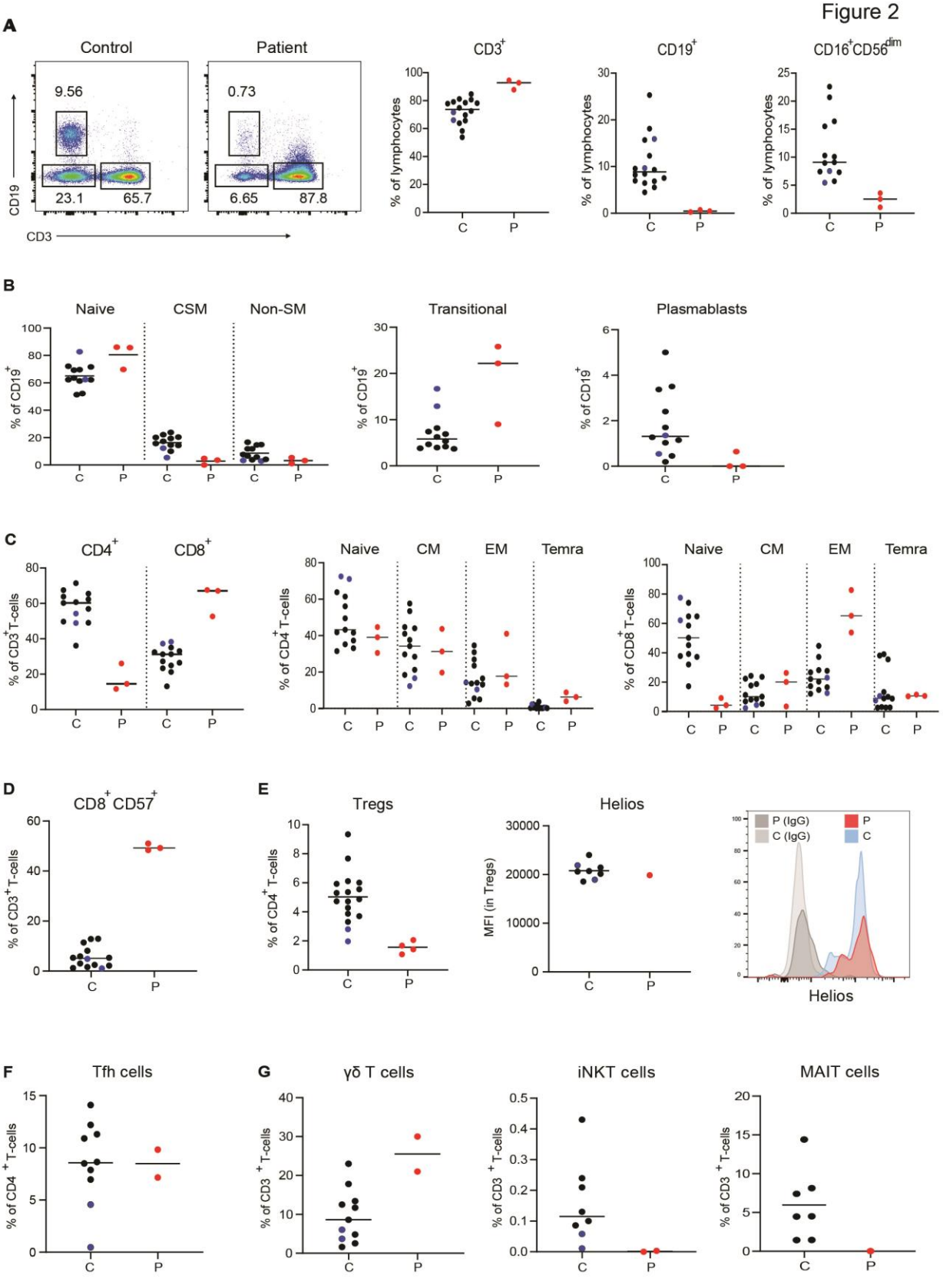
A
Control
Patient
9.56
0.73
23.1
65.7
6.65
87.8
CD19
CD3
CD3+
CD19+
CD16+CD56dim
% of lymphocytes
C
P
B
Naive
CSM
Non-SM
Transitional
Plasmablasts
% of CD19+
C
P
C
CD4+
CD8+
% of CD3+T-cells
Naive
CM
EM
Temra
% of CD4+T-cells
% of CD8+T-cells
D
CD8+CD57+
% of CD3+T-cells
E
Tregs
% of CD4+T-cells
Helios
MFI (in Tregs)
P (IgG)
C (IgG)
P
C
Helios
F
Tfh cells
% of CD4+T-cells
G
γδ T cells
iNKT cells
MAIT cells
% of CD3+T-cells

Fig. 2. Aberrant immune phenotype in patient with biallelic Helios mutation. (A) Flow cytometry plots of CD3 vs. CD19 markers in the patient and a control. The three following graphs to the right compare the percentages of T cells ($CD3^+$), B cells ($CD19^+$) and NK cells ($CD16^+CD56^{dim}$; gated on $CD3^-CD19^-$) in lymphocytes between the patient (P; red) and controls (C; adult controls are shown in black; two age-matched controls are shown in blue (n = 8-16)). **(B)** Graphs showing the frequency of naïve B cells (IgD^+CD27^-), class-switched memory B cells (CSM; IgD^-CD27^+), non-switched memory B cells (Non-SM; IgD^+CD27^+), transitional B cells ($CD21^{++}CD38^+$), and plasmablasts ($CD38^{++}CD27^+$) in patient and controls. **(C)** Graphs showing the frequency of $CD4^+$ and $CD8^+$ T cells as a percentage of $CD3^+$ T cells (left) and the frequency of $CD4^+$ (middle) and $CD8^+$ (right) naïve ($CCR7^+CD45RA^+$), central memory (CM; $CCR7^+CD45RA^-$), effector memory (EM; $CCR7^-CD45RA^-$), and terminally differentiated effector memory (Temra; $CCR7^-CD45RA^+$) cells within $CD4^+$ and $CD8^+$ populations, respectively. **(D)** Frequency of $CD8^+CD57^+$ T cells as a percentage of $CD3^+$ T cells. **(E)** Percentage of T_{regs} ($CD25^+FOXP3^+$) within the $CD4^+$ T-cell population (left), the expression of Helios shown as the mean fluorescence intensity within the T_{reg} population (center) and overlayed histograms showing Helios expression in the T_{regs} of patient vs control, including an IgG control for each in grey (left). **(F)** Frequency of T-follicular helper (Tfh) cells ($CXCR5^+CD45RA^-$) as a percentage of $CD4^+$ T cells. **(G)** Percentage of γδ T cells (left), invariant natural killer T cells (iNKT; TCR-$V\alpha24^+$TCR-$V\beta11^+$; center) and mucosa-associated invariant T cells ($CD161^+$TCR $V\alpha72^+$; left) within the $CD3^+$ T-cell population. The patient's values were taken at two time-points (13 and 14 years).

Figure 3

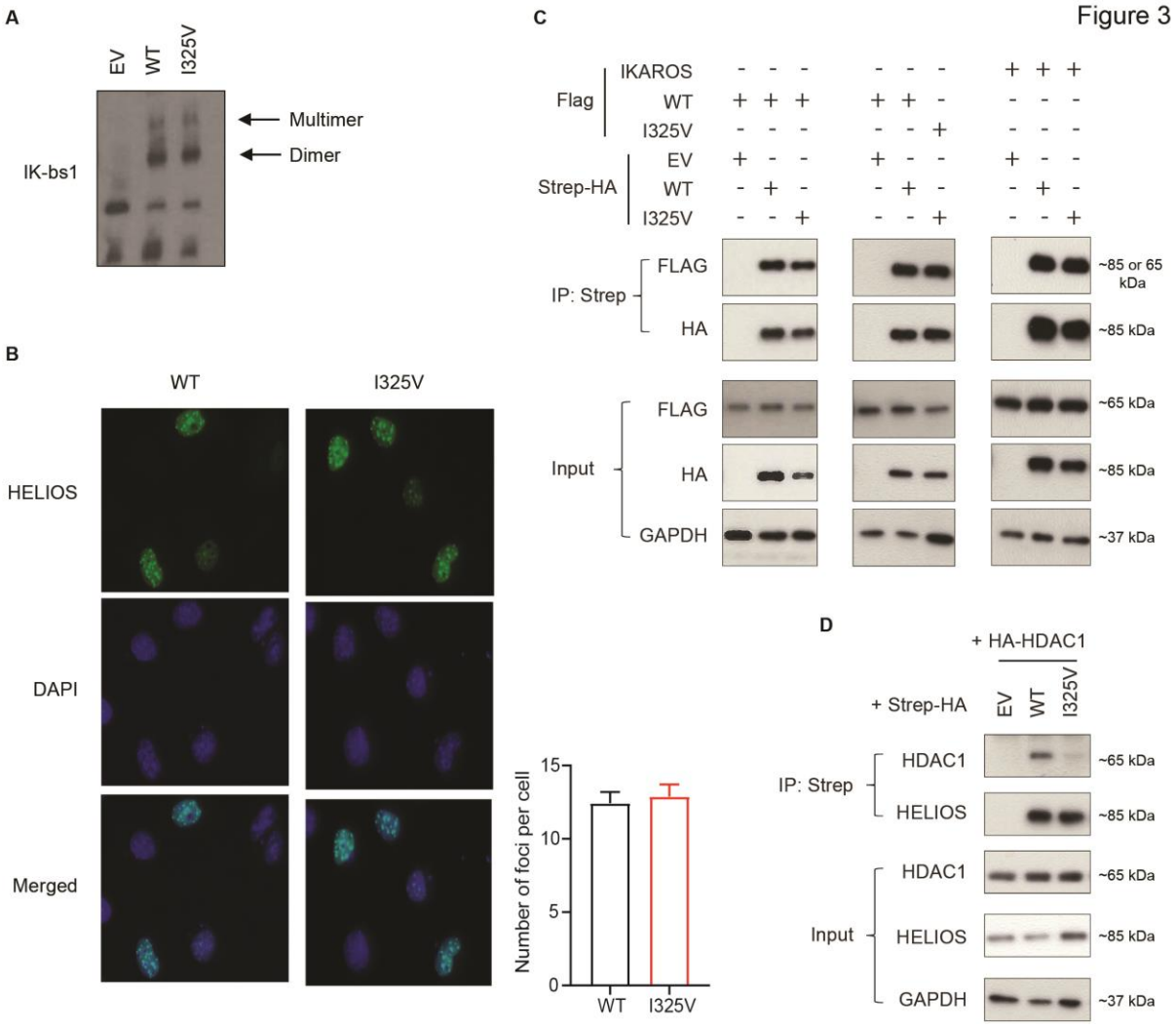
A
EV
WT
I325V
IK-bs1
Multimer
Dimer
B
WT
I325V
HELIOS
DAPI
Merged
Number of foci per cell
15
10
5
0
WT
I325V
C
IKAROS
Flag
WT
I325V
Strep-HA
EV
WT
I325V
IP: Strep
FLAG
HA
~85 or 65 kDa
~85 kDa
Input
FLAG
HA
GAPDH
~65 kDa
~85 kDa
~37 kDa
D
+ HA-HDAC1
+ Strep-HA
EV
WT
I325V
IP: Strep
HDAC1
HELIOS
~65 kDa
~85 kDa
Input
HDAC1
HELIOS
GAPDH
~65 kDa
~85 kDa
~37 kDa

Fig. 3. Effects of p.I325V mutation on Helios function. (A) Electromobility shift assay (EMSA) showing the ability of Helios WT and I325V mutant to form dimers and multimers (arrows) and bind to the IK-bs1 probe, an Ikaros consensus-binding sequence. Representative image of 7 independent experiments; EV: empty vector. **(B)** Immunofluorescence staining of NIH3T3 cells transfected with Helios WT or mutant using an anti-Helios antibody, showing the formation of foci at pericentromeric heterochromatin regions. Graph on the right shows the quantification of number of foci per cell (n = 239-422). Results represent 3 independent experiments, unpaired t-test was done showing no significant difference. **(C)** Co-immunoprecipitation (Co-IP) experiments following co-transfection of HEK293T cells with Strep-HA-Helios WT, I325V mutant or an EV together with FLAG-Helios-WT, mutant or Ikaros. IP was performed with Strep-beads and Western blot analysis was done by running both the IP and whole cell lysate (input) on a gel and blotting with HA, FLAG and GAPDH antibodies. Results are representative of 3-5 independent experiments. **(D)** Co-IP as in (C) after co-transfection with HA-HDAC1 and blotting with HDAC1 and Helios antibodies. Blot representative of 6 independent experiments.

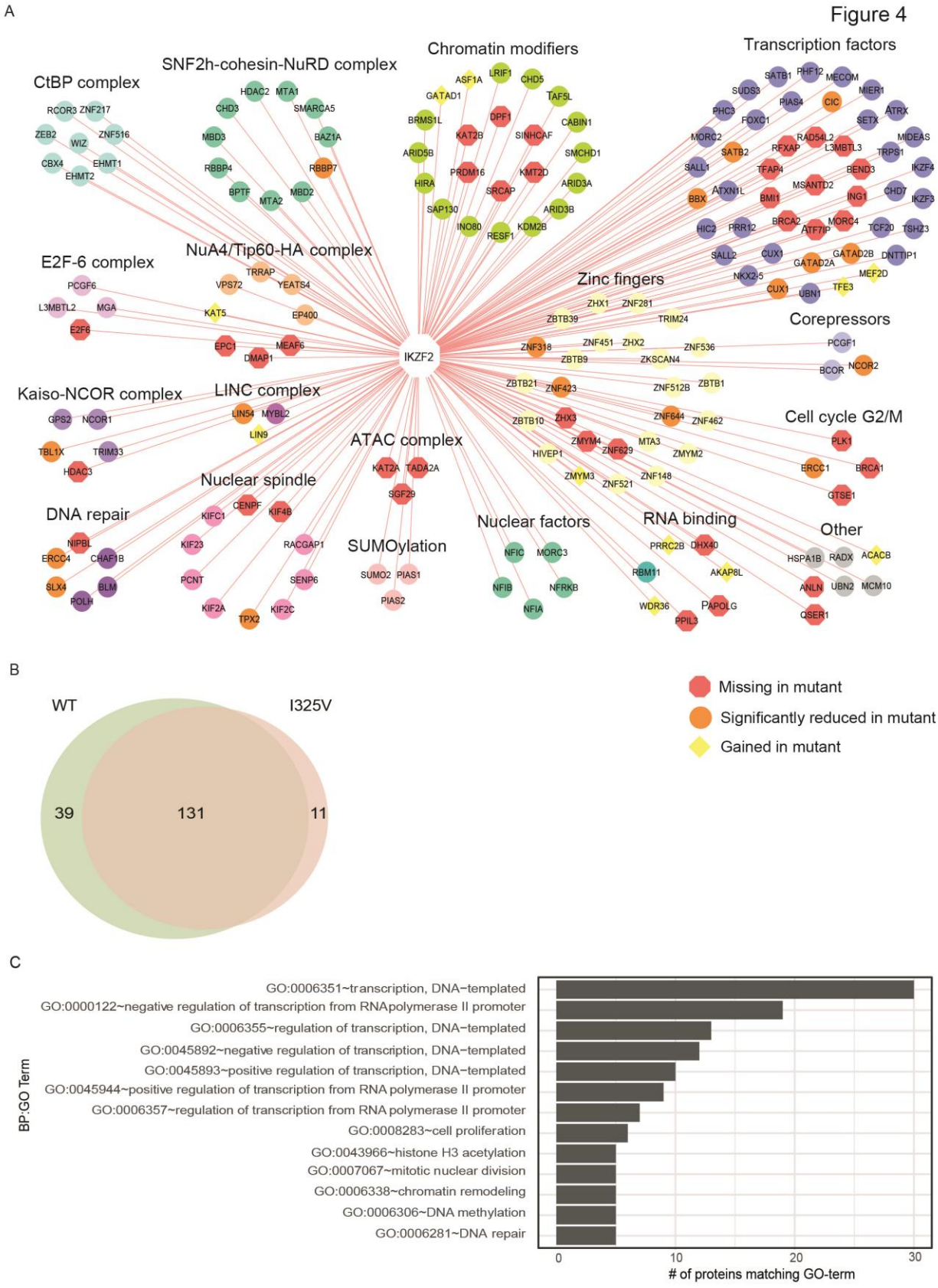
A
Figure 4
CtBP complex
RCOR3
ZNF217
ZEB2
WIZ
ZNF516
CBX4
EHMT1
EHMT2
SNF2h-cohesin-NuRD complex
HDAC2
MTA1
CHD3
SMARCA5
MBD3
BAZ1A
RBBP4
RBBP7
BPTF
MTA2
MBD2
Chromatin modifiers
ASF1A
LRIF1
CHD5
GATAD1
TAF5L
BRMS1L
DPF1
CABIN1
KAT2B
SINHCAF
ARID5B
SMCHD1
PRDM16
KMT2D
HIRA
SRCAP
ARID3A
SAP130
ARID3B
ING0
KDM2B
RESF1
Transcription factors
SATB1
PHF12
MECOM
SUDS3
MIER1
PIAS4
CIC
PHC3
FOXC1
ATRX
SETX
MORC2
RAD54L2
MIDEAS
RFXAP
L3MBTL3
SATB2
TRPS1
SALL1
TFAP4
BEND3
IKZF4
ATXN1L
MSANTD2
BBX
BMI1
ING1
CHD7
IKZF3
HIC2
PRR12
BRCA2
ATF7IP
MORC4
TCF20
TSHZ3
SALL2
CUX1
GATAD2B
DNTTIP1
GATAD2A
NKX2-5
MEF2D
CUX1
UBN1
TFE3
NuA4/Tip60-HA complex
TRRAP
VPS72
YEATS4
KAT5
EP400
EPC1
MEAF6
DMAP1
E2F-6 complex
PCGF6
L3MBTL2
MGA
E2F6
Zinc fingers
ZHX1
ZNF281
ZBTB39
TRIM24
Corepressors
PCGF1
BCOR
NCOR2
IKZF2
ZNF318
ZNF451
ZHX2
ZNF536
ZBTB9
ZKSCAN4
ZBTB21
ZNF423
ZNF512B
ZBTB1
Kaiso-NCOR complex
GPS2
NCOR1
TBL1X
TRIM33
HDAC3
LINC complex
LIN54
MYBL2
LIN9
ZBTB10
ZHX3
ZNF644
ZNF462
Cell cycle G2/M
PLK1
ERCC1
BRCA1
GTSE1
ATAC complex
KAT2A
TADA2A
SGF29
ZMYM4
MTA3
ZNF629
HIVEP1
ZMYM2
ZMYM3
ZNF521
ZNF148
Nuclear spindle
CENPF
KIFC1
KIF4B
KIF23
RACGAP1
PCNT
SENP6
KIF2A
TPX2
KIF2C
DNA repair
NIPBL
ERCC4
CHAF1B
SLX4
BLM
POLH
SUMOylation
SUMO2
PIAS1
PIAS2
Nuclear factors
NFIC
MORC3
NFIB
NFRKB
NFIA
RNA binding
PRRC2B
DHX40
RBM11
AKAP8L
WDR36
PAPOLG
PPIL3
Other
HSPA1B
RADX
ACACB
ANLN
UBN2
MCM10
QSER1
B
WT
I325V
39
131
11
Missing in mutant
Significantly reduced in mutant
Gained in mutant
C
BP:GO Term
GO:0006351~transcription, DNA−templated
GO:0000122~negative regulation of transcription from RNApolymerase II promoter
GO:0006355~regulation of transcription, DNA−templated
GO:0045892~negative regulation of transcription, DNA−templated
GO:0045893~positive regulation of transcription, DNA−templated
GO:0045944~positive regulation of transcription from RNA polymerase II promoter
GO:0006357~regulation of transcription from RNA polymerase II promoter
GO:0008283~cell proliferation
GO:0043966~histone H3 acetylation
GO:0007067~mitotic nuclear division
GO:0006338~chromatin remodeling
GO:0006306~DNA methylation
GO:0006281~DNA repair
0
10
20
30
# of proteins matching GO-term

Fig. 4. Mutant Helios shows altered interactome. (A) Representation of all high-confidence BioID interactors of Helios^{WT} and Helios^{I325V}, clustered into modules based on the protein complexes they are associated with using CORUM (*45*). Interactors that are missing, gained or significantly reduced in Helios^{I325V} are indicated in red, yellow or orange respectively. **(B)** Venn diagram representing number of shared, lost and gained interactors by Helios^{I325V} compared to Helios^{WT}. **(C)** Gene ontology (GO) analysis using Enrichr (*46*) for biological processes of the missing and significantly reduced (≥ 25% reduction) proteins from (A), with bars indicating the number of proteins associated with each GO term.

Figure 5

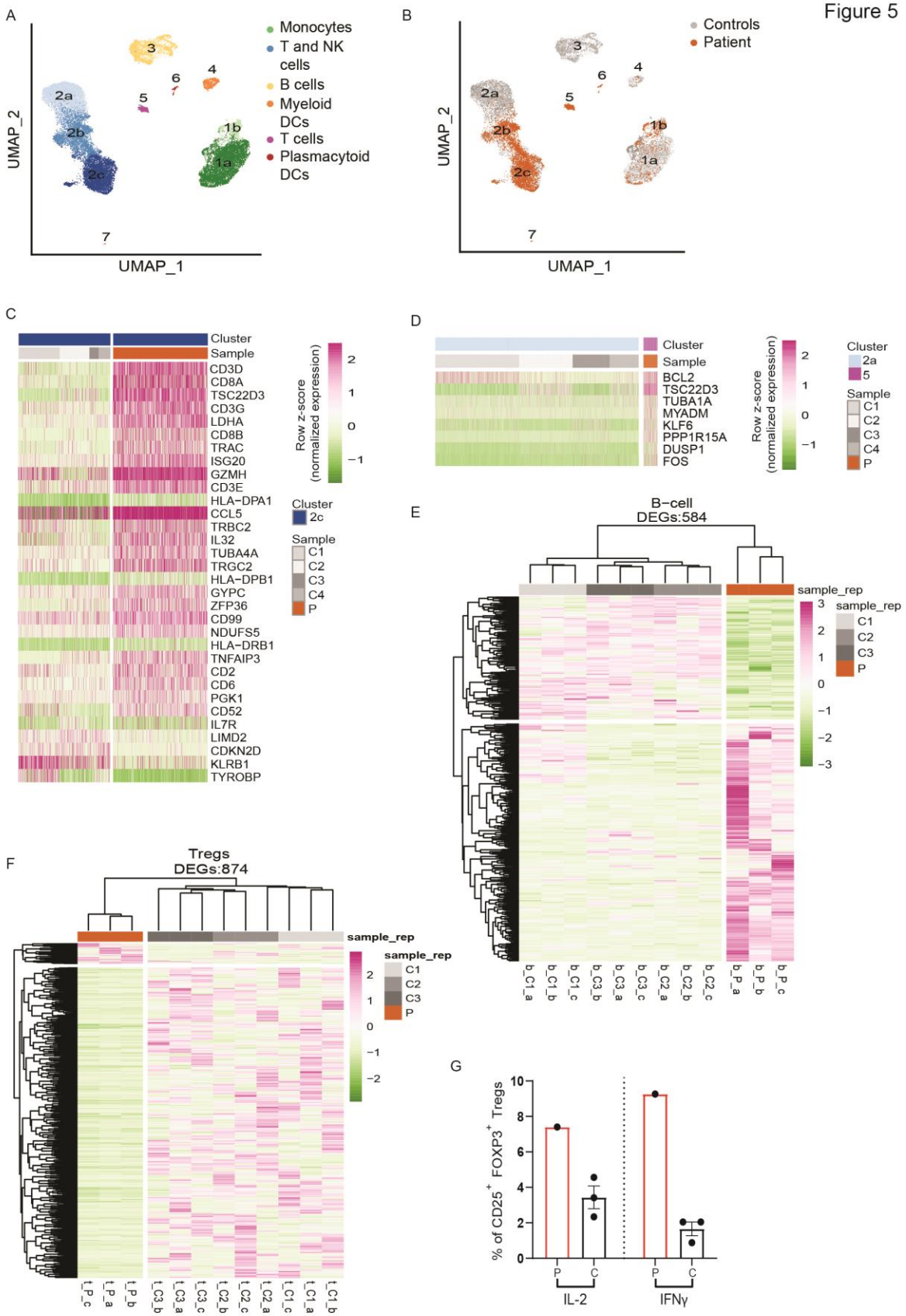
A
Monocytes
T and NK cells
B cells
Myeloid DCs
T cells
Plasmacytoid DCs
UMAP_2
UMAP_1
B
Controls
Patient
C
Cluster
Sample
CD3D
CD8A
TSC22D3
CD3G
LDHA
CD8B
TRAC
ISG20
GZMH
CD3E
HLA-DPA1
CCL5
TRBC2
IL32
TUBA4A
TRGC2
HLA-DPB1
GYPC
ZFP36
CD99
NDUFS5
HLA-DRB1
TNFAIP3
CD2
CD6
PGK1
CD52
IL7R
LIMD2
CDKN2D
KLRB1
TYROBP
Row z-score (normalized expression)
D
BCL2
TSC22D3
TUBA1A
MYADM
KLF6
PPP1R15A
DUSP1
FOS
E
B-cell
DEGs:584
sample_rep
F
Tregs
DEGs:874
G
% of CD25+ FOXP3+ Tregs
IL-2
IFNγ

Fig. 5. Altered transcriptional state of Helios-mutant patient PBMCs. (A) Low-dimensional projection (UMAP plot) of the combined scRNA-seq dataset comprising 25,081 cells from the patient (P) and 4 controls (2 adults, C1: male, C2: female; and 2 age-matched, C3: male, C4: female). Numbers indicate clusters (graph-based clustering) and colors correspond to cell type (manual curation). **(B)** UMAP plot (same coordinates as in panel A) showing the distribution of patient cells (orange) within the clusters compared to controls (shades of grey). **(C)** Heatmap showing differentially expressed genes within cluster 2c between cells from the patient and those from all four controls (FDR < 0.05, log fc > 0.25). **(D)** Heatmap showing differentially expressed genes between cluster 2a and cluster 5. The complete results of the marker genes and differential gene expression analysis for each comparison are available in tables S5 and S6. **(E and F)** Heatmap showing differentially expressed genes between sorted **(E)** naïve B cells ($CD19^{+}CD27^{-}IgD^{+}$) and **(F)** Tregs ($CD4^{+}CD25^{hi}CD127^{-}$) from PBMCs of the patient and three male healthy controls, with three replicates each (padj<0.05, |log2FoldChange| >= 1). **(G)** Cytokine production assay, measuring intracellular IL-2 and IFNγ in Tregs (gated for $CD4^{+}CD25^{+}FOXP3^{+}$) after 6 hours of stimulation with PMA and ionomycin.

Figure 6

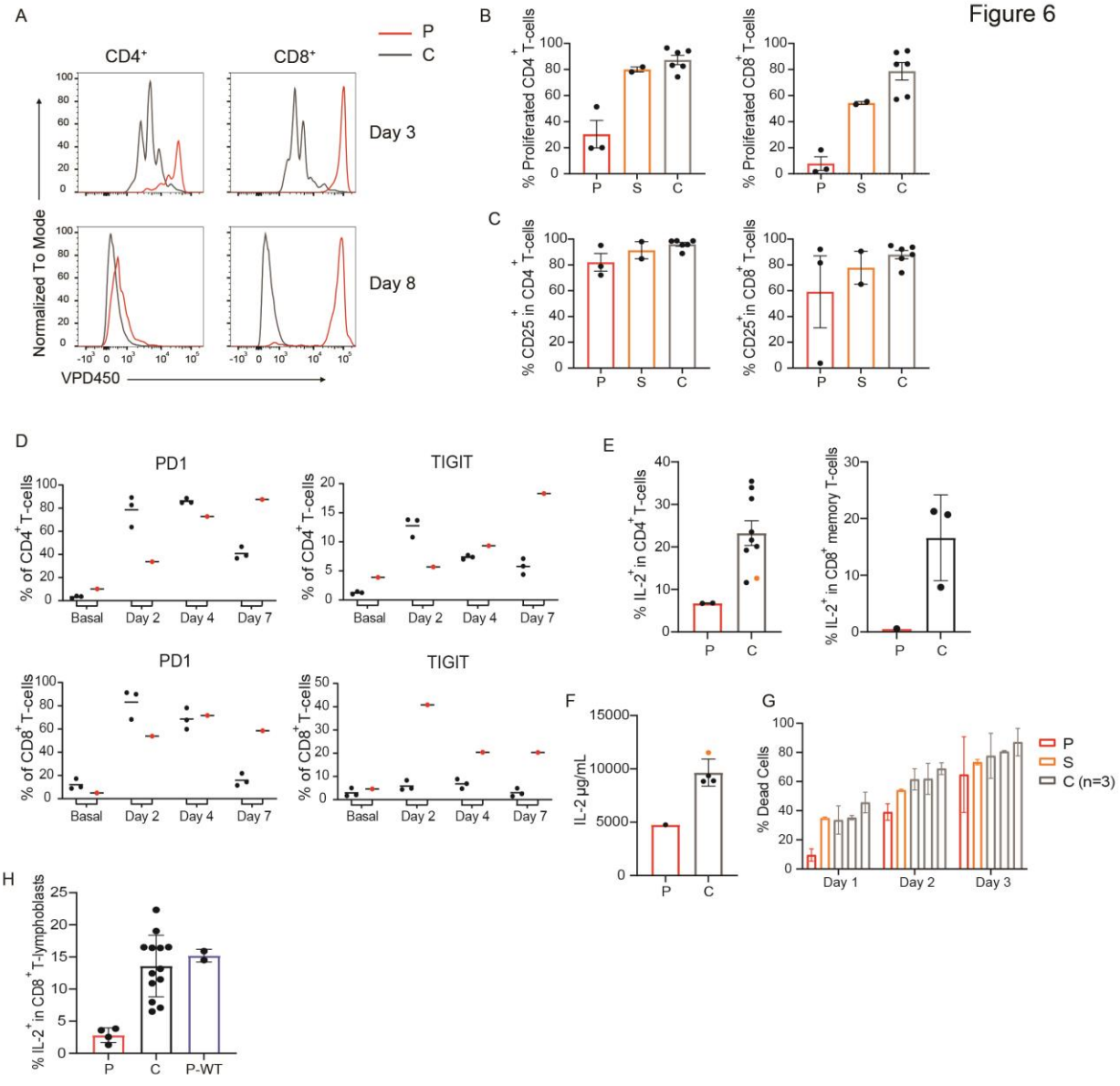
A
CD4+
CD8+
P
C
Day 3
Day 8
Normalized To Mode
VPD450
B
% Proliferated CD4+ T-cells
% Proliferated CD8+ T-cells
P
S
C
C
% CD25+ in CD4+ T-cells
% CD25+ in CD8+ T-cells
D
PD1
TIGIT
% of CD4+ T-cells
% of CD8+ T-cells
Basal
Day 2
Day 4
Day 7
E
% IL-2+ in CD4+ T-cells
% IL-2+ in CD8+ memory T-cells
F
IL-2 µg/mL
G
% Dead Cells
Day 1
Day 2
Day 3
P
S
C (n=3)
H
% IL-2+ in CD8+ T-lymphoblasts
P-WT

Fig. 6. Patient T cells have defective proliferation and reduced IL-2 production. (A) Representative histograms displaying the dilution of the violet proliferation dye (VPD450) in $CD4^+$ and $CD8^+$ T cells from the patient and a control after 3 days and 8 days of stimulation with CD3/CD28 beads, P: patient, C: control. **(B)** Summary bar graphs showing the percentage of proliferated or (C) percentage of $CD4^+$ and $CD8^+$ T cells that have upregulated CD25 at day 3, upon stimulation with CD3/CD28 beads, in the patient (P; red), sister (S; orange) and controls (C; black, n = 2-3). Two-three independent experiments were done. **(D)** Summary graphs showing the percentage of $CD4^+$ or $CD8^+$ T cells that have upregulated the check-point inhibitor PD-1 and TIGIT after stimulation with CD3/CD28 beads at basal state (before stimulation), day 2, day 4 and day 7 after stimulation. **(E)** Bar graphs showing the percentage of $CD4^+$ and memory $CD8^+$ T cells that produced IL-2 after stimulation of PBMCs with PMA/ionomycin for 5 hours. **(F)** Amount of IL-2 (in µg/mL) released into the media after stimulating PBMCs with CD3/CD28 Beads for 24 hours. The sister (orange) is included with the controls in (E) and (F) (C; n = 3-8). IL-2 production in $CD4^+$ T cells of the patient has been done in two independent experiments. **(G)** Bar graphs showing the percentage of cell death in T-lymphoblasts, measured by Annexin V and PI staining, after withdrawing IL-2 from the growth media. Results from (G) are from two experiment. **(H)** Percentage of $CD8^+$ T cells expressing IL-2 after stimulation T-lymphoblasts with PMA/ionomycin for 20 hours, including the T-lymphoblast clone that has the *IKZF2* gene CRISPR-edited to express WT alleles (P-WT, blue bar on graph). Each data-point represents and independent experiment. Error bars in all summary bar graphs show the mean with standard error of mean.

Figure 7

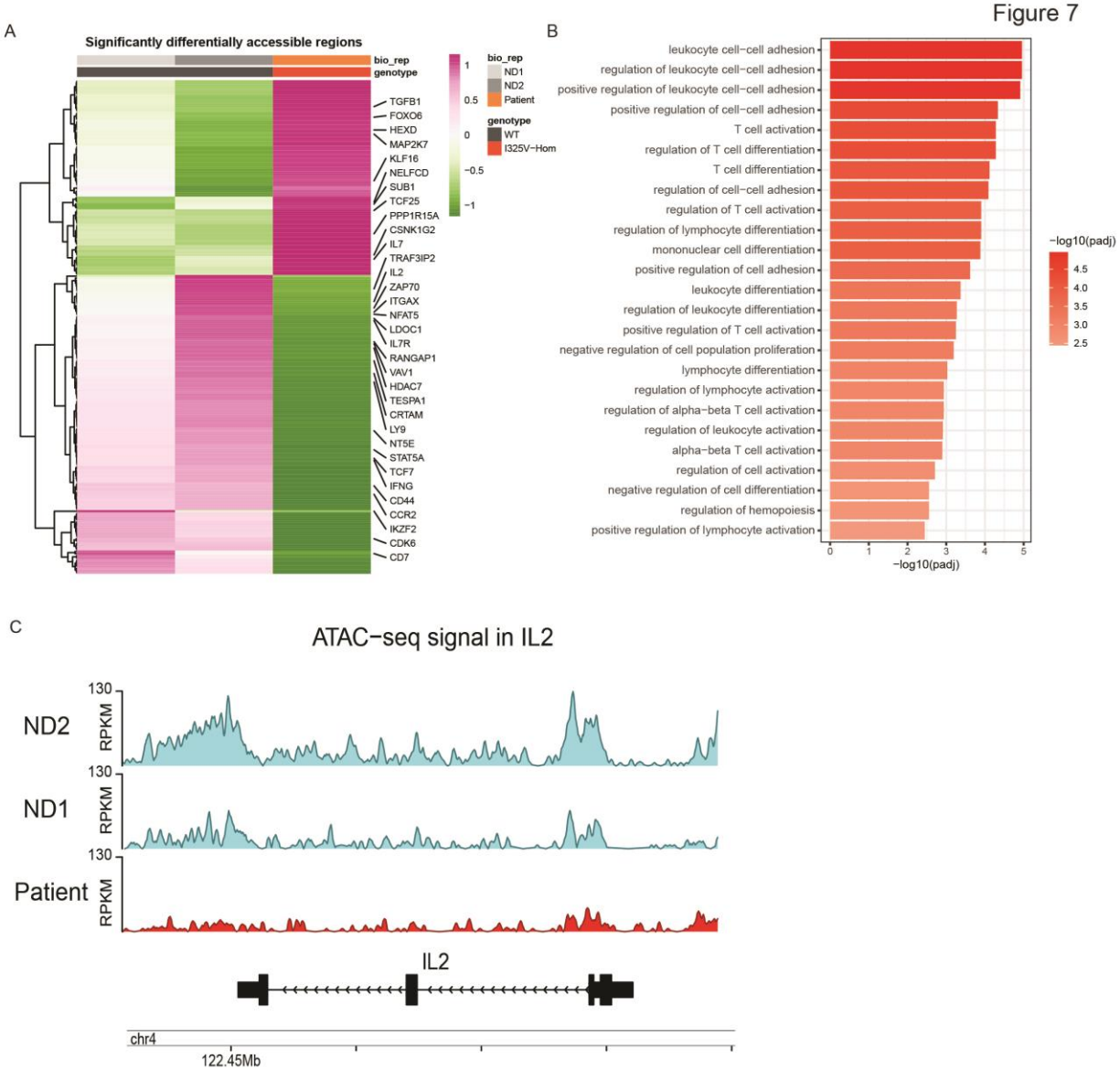
A
Significantly differentially accessible regions
bio_rep
genotype
TGFB1
FOXO6
HEXD
MAP2K7
KLF16
NELFCD
SUB1
TCF25
PPP1R15A
CSNK1G2
IL7
TRAF3IP2
IL2
ZAP70
ITGAX
NFAT5
LDOC1
IL7R
RANGAP1
VAV1
HDAC7
TESPA1
CRTAM
LY9
NT5E
STAT5A
TCF7
IFNG
CD44
CCR2
IKZF2
CDK6
CD7
1
0.5
0
−0.5
−1
bio_rep
ND1
ND2
Patient
genotype
WT
I325V−Hom
B
leukocyte cell−cell adhesion
regulation of leukocyte cell−cell adhesion
positive regulation of leukocyte cell−cell adhesion
positive regulation of cell−cell adhesion
T cell activation
regulation of T cell differentiation
T cell differentiation
regulation of cell−cell adhesion
regulation of T cell activation
regulation of lymphocyte differentiation
mononuclear cell differentiation
positive regulation of cell adhesion
leukocyte differentiation
regulation of leukocyte differentiation
positive regulation of T cell activation
negative regulation of cell population proliferation
lymphocyte differentiation
regulation of lymphocyte activation
regulation of alpha−beta T cell activation
regulation of leukocyte activation
alpha−beta T cell activation
regulation of cell activation
negative regulation of cell differentiation
regulation of hemopoiesis
positive regulation of lymphocyte activation
0
1
2
3
4
5
−log10(padj)
−log10(padj)
4.5
4.0
3.5
3.0
2.5

C
ATAC−seq signal in IL2
ND2
ND1
Patient
RPKM
130
IL2
chr4
122.45Mb

Fig. 7. Helios^{I325V} leads to global chromatin changes and less accessibility for the *Il2* locus upon T cell activation (A) Heatmap of significantly differentially accessible regions in normal donor- and patient-derived T lymphoblast cells upon T cell activation. Highlighted are key genes that have been shown to be involved in IL-2 signaling. Values are scored across rows, z-scores (1 indicates that regions of the corresponding genes are transcriptionally accessible, whereas –1 indicates that the regions are not accessible). (**B**) Top 25 significantly (biological significance, at abs(log2FC) > log2(1.5) and withing 1000bp of TSS) enriched GOBP terms for genes from less chromatin accessible regions in patient-derived cells compared to normal donors. (**C**) Comparison of ATAC-seq signal tracks for *Il2* gene locus between patient and two normal donors. Reads per kilobase per million mapped (RPKM) reads normalized tracks.

SUPPLEMENTARY MATERIAL

Methods

Whole exome sequencing (WES)

For WES, a TrueSeq Rapid Exome kit as well as the Illumina HiSeq3000 system and the cBot cluster generation instruments were used as previously described (*70*). Briefly, reads were aligned to the human genome version 19 by means of the Burrows-Wheeler Aligner (BWA). The variant effector predictor (VEP) was used for annotating single nucleotide variants (SNVs) and insertions/deletions lists. The list was then filtered to obtain variants with a minor allele frequency (MAF) <0.01 in 1,000 Genomes, gnomAD, and dbSNP build 149. After further filtering steps for nonsense, missense, and splice-site variants using VCF.Filter software (*71*), an internal database was used to filter out recurrent variants. Moreover, variants are prioritized using tools, such as SIFT, Polyphen-2 and the combined annotation dependent depletion (CADD) score (*72*), that predict the deleteriousness of a present variant (table S2).

Sanger sequencing

Genomic DNA from the patient (II-4), father (I-1), mother (I-2) and sister (II-2) were used to validate and segregate the *IKZF2* variant by Sanger sequencing (fig. 1A-B). DNA from other family members was not available. The following primers were designed for amplification and sequencing: Forward: 5'- GGGTCGACTCTTTGGTCTGA-3', Reverse: 5'-CTTCCAGGGGAAAAGCTCAT-3'.

Plasmids

Human *IKZF2* (NM_016260; Origene, RC214813), *IKZF1* (NM_006060 (*27*)) and *IKZF3* (NM_012481; GenScript, Ohu21008D) cDNA were synthesized and subcloned into a CMV driven

C-terminal Myc-Flag-tagged mammalian expression vector (Origene or GenScript), or into a pTO-Strep-HA plasmid by Gateway™ cloning (ThermoFisher Scientific), following manufacturer's protocol, to generate an N-terminal Streptavidin-Hemagglutinin tag. The patient variant was generated on *IKZF2* vectors using the AccuPrime Pfx DNA Polymerase followed by DpnI treatment. HA-HDAC1 (NM_004964.2; Sino Biological, HG11486-CY) and GFP-SUMO2 (pCMV3-N-GFPSpark-Sumo2; Sino Biological, HG13443-ANG) were purchased. *IKZF4* (NM_022465) and *HDAC3* (NM_003883) cDNA were amplified and cloned into a pcDNA-C-Myc vector, to generate C-terminal Myc-tagged coding sequences by Gateway™ cloning.

Sumoylation

To assess the ability of Helios variants to be sumoylated by SUMO2, HEK293T cells were transfected with Strep-HA-Helios WT or mutant together with GFP-SUMO2 for 24 hours. Cells were washed with PBS once and lysed in sumoylation IP buffer (50 mM Tris (pH 7.4), 150 mM NaCl, 2 mM EDTA, 0.5% Nonidet P-40, 1% SDS and 20 mM N-ethylmaleimide (NEM, Sigma) and Halt™ protease and phosphatase inhibitor cocktail (Sigma)) for 15 min on ice. To reduce viscosity, QIAshredder (Qiagen) was used. After centrifuging the lysates for 10 min, 13000 rpm, at 4 °C, the supernatant was saved and total 500 ug of cell lysates were incubated with an anti-HA (#3724S, CST) or normal rabbit IgG antibody (#2729, CST) together with Pierce™ Protein A/G-agarose beads (Thermo Scientific). After 2-4 hours of incubation at 4 °C on a rotating wheel, beads were washed three times with lysis buffer (50 mM Tris pH 7.4, 150 mM NaCl, 2 mM EDTA, 0.5% Triton X-100 and 0.5% NP-40). The samples were then prepared and separated on NuPAGE® Novex® 4-12% Bis-Tris Protein Gels (Life Technology) and Western blotting was performed using Sumo2 (101083-T38, Sino Biological) and HA (MMS-101P/901501, Biolegend) antibodies. Images were analyzed with Image Studio Software (Li-Cor).

Generation of T-lymphoblasts

To generate T-lymphoblasts, T cells are expanded starting from PBMCs that are plated on a layer of feeder cells (irradiated PBMCs from blood donors) in T-cell media (RPMI media (Gibco) supplemented with 5% human serum, Hepes (20 mM; Gibco), penicillin/streptomycin (10 µg/mL; Invitrogen), sodium pyruvate (1mM) and non-essential amino acids (1X; both from Gibco) with IL-2 (100 IU/mL) and PHA (1 µg/mL). Cells are split approximately every two days, adding fresh IL-2, until quiescence around day 12, when most of the experiments are performed. All healthy controls were aged 25-40 with representation of both males and females.

Calcium flux assay

T-lymphoblasts ($1x10^6$) from patient and controls were stained for 30 mins with Calcium Sensor Dye eFluor™ 514 (eBiosciences) at 37 °C. Cells were then washed, resuspended with media and incubated in a 37 °C water bath while stimulation and acquisition took place. Cells were first stimulated with 1 µg/mL anti-CD3 (OKT3, eBioscience) for 5 minutes at 37 °C, followed by a 30 second measurement using the FITC channel. Immediately after, TCR was cross-linked with the addition of 20 µg/mL of AffiniPure Goat Anti-Mouse IgG (Jackson ImmunoResearch) followed by a 3 minute measurement, and then a final addition of 1 µg/mL Ionomycin and a 1 minute measurement. Results, recorded as intensity per unit time, were normalized to the mean basal intensity before TCR cross-linking, and plotted against time.

TCR activation analysis by Western Blot

T-lymphoblasts from the patient and controls were starved in RPMI media with 0.1% human serum for 3 hours in a 37 °C incubator, at a concentration of 1 x 10^6 cells/50µl. Cells were either left unstimulated by adding 50µl of the starvation media, or stimulated with 50µl of the starvation

media containing 25µl of CD3/CD28 Dynabeads™ and IL-2 (final concentration of 100 IU/mL). The stimulation was quenched on ice, and cells were washed with ice-cold PBS. Cells were then lysed and run on a 10% SDS-PAGE for Western blotting using the following antibodies: phospho-ERK1/2 (Thr202/Tyr204; D13.14.4E), phospho-p38 (Thr180/Tyr182; D3F9), phospho-p65 (Ser536; 93H1), phospho-AKT (Ser473; D9E), AKT (40D4; all from Cell Signaling) and HSP90 α/β (F-8; Santa Cruz Biotechnology).

Smart-seq2

Frozen PBMCs from the patient and three male controls were thawn, washed in RPMI media and resuspended in sterile PBS with 0.04% bovine serum albumin (BSA). Sorting of 100 naïve B cells ($CD19^+CD27^-IgD^+$) or 30 T_{regs} ($CD4^+CD25^{hi}CD127^-$) from the live lymphocyte population into wells of a 96-well PCR-plate containing lysis buffer (0.2% (vol/vol) Triton X-100 solution with RNase inhibitor (Clontech)) was performed using the FACSAria™ Fusion (BD). cDNA synthesis and enrichment were performed according to the Smart-seq2 protocol as described previously (*53*). Library preparation was conducted on 1 ng of cDNA using the Nextera XT library preparation kit (Illumina). Sequencing was performed by the Biomedical Sequencing Facility at CeMM using the 50 bp single-read setup on the Illumina HiSeq 3000/4000 platform. Sequence reads were trimmed of sequencing adapters using trimmomatic (v 0.36) before alignment to the human reference genome (assembly: GRCh38.p13) using STAR (v 2.7.3a) (*73, 74*). Subsequent analysis was performed in R (v 4.0.2) using the same Docker container as for scRNA-seq analysis (cancerbits/dockR:mo-ikzf2-v1). Reads were aggregated known gene models (Ensembl v98) using featureCounts (v 2.2.6; default parameters, GTF.attrType="gene_name") and used as input for DESeq2 for differential analysis (v 1.28.1; default parameters, design: ~bio_rep) (*75, 20*). Lowly expressed genes (< 10 total reads across samples) were excluded before fitting the model. Results

tables comparing each healthy donor to the patient were extracted (for each cell type separately), and differentially expressed genes that maintain the same direction of regulation in at least two of the three comparisons were selected (padj<0.05, |log2FoldChange| >= 1). For heatmaps, transformed counts were retrieved via the vst function (blind = FALSE). Next, we performed functional enrichment analysis using ezRun (v 3.11.1) to query the Enrichr API (top 20 terms by combined score; databases: BioPlanet_2019, WikiPathways_2019_Human, KEGG_2019_Human, GO_Biological_Process_2018, GO_Molecular_Function_2018), and the CHEA3 API (date of access: 2021-06-06) (*46, 76*). Summary statistics, lists of differentially expressed genes, and enrichment analyses results, including both Enrichr and CHEA3, are given in Supplementary Tables S7, S8 and S9, respectively.

ATAC-seq

Assay for Transposase-Accessible Chromatin with sequencing (ATAC-seq) was used to assess chromatin accessibility in activated T-lymphoblasts of the patient compared to two normal donor controls. T-lymphoblasts were stimulated with PMA (0.2 mM) and Ionomycin (1 μg/mL) for 2 hours, and 50,000 cells were processed as described previously (*25*). Sequencing was performed by the Biomedical Squencing Facility at CeMM using the 50bp single-read setup on the Illumina HiSeq 3000/4000 platform. ATAC-seq reads were pre-processed and initial QC was done using PEPATAC (v0.8.6) (*77*) with GRCh38 genome (GCA_000001405.15). Downstream analysis was performed in R (v 4.1.0) (*78*) using a combination of tidyverse (v1.3.1) (*79*) and GenomicRanges (v1.44.0) (*80*) packages for data manipulation. Downstream quality control analysis was performed using ChIPQC (v1.28.0) (*81*) and peaks overlapping with blacklisted (GRCh38) (*82*) regions were filtered out before annotating the remaining peaks against gene features from the UCSC hg38 annotation (v3.13.0) using ChIPseeker (v1.28.3) (*83*). Next, differential accessibility

analysis was performed with DESeq2 (v1.32.0) (*84*) using count matrix generated across consensus peaks (detected in 2 and more samples). Functional enrichment analysis was performed using clusterProfiler (v4.0.0) (*85*) on genes from significantly differentially accessible regions defined as regions with abs(log2FC) > log2(1.5) and at the same time within a window of 1000bp around a TSS (*85-89*). The plot of IL2 gene tracks across samples was generated using karyoploteR (v1.18.0) (*90*).

Supplementary figures

Figure S1

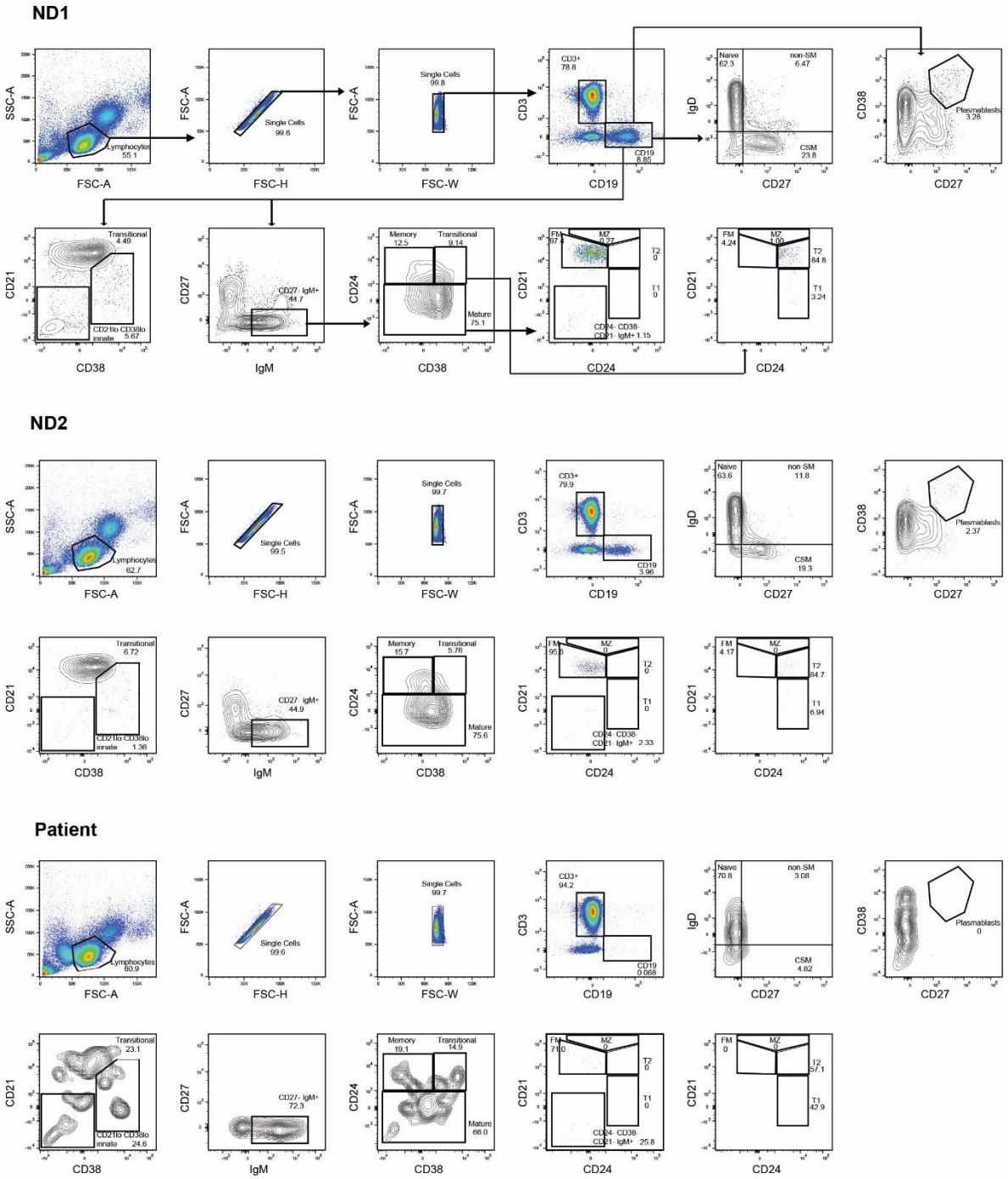

Fig. S1. Gating strategy for B cell flow cytometry. PBMCs were stained and acquired on a flow cytometer, whereby gating for the lymphocyte subset was done using forward vs. side-scatter (FSC vs SSC) in all immunophenotyping experiments. B cells of normal donors (ND1 and ND1) and patient were gated on using the CD19 marker and were analyzed further for their differential expression of the following markers: IgD/CD27 (naïve B cells IgD+CD27-; class switch memory IgD-CD27+; non-switch memory IgD+CD27+), CD27/CD38 (plasmablasts $CD27^{++}CD38^{++}$) and CD21/CD38/CD27/IgM (transitional B cells $CD21^{lo}CD38^{+}$ or alternatively $IgM^{+}CD27^{-}CD24^{+}CD38^{+}$). Transitional B cells gated on $IgM^{+}CD27^{-}CD24^{+}CD38^{+}$ were further analyzed for the expression of CD21, differentiating transitional 1 (T1, $CD21^{-}$) from transitional 2 (T2, $CD21^{+}$) B cells. Innate-like activated B cells ($CD19^{+}CD21^{lo}CD38^{lo}$) are also depicted. (MZ: marginal zone; FM: follicular memory). These gating strategies correspond to data shown in summary graphs of fig. 2B.

Figure S2

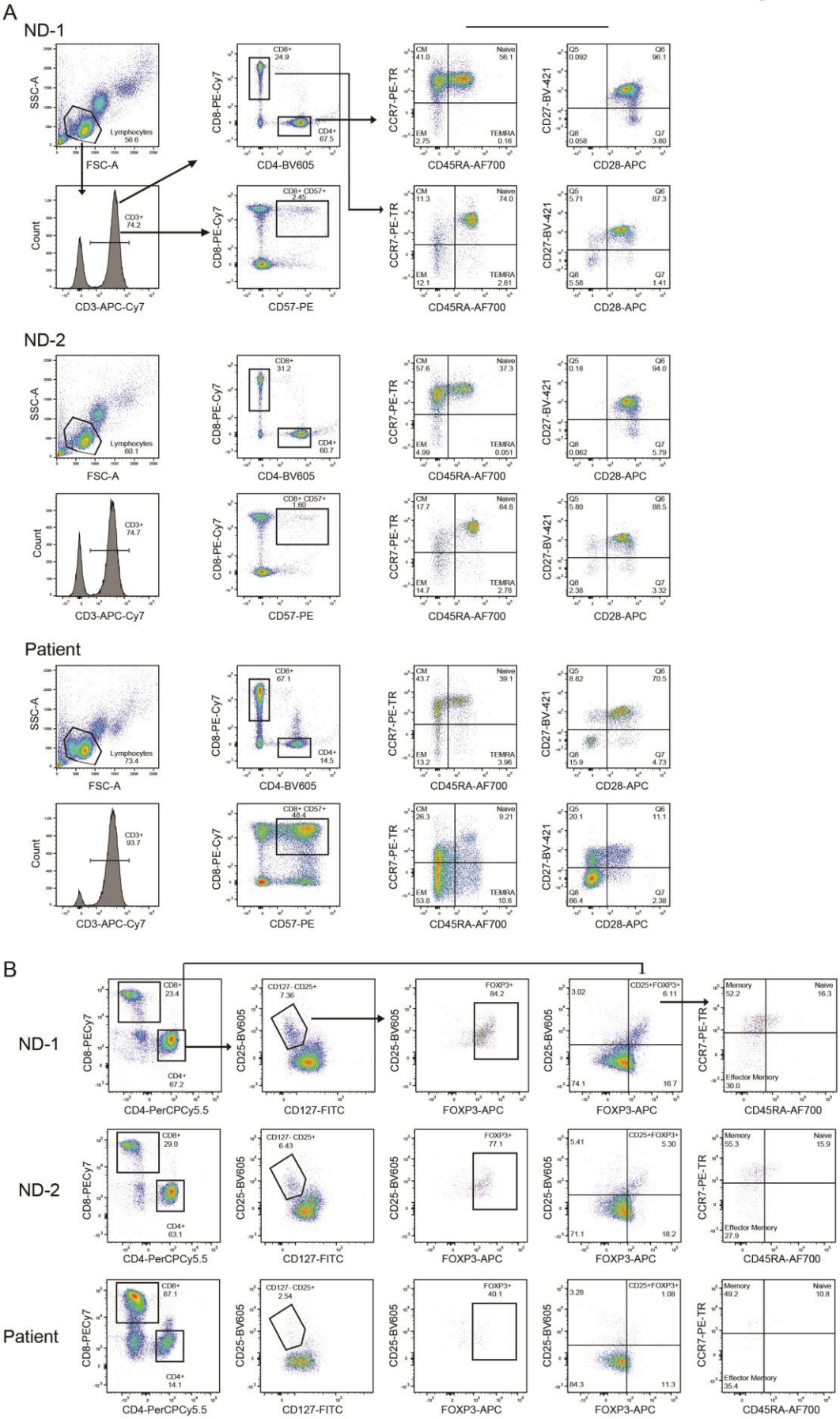
A
ND-1
SSC-A
Lymphocytes 56.6
FSC-A
Count
CD3+ 74.2
CD3-APC-Cy7
CD8+ 24.9
CD8-PE-Cy7
CD4+ 67.5
CD4-BV605
CD8+ CD57+ 2.45
CD57-PE
CM 41.0
Naive 56.1
EM 2.75
TEMRA 0.16
CCR7-PE-TR
CD45RA-AF700
Q5 0.092
Q6 96.1
Q8 0.058
Q7 3.80
CD27-BV-421
CD28-APC
CM 11.3
Naive 74.0
EM 12.1
TEMRA 2.61
Q5 5.71
Q6 87.3
Q8 5.58
Q7 1.41
ND-2
Lymphocytes 60.1
CD8+ 31.2
CD4+ 60.7
CM 57.6
Naive 37.3
EM 4.99
TEMRA 0.051
Q5 0.18
Q6 94.0
Q8 0.062
Q7 5.79
CD3+ 74.7
CD8+ CD57+ 1.60
CM 17.7
Naive 64.8
EM 14.7
TEMRA 2.78
Q5 5.80
Q6 88.5
Q8 2.38
Q7 3.32
Patient
Lymphocytes 73.4
CD8+ 67.1
CD4+ 14.5
CM 43.7
Naive 39.1
EM 13.2
TEMRA 3.96
Q5 8.82
Q6 70.5
Q8 15.9
Q7 4.73
CD3+ 93.7
CD8+ CD57+ 48.4
CM 26.3
Naive 9.21
EM 53.8
TEMRA 10.6
Q5 20.1
Q6 11.1
Q8 66.4
Q7 2.38
B
ND-1
CD8+ 23.4
CD4+ 67.2
CD8-PECy7
CD4-PerCPCy5.5
CD127- CD25+ 7.36
CD25-BV605
CD127-FITC
FOXP3+ 84.2
FOXP3-APC
3.02
CD25+FOXP3+ 6.11
74.1
16.7
Memory 52.2
Naive 16.3
Effector Memory 30.0
CCR7-PE-TR
CD45RA-AF700
ND-2
CD8+ 29.0
CD4+ 63.1
CD127- CD25+ 6.43
FOXP3+ 77.1
5.41
CD25+FOXP3+ 5.30
71.1
18.2
Memory 55.3
Naive 15.9
Effector Memory 27.9
Patient
CD8+ 67.1
CD4+ 14.1
CD127- CD25+ 2.54
FOXP3+ 40.1
3.28
CD25+FOXP3+ 1.08
84.3
11.3
Memory 49.2
Naive 10.8
Effector Memory 35.4

Fig. S2. Gating strategy for T cell flow cytometry. (A) Gating strategy for characterization of $CD4^+$ and $CD8^+$ $CD3^+$-gated T cells using CD45RA and CCR7 markers to identify naïve ($CD45RA^+CCR7^+$), central memory (CM, $CD45RA^-CCR7^+$), effector memory (EM, $CD45RA^-CCR7^+$), and the TEMRA ($CD45RA^+CCR7^+$) T-cell subsets in normal donors (ND1 and ND2) and patient samples. Markers for co-stimulatory receptors CD27/CD28 were also used, as well as the T-cell senescent marker, CD57. (**B**) Gating strategy for the identification of $CD4^+$ regulatory T-cell (T_{reg}) population. $CD4^+$ T-cells were analysed for the differential expression of CD25/CD127/FOXP3. $CD25^+CD127^-$ defines a subset of T cells that includes FOXP3-expressing T_{regs}. $CD25^+CD127^-$ T_{reg} cells were then analysed for the expression of FOXP3. T_{reg} cells gated on $CD25^+FOXP3^+$ were then analysed for the differential expression of CCR7 and CD45RA. These gating strategies correspond to data shown in summary graphs of fig. 2C, D and E.

Figure S3

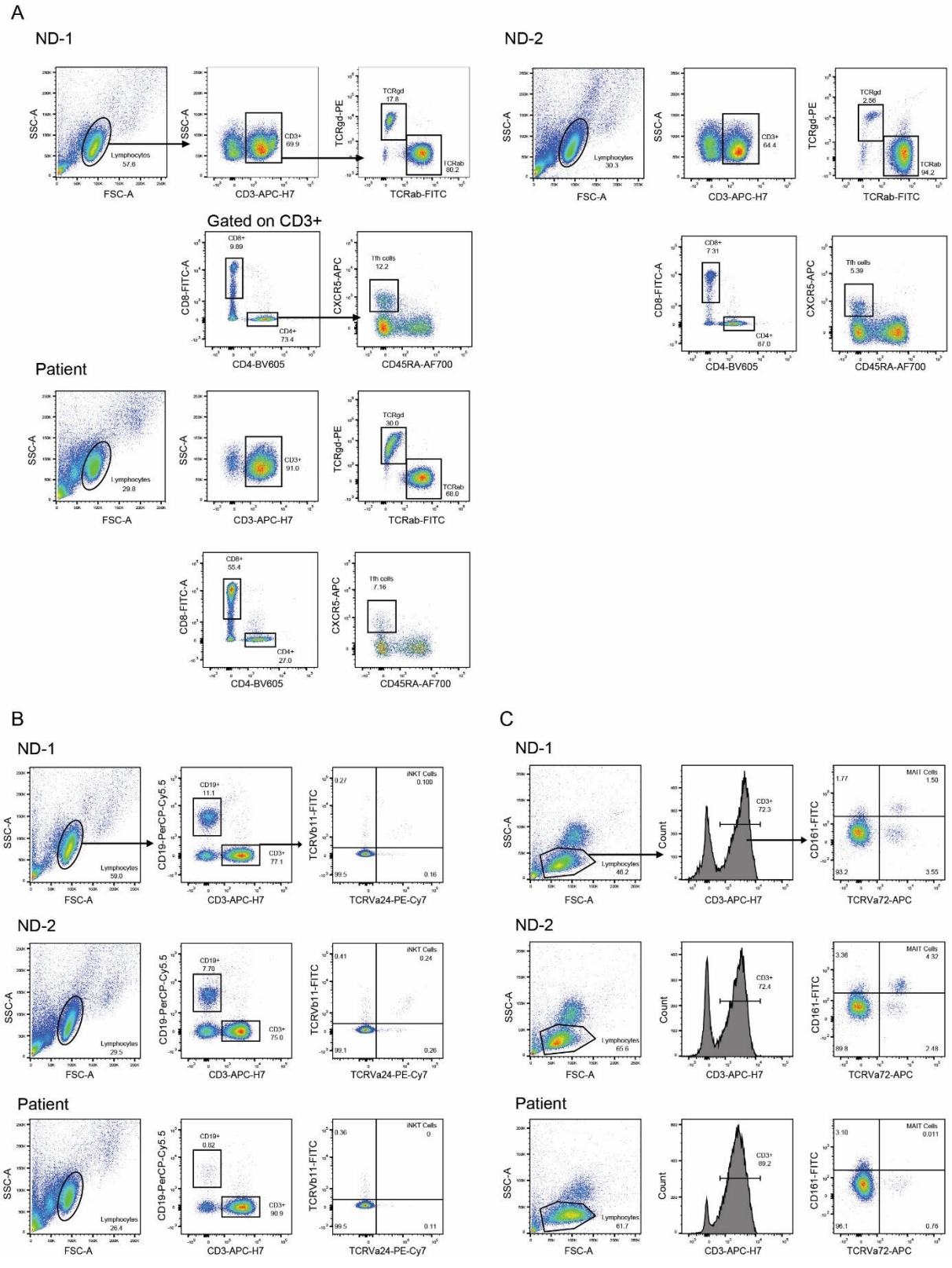
A
ND-1
SSC-A
FSC-A
Lymphocytes
57.6
CD3-APC-H7
CD3+
69.9
TCRgd-PE
TCRab-FITC
TCRgd
17.8
TCRab
80.2
Gated on CD3+
CD8-FITC-A
CD4-BV605
CD8+
9.89
CD4+
73.4
CXCR5-APC
CD45RA-AF700
Tfh cells
12.2
Patient
Lymphocytes
29.8
CD3+
91.0
TCRgd
30.0
TCRab
68.0
CD8+
55.4
CD4+
27.0
Tfh cells
7.16
ND-2
Lymphocytes
30.3
CD3+
64.4
TCRgd
2.56
TCRab
94.2
CD8+
7.31
CD4+
87.0
Tfh cells
5.39
B
ND-1
Lymphocytes
59.0
CD19-PerCP-Cy5.5
CD19+
11.1
CD3+
77.1
TCRVb11-FITC
TCRVa24-PE-Cy7
iNKT Cells
0.100
0.27
99.5
0.16
ND-2
Lymphocytes
29.5
CD19+
7.70
CD3+
75.0
iNKT Cells
0.24
0.41
99.1
0.26
Patient
Lymphocytes
26.4
CD19+
0.62
CD3+
90.9
iNKT Cells
0
0.36
99.5
0.11
C
ND-1
Lymphocytes
46.2
Count
CD3+
72.3
CD161-FITC
TCRVa72-APC
MAIT Cells
1.50
1.77
93.2
3.55
ND-2
Lymphocytes
65.6
CD3+
72.4
MAIT Cells
4.32
3.36
89.8
2.48
Patient
Lymphocytes
61.7
CD3+
89.2
MAIT Cells
0.011
3.10
96.1
0.76

Fig. S3. Gating strategy for the identification of CD4+ folicullar helper, iNKT and MAIT cells by flow cytometry. (A) Lymphocytes gated on $CD3^+$ were analysed for the expression of CD8/CD4. $CD4^+$ T-cells were then analysed for the expression of CXCR5/CD45RA to identify CXCR5+CD45RA- folicullar helper T-cells. (**B**) Lymphocytes gated on CD3 were analysed for their expression of both TCRVβ11 and TCRVα24, which defines invariant natural killer T (iNKT) cells. (C) Lymphocytes gated on $CD3^+$ T cells were analysed for the expression of CD161/TCRVα72. $CD3^+CD161^+TCRV\alpha72^+$ represents mucosa-associated invariant T (MAIT) T-cells. These gating strategies correspond to summary graphs in fig. 2F and G.

Figure S4

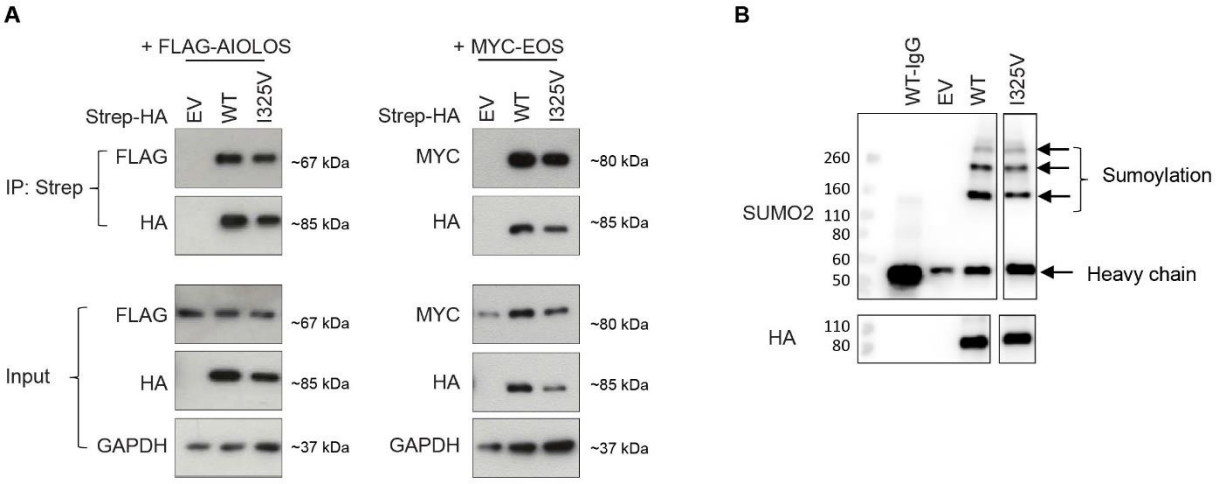
A
+ FLAG-AIOLOS
+ MYC-EOS
Strep-HA
EV
WT
I325V
IP: Strep
FLAG
HA
MYC
Input
GAPDH
~67 kDa
~80 kDa
~85 kDa
~37 kDa
B
WT-IgG
SUMO2
260
160
110
80
60
50
Sumoylation
Heavy chain

Fig. S4. Interaction with other Ikaros members and sumoylation. (A) Co-immunoprecipitation (Co-IP) experiments following co-transfection of HEK293T cells with Strep-HA-Helios WT, I325V mutant or an empty vector (EV) together with FLAG-Aiolos or MYC-Eos. IP was performed with Strep-beads and Western blot analysis was done by running both the IP and whole cell lysate (input) on a gel and blotting with HA, FLAG, MYC and GAPDH antibodies. Results are representative of 1-2 independent experiments. **(B)** Blot showing the result of a sumoylation assay after co-transfecting HEK293T cells with Strep-HA-Helios WT or I325V mutant and GFP-SUMO2, immuneprecipitating the lysate with HA or IgG antibodies and running a Western blot to blot for SUMO2 and HA. Representative of 4 independent experiments.

Figure S5

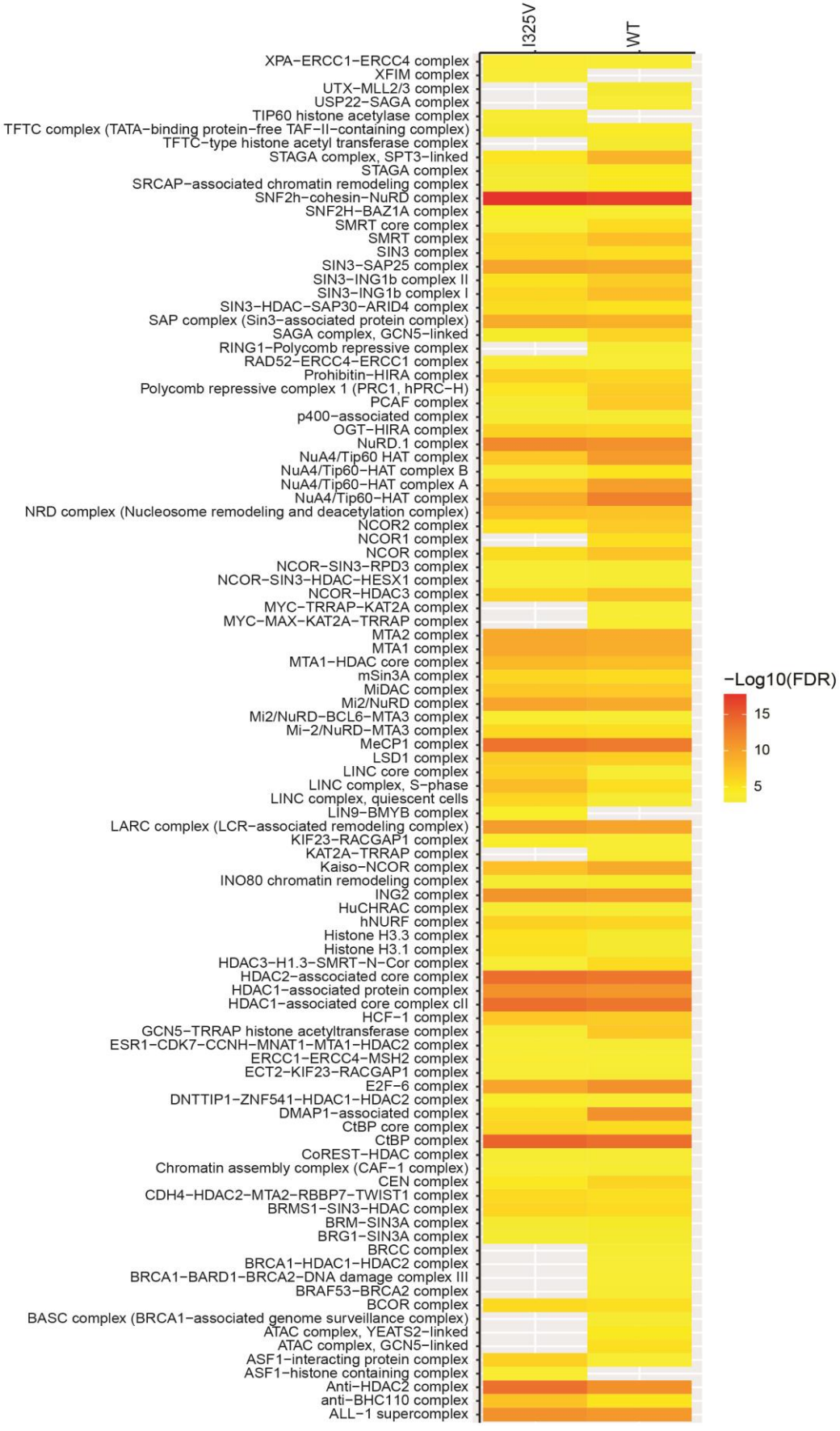
I325V
WT
XPA−ERCC1−ERCC4 complex
XFIM complex
UTX−MLL2/3 complex
USP22−SAGA complex
TIP60 histone acetylase complex
TFTC complex (TATA−binding protein−free TAF−II−containing complex)
TFTC−type histone acetyl transferase complex
STAGA complex, SPT3−linked
STAGA complex
SRCAP−associated chromatin remodeling complex
SNF2h−cohesin−NuRD complex
SNF2H−BAZ1A complex
SMRT core complex
SMRT complex
SIN3 complex
SIN3−SAP25 complex
SIN3−ING1b complex II
SIN3−ING1b complex I
SIN3−HDAC−SAP30−ARID4 complex
SAP complex (Sin3−associated protein complex)
SAGA complex, GCN5−linked
RING1−Polycomb repressive complex
RAD52−ERCC4−ERCC1 complex
Prohibitin−HIRA complex
Polycomb repressive complex 1 (PRC1, hPRC−H)
PCAF complex
p400−associated complex
OGT−HIRA complex
NuRD.1 complex
NuA4/Tip60 HAT complex
NuA4/Tip60−HAT complex B
NuA4/Tip60−HAT complex A
NuA4/Tip60−HAT complex
NRD complex (Nucleosome remodeling and deacetylation complex)
NCOR2 complex
NCOR1 complex
NCOR complex
NCOR−SIN3−RPD3 complex
NCOR−SIN3−HDAC−HESX1 complex
NCOR−HDAC3 complex
MYC−TRRAP−KAT2A complex
MYC−MAX−KAT2A−TRRAP complex
MTA2 complex
MTA1 complex
MTA1−HDAC core complex
mSin3A complex
MiDAC complex
Mi2/NuRD complex
Mi2/NuRD−BCL6−MTA3 complex
Mi−2/NuRD−MTA3 complex
MeCP1 complex
LSD1 complex
LINC core complex
LINC complex, S−phase
LINC complex, quiescent cells
LIN9−BMYB complex
LARC complex (LCR−associated remodeling complex)
KIF23−RACGAP1 complex
KAT2A−TRRAP complex
Kaiso−NCOR complex
INO80 chromatin remodeling complex
ING2 complex
HuCHRAC complex
hNURF complex
Histone H3.3 complex
Histone H3.1 complex
HDAC3−H1.3−SMRT−N−Cor complex
HDAC2−asscociated core complex
HDAC1−associated protein complex
HDAC1−associated core complex cII
HCF−1 complex
GCN5−TRRAP histone acetyltransferase complex
ESR1−CDK7−CCNH−MNAT1−MTA1−HDAC2 complex
ERCC1−ERCC4−MSH2 complex
ECT2−KIF23−RACGAP1 complex
E2F−6 complex
DNTTIP1−ZNF541−HDAC1−HDAC2 complex
DMAP1−associated complex
CtBP core complex
CtBP complex
CoREST−HDAC complex
Chromatin assembly complex (CAF−1 complex)
CEN complex
CDH4−HDAC2−MTA2−RBBP7−TWIST1 complex
BRMS1−SIN3−HDAC complex
BRM−SIN3A complex
BRG1−SIN3A complex
BRCC complex
BRCA1−HDAC1−HDAC2 complex
BRCA1−BARD1−BRCA2−DNA damage complex III
BRAF53−BRCA2 complex
BCOR complex
BASC complex (BRCA1−associated genome surveillance complex)
ATAC complex, YEATS2−linked
ATAC complex, GCN5−linked
ASF1−interacting protein complex
ASF1−histone containing complex
Anti−HDAC2 complex
anti−BHC110 complex
ALL−1 supercomplex
−Log10(FDR)
15
10
5

Fig. S5. CORUM analysis of interactors from Helios^{WT} and Helios^{I325V} BioID. Heatmap showing differences in the overrepresentation of prey proteins in the CORUM database (*45*) with a false discovery rate (FDR) < 0.01.

Figure S6

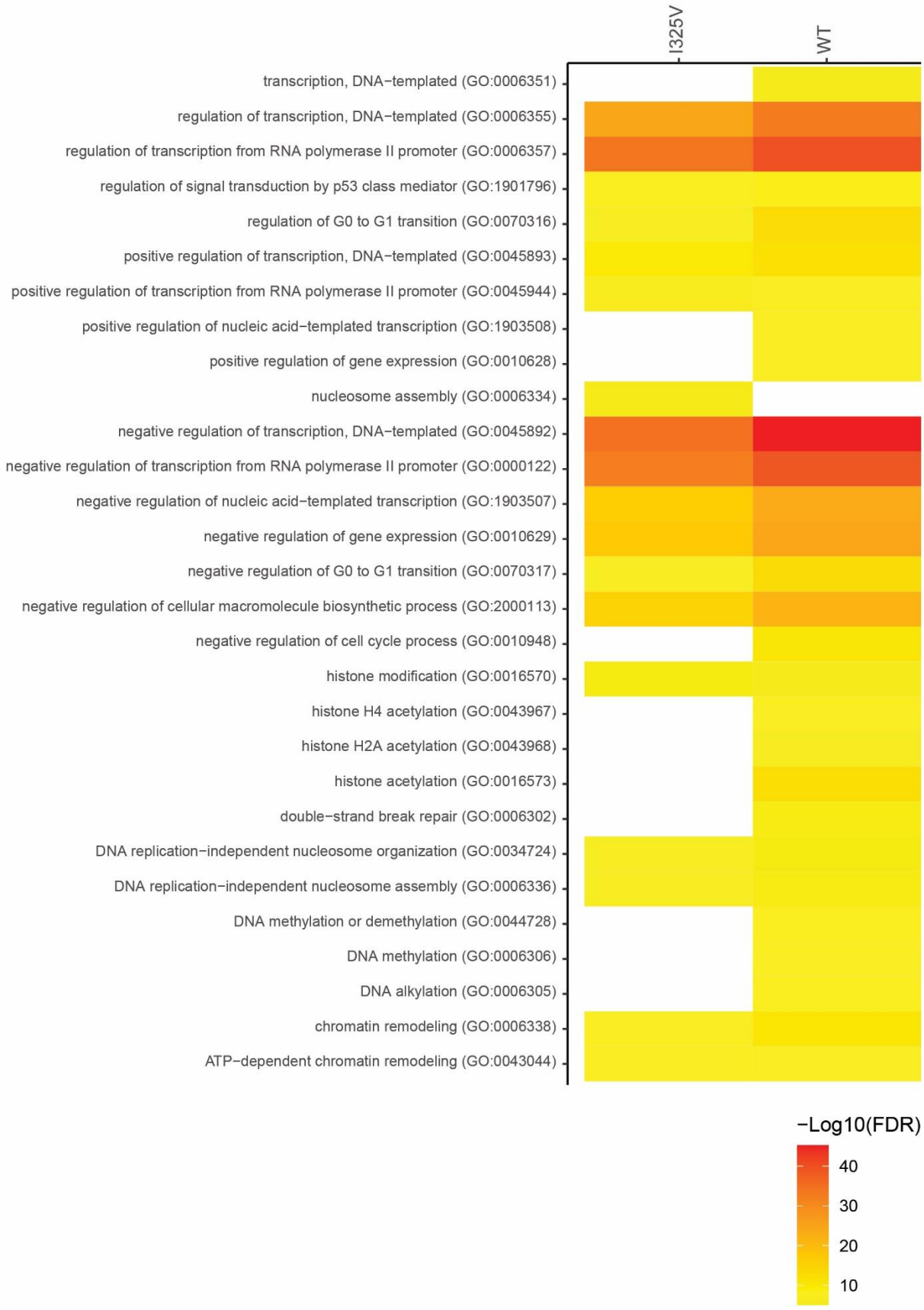
I325V
WT
transcription, DNA−templated (GO:0006351)
regulation of transcription, DNA−templated (GO:0006355)
regulation of transcription from RNA polymerase II promoter (GO:0006357)
regulation of signal transduction by p53 class mediator (GO:1901796)
regulation of G0 to G1 transition (GO:0070316)
positive regulation of transcription, DNA−templated (GO:0045893)
positive regulation of transcription from RNA polymerase II promoter (GO:0045944)
positive regulation of nucleic acid−templated transcription (GO:1903508)
positive regulation of gene expression (GO:0010628)
nucleosome assembly (GO:0006334)
negative regulation of transcription, DNA−templated (GO:0045892)
negative regulation of transcription from RNA polymerase II promoter (GO:0000122)
negative regulation of nucleic acid−templated transcription (GO:1903507)
negative regulation of gene expression (GO:0010629)
negative regulation of G0 to G1 transition (GO:0070317)
negative regulation of cellular macromolecule biosynthetic process (GO:2000113)
negative regulation of cell cycle process (GO:0010948)
histone modification (GO:0016570)
histone H4 acetylation (GO:0043967)
histone H2A acetylation (GO:0043968)
histone acetylation (GO:0016573)
double−strand break repair (GO:0006302)
DNA replication−independent nucleosome organization (GO:0034724)
DNA replication−independent nucleosome assembly (GO:0006336)
DNA methylation or demethylation (GO:0044728)
DNA methylation (GO:0006306)
DNA alkylation (GO:0006305)
chromatin remodeling (GO:0006338)
ATP−dependent chromatin remodeling (GO:0043044)
−Log10(FDR)
40
30
20
10

Fig. S6. Gene ontology analysis of interactors from Helios^{WT} and Helios^{I325V} BioID. Heatmap showing differences in the overrepresentation of GO terms related to biological processes with a false discovery rate (FDR) < 10^{-5}.

Figure S7

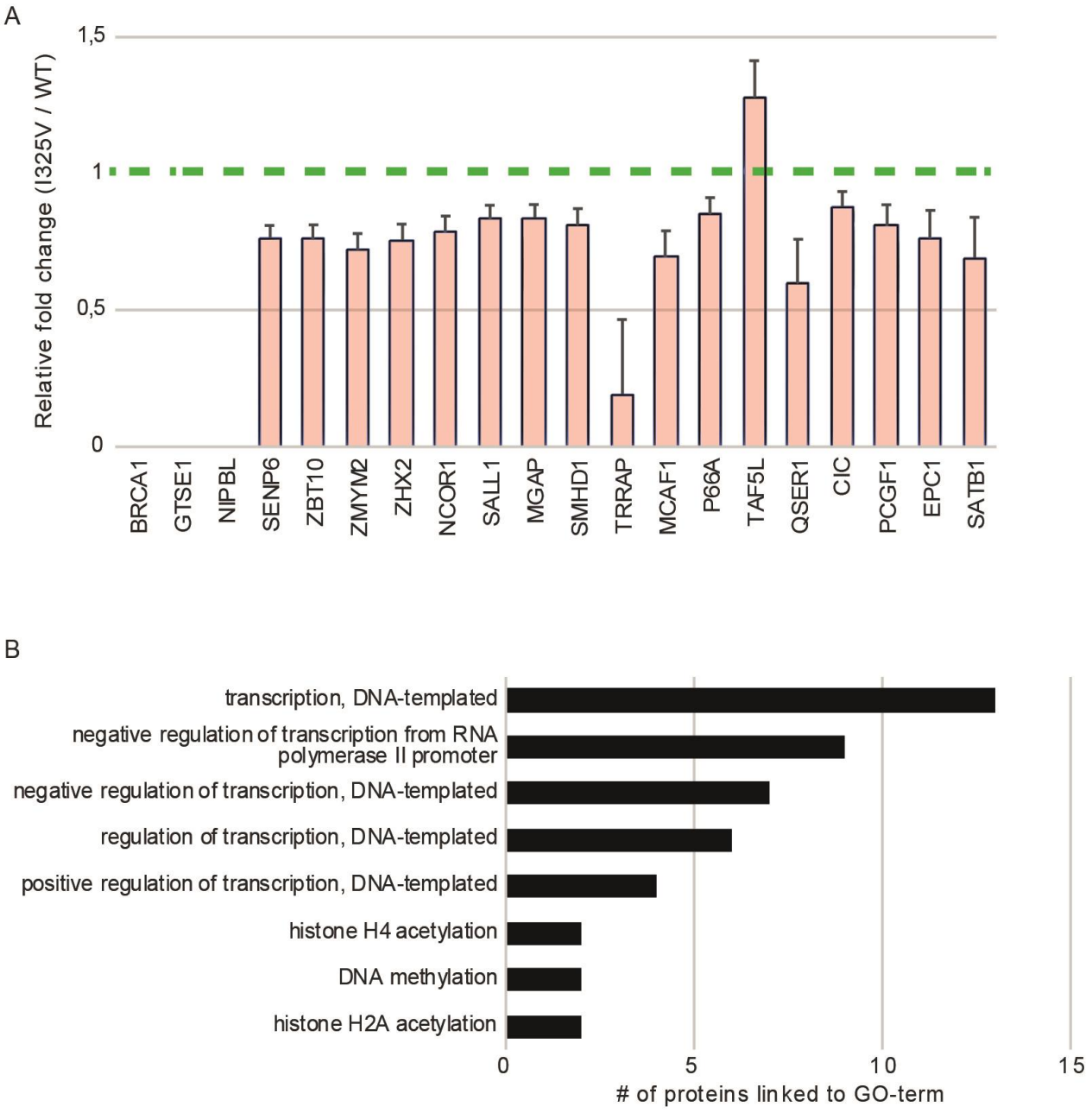
A
Relative fold change (I325V / WT)
1,5
1
0,5
0
BRCA1
GTSE1
NIPBL
SENP6
ZBT10
ZMYM2
ZHX2
NCOR1
SALL1
MGAP
SMHD1
TRRAP
MCAF1
P66A
TAF5L
QSER1
CIC
PCGF1
EPC1
SATB1
B
transcription, DNA-templated
negative regulation of transcription from RNA polymerase II promoter
negative regulation of transcription, DNA-templated
regulation of transcription, DNA-templated
positive regulation of transcription, DNA-templated
histone H4 acetylation
DNA methylation
histone H2A acetylation
0
5
10
15
# of proteins linked to GO-term

Fig. S7. MaxQuant quantification analysis of interactors. (A) Bar chart with significantly altered interactors, showing the fold change relative to the Helios^{WT}, after performing MaxQuant analysis and normalizing the label-free quantification (LFQ) intensities of the Helios^{I325V} interactors to that of Helios^{WT}. Data is representative of triplicates and a Student's *t*-test was performed, p-value < 0.05. **(B)** Gene ontology (GO) analysis for biological processes of the significantly altered proteins from (A), with bars indicating the number of proteins associated with each GO term.

Figure S8

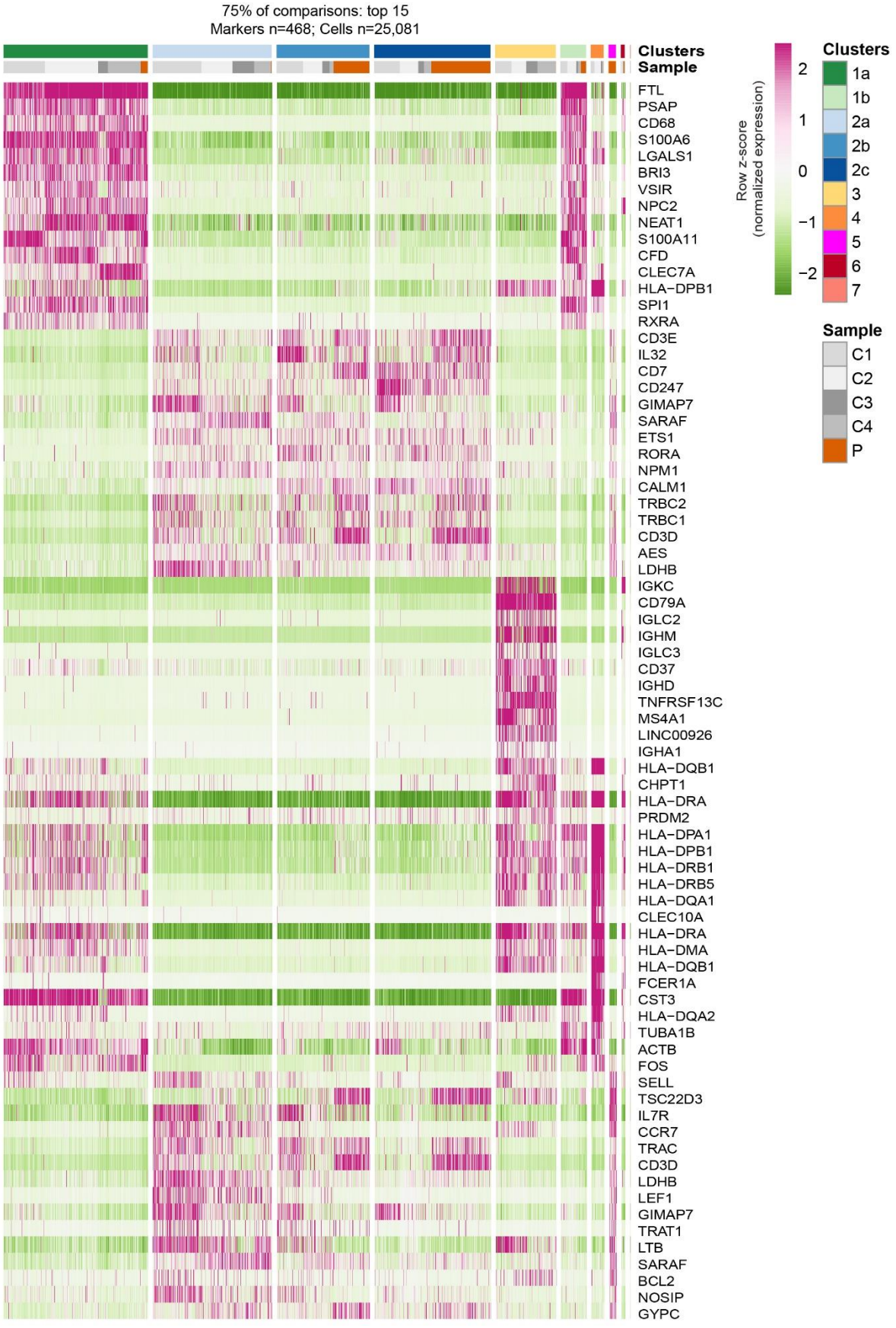
75% of comparisons: top 15
Markers n=468; Cells n=25,081
Clusters
Sample
FTL
PSAP
CD68
S100A6
LGALS1
BRI3
VSIR
NPC2
NEAT1
S100A11
CFD
CLEC7A
HLA−DPB1
SPI1
RXRA
CD3E
IL32
CD7
CD247
GIMAP7
SARAF
ETS1
RORA
NPM1
CALM1
TRBC2
TRBC1
CD3D
AES
LDHB
IGKC
CD79A
IGLC2
IGHM
IGLC3
CD37
IGHD
TNFRSF13C
MS4A1
LINC00926
IGHA1
HLA−DQB1
CHPT1
HLA−DRA
PRDM2
HLA−DPA1
HLA−DPB1
HLA−DRB1
HLA−DRB5
HLA−DQA1
CLEC10A
HLA−DRA
HLA−DMA
HLA−DQB1
FCER1A
CST3
HLA−DQA2
TUBA1B
ACTB
FOS
SELL
TSC22D3
IL7R
CCR7
TRAC
CD3D
LDHB
LEF1
GIMAP7
TRAT1
LTB
SARAF
BCL2
NOSIP
GYPC
Row z-score
(normalized expression)
2
1
0
−1
−2
Clusters
1a
1b
2a
2b
2c
3
4
5
6
7
Sample
C1
C2
C3
C4
P

Fig. S8. Meta-clustering of PMBC population. Hierarchical clustering showing the most highly expressed genes per meta-cluster. **(A)** Heatmap showing the top 15 overexpressed genes per meta-clusters (1, 2, 3, 4 and 5). Selected genes are labelled. **(B)** Bar graph showing the relative distribution of cells from each sample across clusters. A complete loss of patient cells from cluster 3 (B cells) is evident, as well as a shift within clusters 1 and 2/5. **(C)** Principle component analysis of the cells from clusters 2 and 5. The close overlap between cells from 5 (patient-only) and 2a (controls-only) indicate high similarity between these cell types.

Figure S9

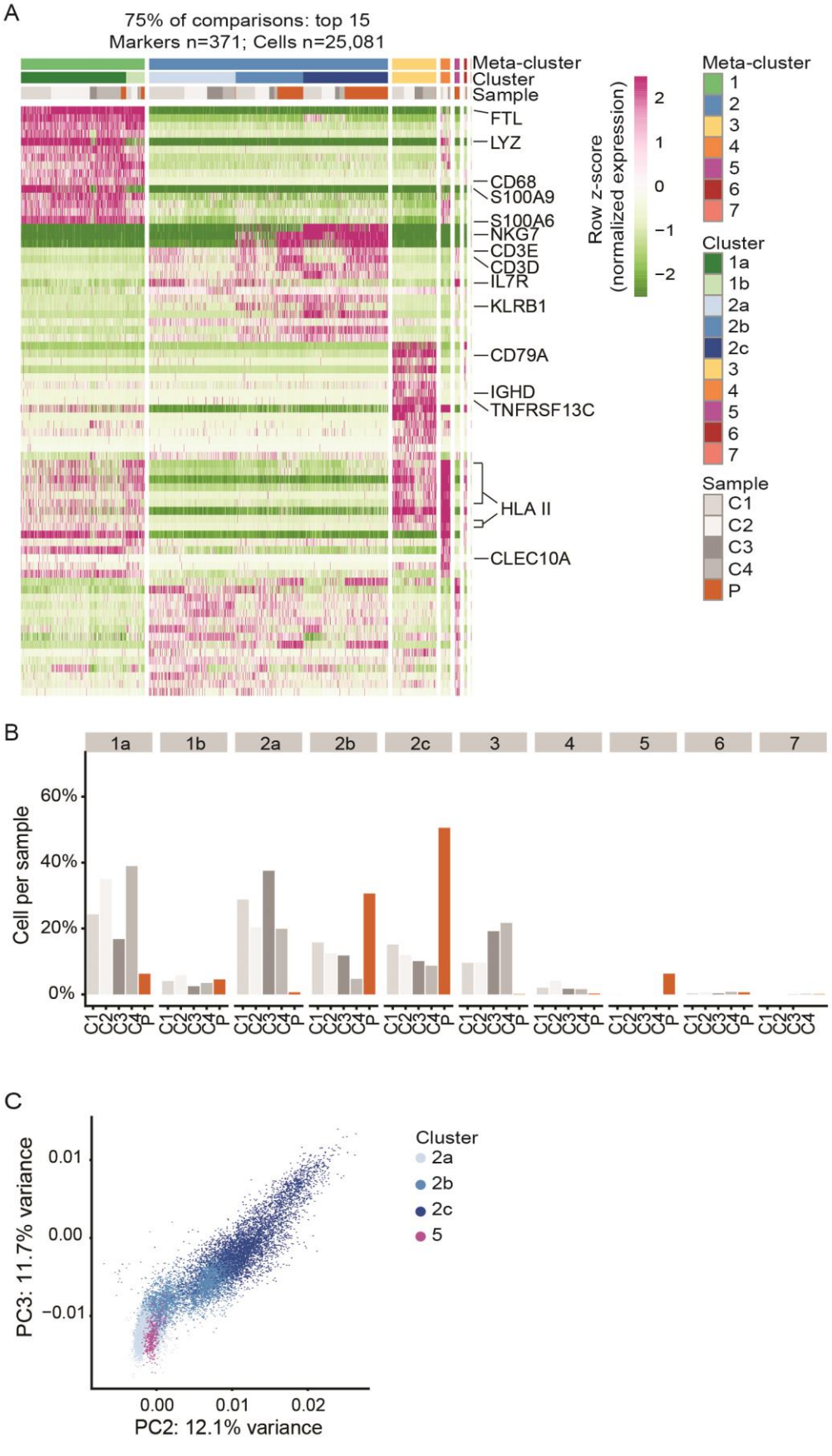
A
75% of comparisons: top 15
Markers n=371; Cells n=25,081
Meta-cluster
Cluster
Sample
FTL
LYZ
CD68
S100A9
S100A6
NKG7
CD3E
CD3D
IL7R
KLRB1
CD79A
IGHD
TNFRSF13C
HLA II
CLEC10A
Row z-score (normalized expression)
2
1
0
−1
−2
Meta-cluster
1
2
3
4
5
6
7
Cluster
1a
1b
2a
2b
2c
3
4
5
6
7
Sample
C1
C2
C3
C4
P
B
1a
1b
2a
2b
2c
3
4
5
6
7
Cell per sample
60%
40%
20%
0%
C1 C2 C3 C4 P
C
PC3: 11.7% variance
0.01
0.00
−0.01
0.00
0.01
0.02
PC2: 12.1% variance
Cluster
2a
2b
2c
5

Fig. S9. Meta-clustering of PMBC subpopulation. Hierarchical clustering showing the most highly expressed genes in each cluster, from cells of all individuals (patient and controls).

Figure S10

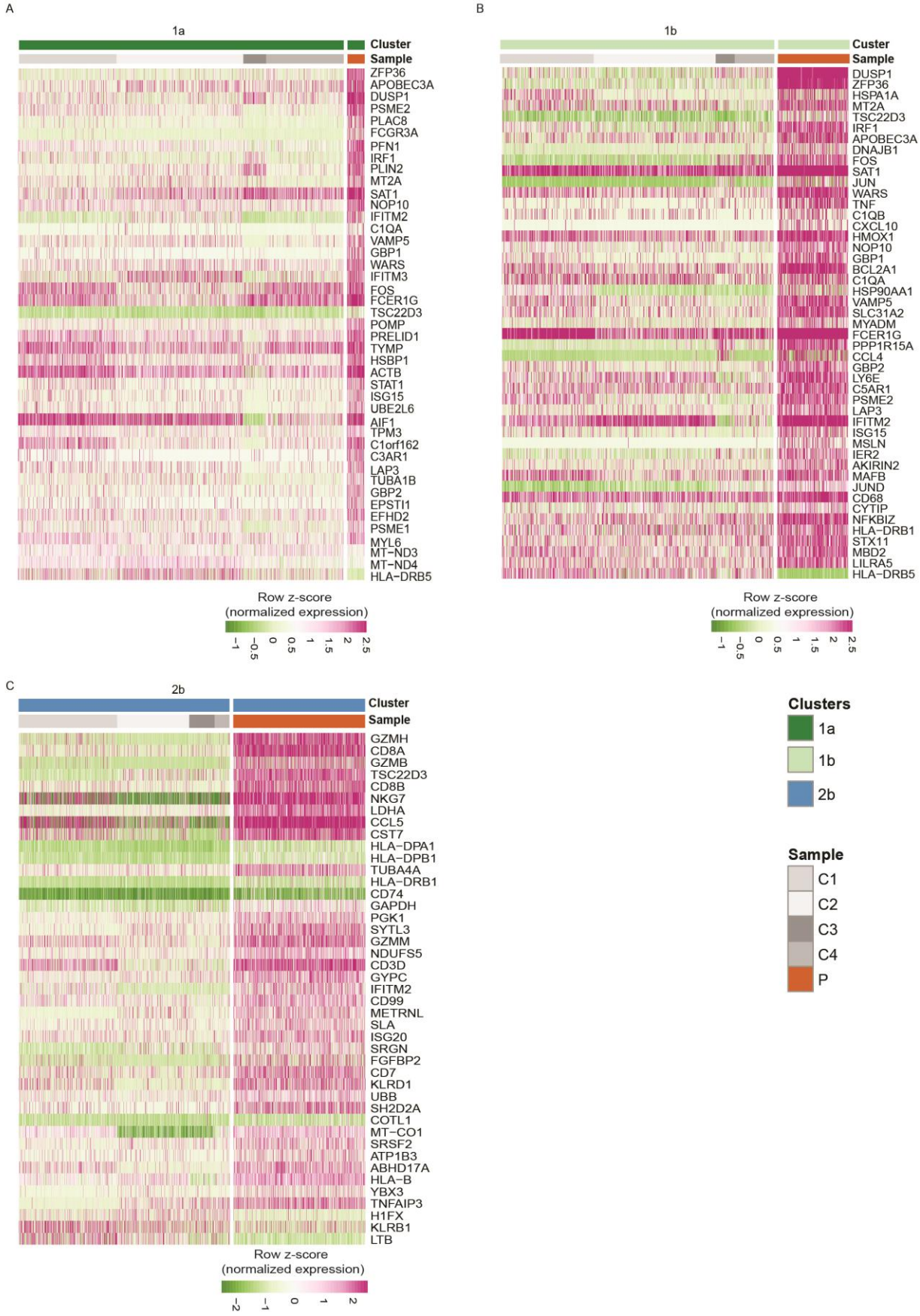
A
1a
Cluster
Sample
ZFP36
APOBEC3A
DUSP1
PSME2
PLAC8
FCGR3A
PFN1
IRF1
PLIN2
MT2A
SAT1
NOP10
IFITM2
C1QA
VAMP5
GBP1
WARS
IFITM3
FOS
FCER1G
TSC22D3
POMP
PRELID1
TYMP
HSBP1
ACTB
STAT1
ISG15
UBE2L6
AIF1
TPM3
C1orf162
C3AR1
LAP3
TUBA1B
GBP2
EPSTI1
EFHD2
PSME1
MYL6
MT-ND3
MT-ND4
HLA-DRB5
Row z-score
(normalized expression)
−1
−0.5
0
0.5
1
1.5
2
2.5
B
1b
Custer
Sample
DUSP1
ZFP36
HSPA1A
MT2A
TSC22D3
IRF1
APOBEC3A
DNAJB1
FOS
SAT1
JUN
WARS
TNF
C1QB
CXCL10
HMOX1
NOP10
GBP1
BCL2A1
C1QA
HSP90AA1
VAMP5
SLC31A2
MYADM
FCER1G
PPP1R15A
CCL4
GBP2
LY6E
C5AR1
PSME2
LAP3
IFITM2
ISG15
MSLN
IER2
AKIRIN2
MAFB
JUND
CD68
CYTIP
NFKBIZ
HLA-DRB1
STX11
MBD2
LILRA5
HLA-DRB5
Row z-score
(normalized expression)
−1
−0.5
0
0.5
1
1.5
2
2.5
C
2b
Cluster
Sample
GZMH
CD8A
GZMB
TSC22D3
CD8B
NKG7
LDHA
CCL5
CST7
HLA-DPA1
HLA-DPB1
TUBA4A
HLA-DRB1
CD74
GAPDH
PGK1
SYTL3
GZMM
NDUFS5
CD3D
GYPC
IFITM2
CD99
METRNL
SLA
ISG20
SRGN
FGFBP2
CD7
KLRD1
UBB
SH2D2A
COTL1
MT-CO1
SRSF2
ATP1B3
ABHD17A
HLA-B
YBX3
TNFAIP3
H1FX
KLRB1
LTB
Row z-score
(normalized expression)
−2
−1
0
1
2
Clusters
1a
1b
2b
Sample
C1
C2
C3
C4
P

Fig. S10. DGE within clusters. Heatmaps showing results of a differential gene expression analysis done between patient cells within each of cluster 1a **(A)**, 1b **(B)** and 2b **(C)** compared to all 4 controls.

Figure S11

A

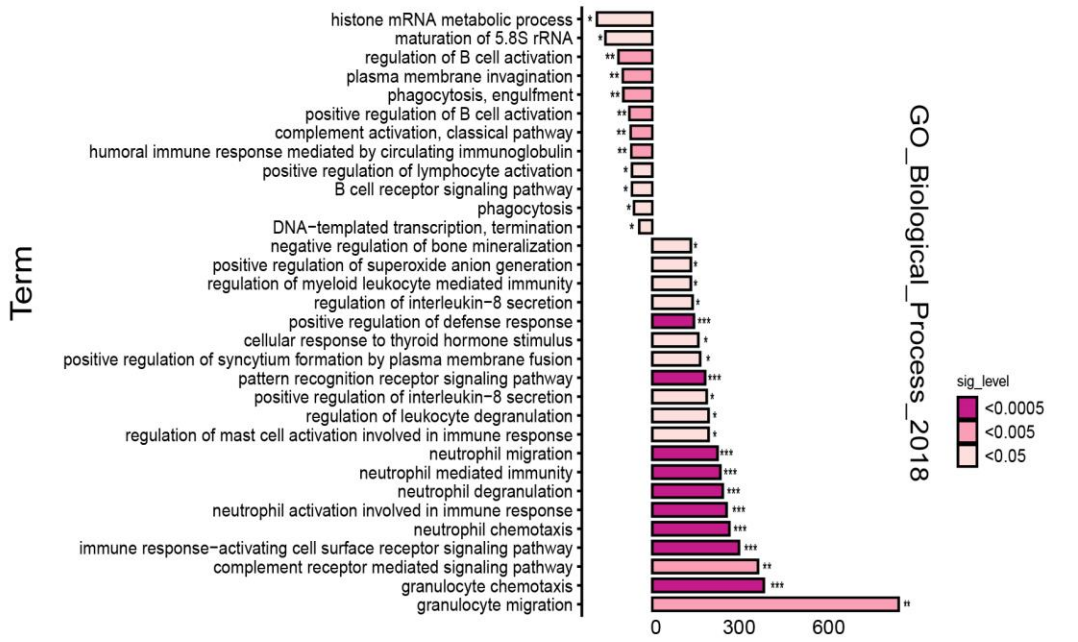

B

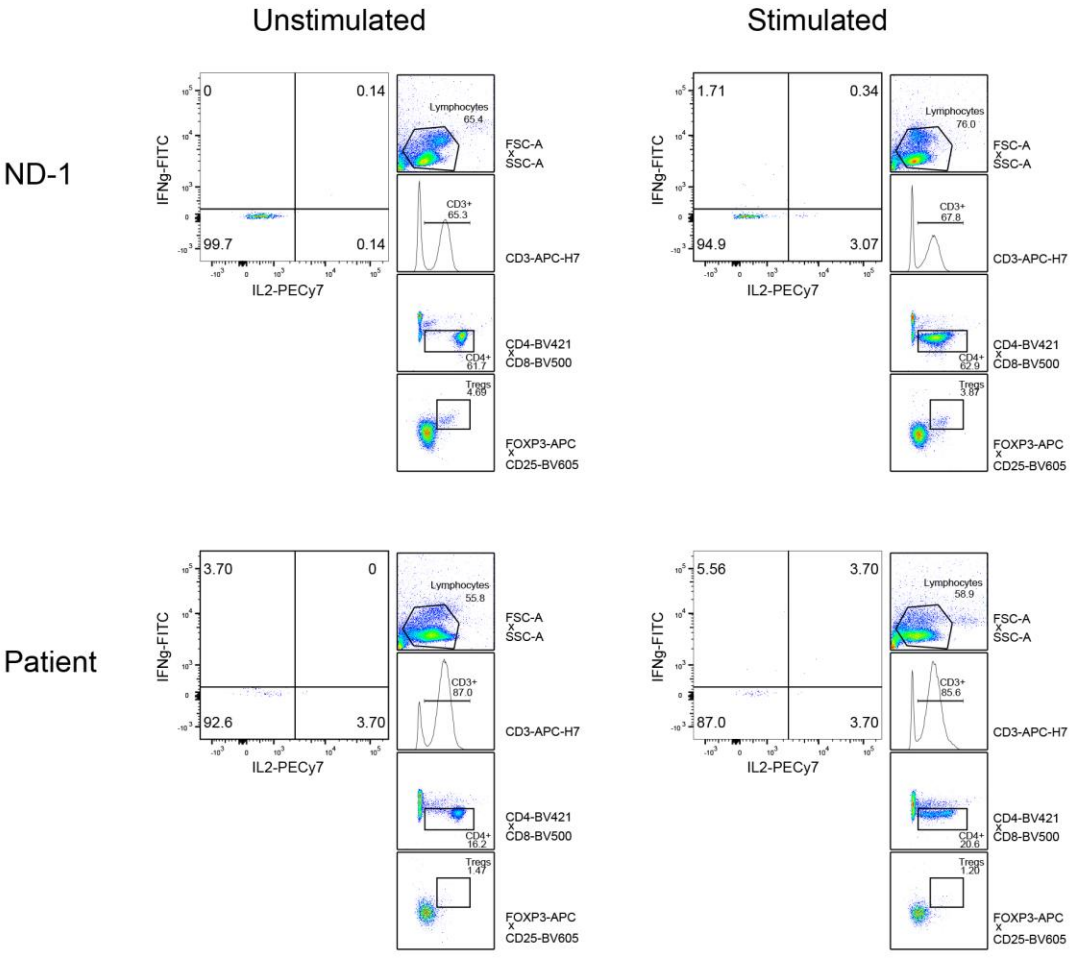

Fig. S11. Analysis of naïve B cells and Tregs of patient. **(A)** Bar charts indicating enriched Gene Ontology Biological Processes terms associated with differentially expressed genes in patient-derived naïve B cells / T_{regs} compared to healthy controls. Terms linked to downregulated genes are shown on the top left and terms linked to upregulated genes on the bottom right. **(B)** Flow cytometry plots, showing gating strategy for measuring intracellular IL-2 and IFNγ cytokine production in Treg cells gated on $CD25^{+}FOXP3^{+}$ $CD4^{+}$ T cells after stimulation of PBMCs with PMA and Ionomycin for 5 hours and at the basal unstimulated state. These plots correspond to the summary graph shown in fig. 5G. Positive cytokine gates were set using the unstimulated cytokine-stained cells as negative controls, whereby the same cytokine gate was used across all samples per experiment.

Figure S12

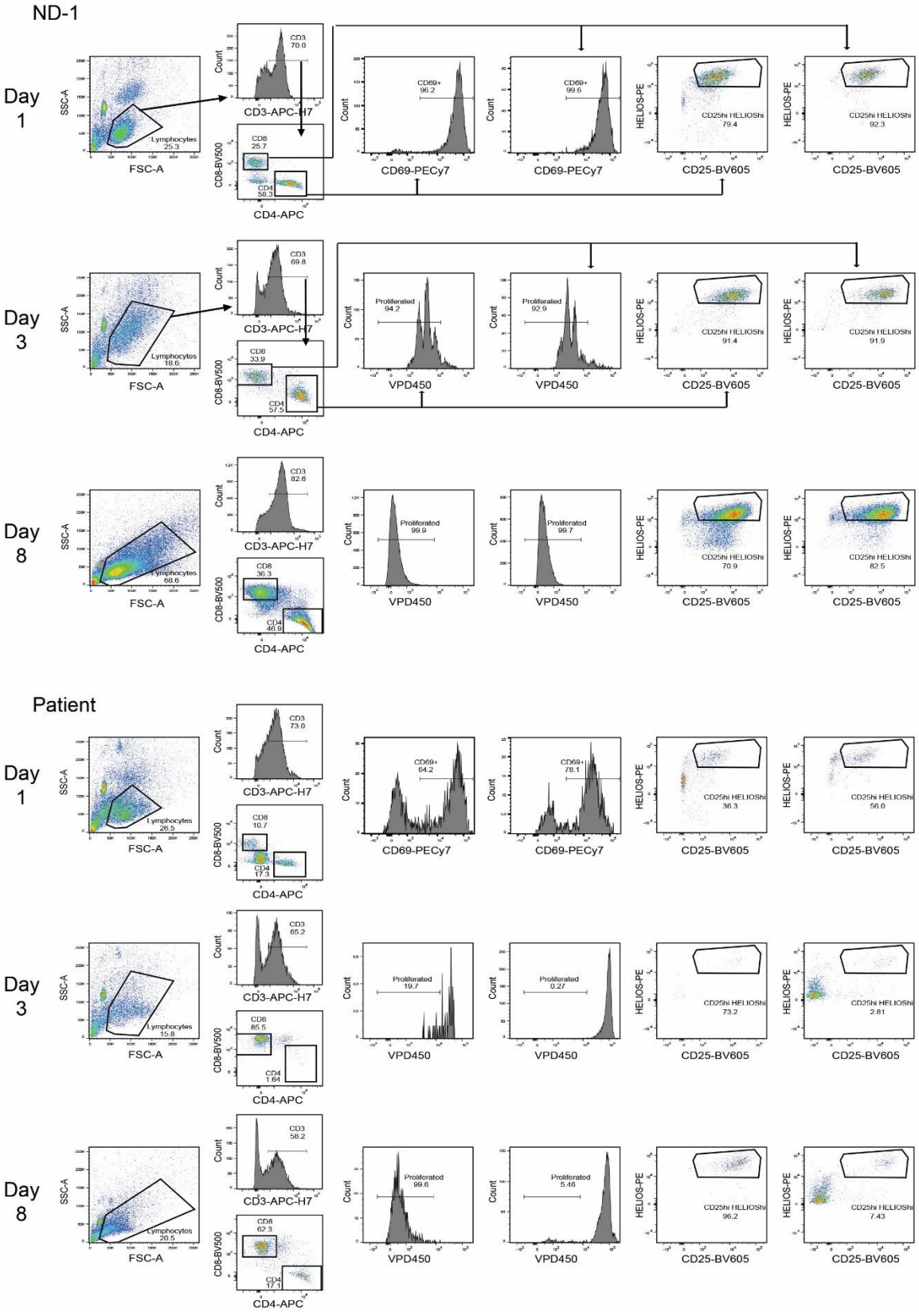
ND-1
Day 1
Day 3
Day 8
Patient
Day 1
Day 3
Day 8
SSC-A
FSC-A
Lymphocytes
CD3
CD3-APC-H7
CD8-BV500
CD4-APC
CD8
CD4
CD69+
CD69-PECy7
Proliferated
VPD450
HELIOS-PE
CD25-BV605
CD25hi HELIOShi

Fig. S12. Gating strategy for T cell proliferation assay. Flow cytometry plots showing gating of $CD4^+$ and $CD8^+$ T cells from within the $CD3^+$ lymphocyte gate, after stimulation with CD3/CD28 beads, at day 1, day 3 and day 8. At day 1, CD69 activation marker, CD25 and intracellular Helios expression were measured. At days 3 and 8, CD25, Helios and the dilution of VPD450 were measured as T cells proliferated. These plots correspond to data shown in fig. 6A-C.

Figure S13

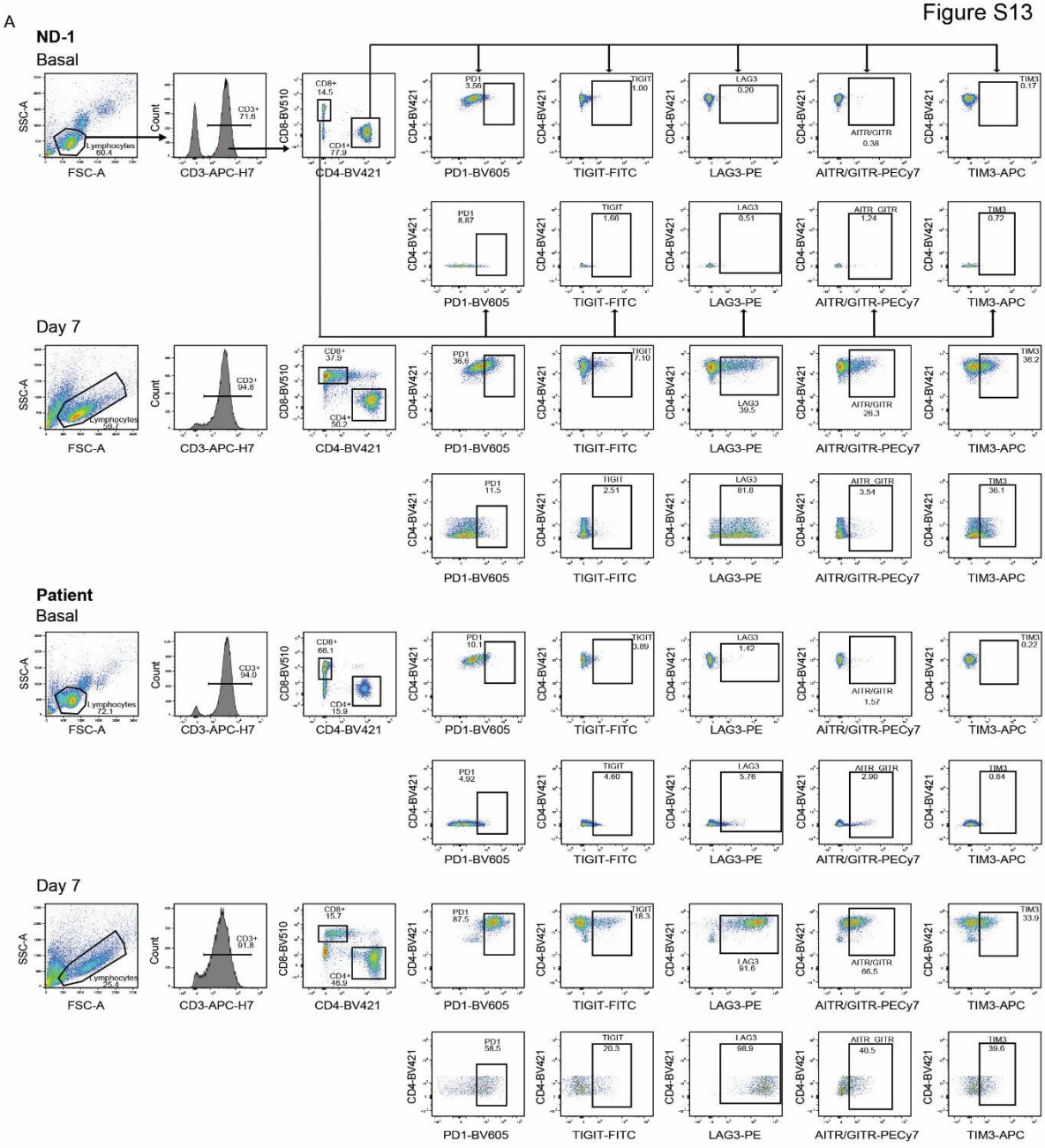
A
ND-1
Basal
Day 7
Patient
Basal
Day 7
SSC-A
FSC-A
Lymphocytes
Count
CD3-APC-H7
CD3+
CD8-BV510
CD8+
CD4+
CD4-BV421
PD1-BV605
TIGIT-FITC
LAG3-PE
AITR/GITR-PECy7
TIM3-APC
PD1
TIGIT
LAG3
AITR/GITR
TIM3

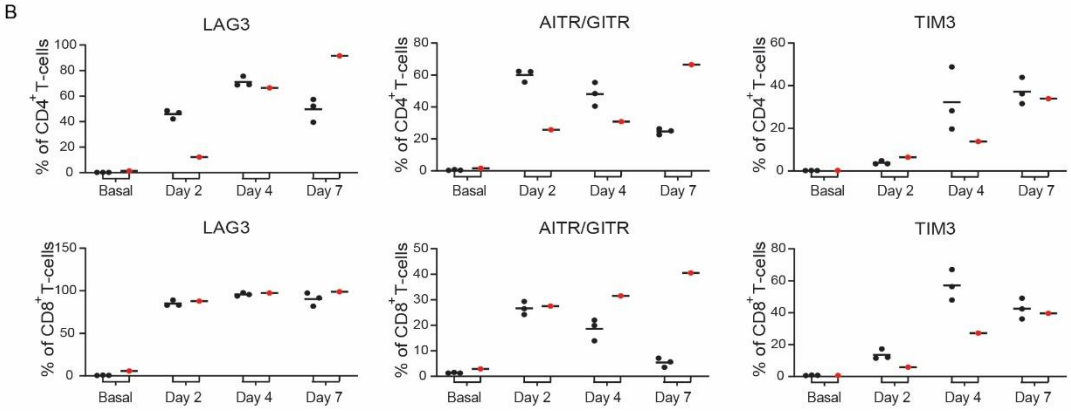
B
LAG3
AITR/GITR
TIM3
% of CD4+ T-cells
% of CD8+ T-cells
Basal
Day 2
Day 4
Day 7

Fig. S13. Expression of exhaustion markers and check-point inhibitors upon TCR stimulation. (**A**) Gating strategy showing the expression of PD-1, TIGIT, LAG3, AITR/GITR and TIM3 in $CD4^+$ and $CD8^+$ $CD3^+$ T cells at two time-point, basal (unstimulated) level and at day 7 post-stimulation with CD3/CD28 beads. This corresponds to some summary graphs shown in fig. 6D. **(B)** Summary graphs showing the expression of LAG3, AITR/GITR and TIM3 at all four time-points, basal level, day 2, day 4 and day 7, in $CD4^+$ and $CD8^+$ T cells.

Figure S14

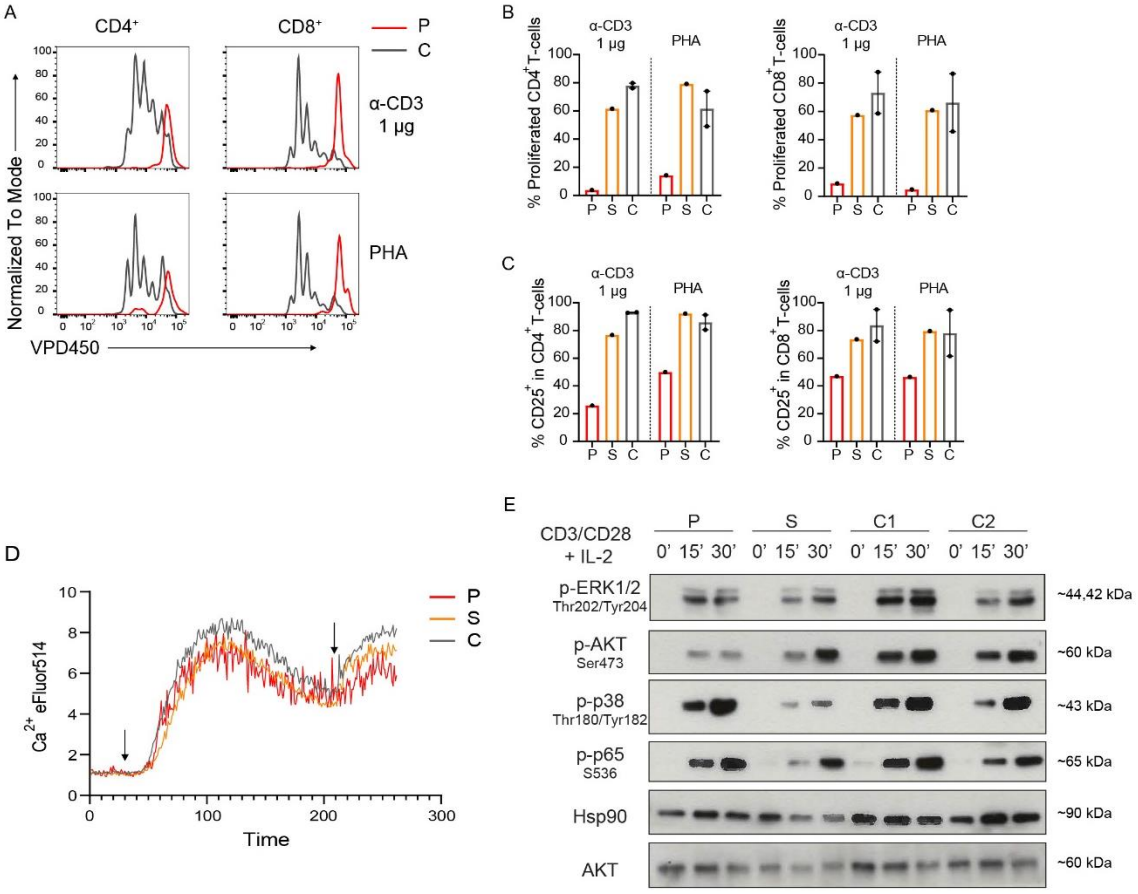
A
CD4+
CD8+
P
C
α-CD3
1 µg
PHA
Normalized To Mode
VPD450
B
α-CD3
1 µg
PHA
% Proliferated CD4+ T-cells
% Proliferated CD8+ T-cells
P S C
C
% CD25+ in CD4+ T-cells
% CD25+ in CD8+ T-cells
D
Ca2+ eFluor514
Time
S
E
CD3/CD28
+ IL-2
P
S
C1
C2
0' 15' 30'
p-ERK1/2
Thr202/Tyr204
~44,42 kDa
p-AKT
Ser473
~60 kDa
p-p38
Thr180/Tyr182
~43 kDa
p-p65
S536
~65 kDa
Hsp90
~90 kDa
AKT
~60 kDa

Fig. S14. Patient T cells have defective proliferation with no upstream signaling defects. (A) Representative histograms displaying the dilution of the violet proliferation dye (VPD450) in $CD4^+$ and $CD8^+$ T cells from the patient and a control after 3 days of stimulation with anti-CD3 (OKT3; 1 μg) or PHA (1 μg); P: patient, C: control. **(B)** Summary bar graphs showing the percentage of proliferated $CD4^+$ and $CD8^+$ T cells at day 3, under the different stimuli, in the patient (P; red), sister (S; orange) and controls (C; black, n = 2). **(C)** Summary bar graphs showing percentage of $CD4^+$ and $CD8^+$ T cells that have upregulated CD25 (IL2RA) at day 3, corresponding to the proliferation experiments from (B). **(D)** Graph showing intracellular calcium release in T-lymphoblasts, through the measurement of a calcium-binding dye, upon TCR cross-linking. IgM was added to CD3-stimulated T-lymphoblasts 30 seconds after acquisition of basal calcium levels (first arrow), followed by addition of Ionomycin (1 μg) 3 minutes later (second arrow). Data from the patient (P) and sister (S) are an average of two independent experiments. Data from the controls (C) is representative of three individuals, two of which the experiment has been done on twice independently. Multiple t-test analysis was done to compare data from every second across the three groups; no significant difference was observed at any time-point. **(E)** Western blot of starved T-lymphocytes after stimulation with CD3/CD28 beads and IL-2 for 15 and 30 minutes, or left unstimulated (0 minutes). Lysates were run and blotted for p-ERK, p-p65, p-p38, p-AKT, total AKT and Hsp90 (housekeeping gene).

Figure S15

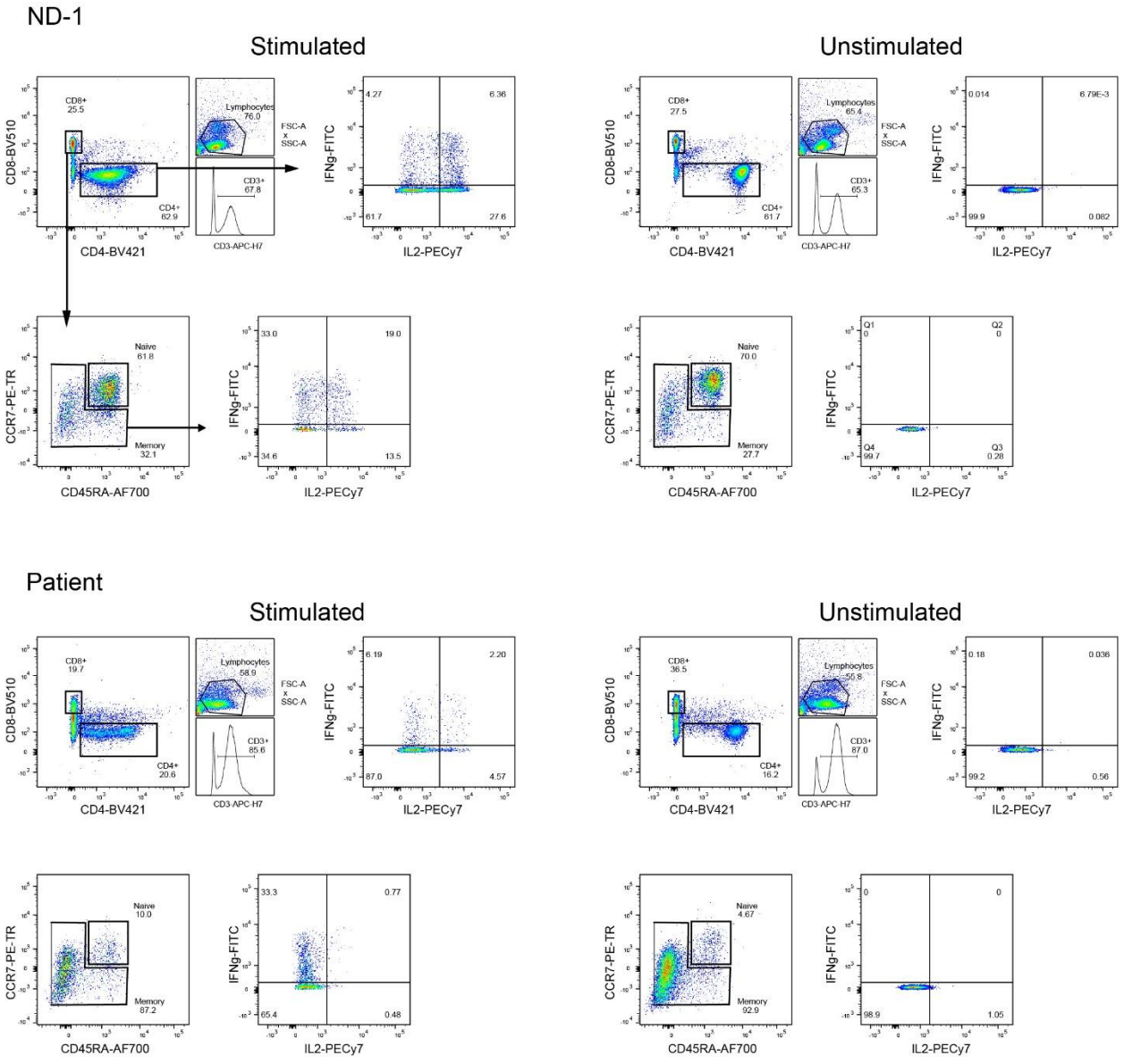
ND-1
Stimulated
Unstimulated
Patient
Stimulated
Unstimulated
CD8-BV510
CD4-BV421
Lymphocytes
FSC-A x SSC-A
CD3-APC-H7
IFNg-FITC
IL2-PECy7
CCR7-PE-TR
CD45RA-AF700
Naive
Memory

Fig. S15. Intracellular IL-2 secretion assay gating strategy. Flow cytometry plots showing percentage of cells positive for IL-2 and IFNγ gated on $CD4^+$ or memory $CD8^+$ $CD3^+$ T lymphocytes of a normal donor and patient after stimulation of PBMCs with PMA and Ionomycin for 5 hours. Gating corresponds to summary plots in fig. 6E. Positive cytokine gates were set using the unstimulated cytokine-stained cells as negative controls, whereby the same cytokine gate was used across all samples per experiment.

Figure S16

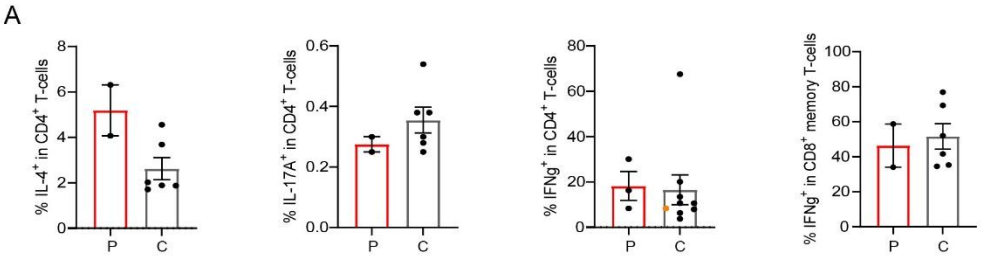
A
% IL-4+ in CD4+ T-cells
% IL-17A+ in CD4+ T-cells
% IFNg+ in CD4+ T-cells
% IFNg+ in CD8+ memory T-cells
P
C

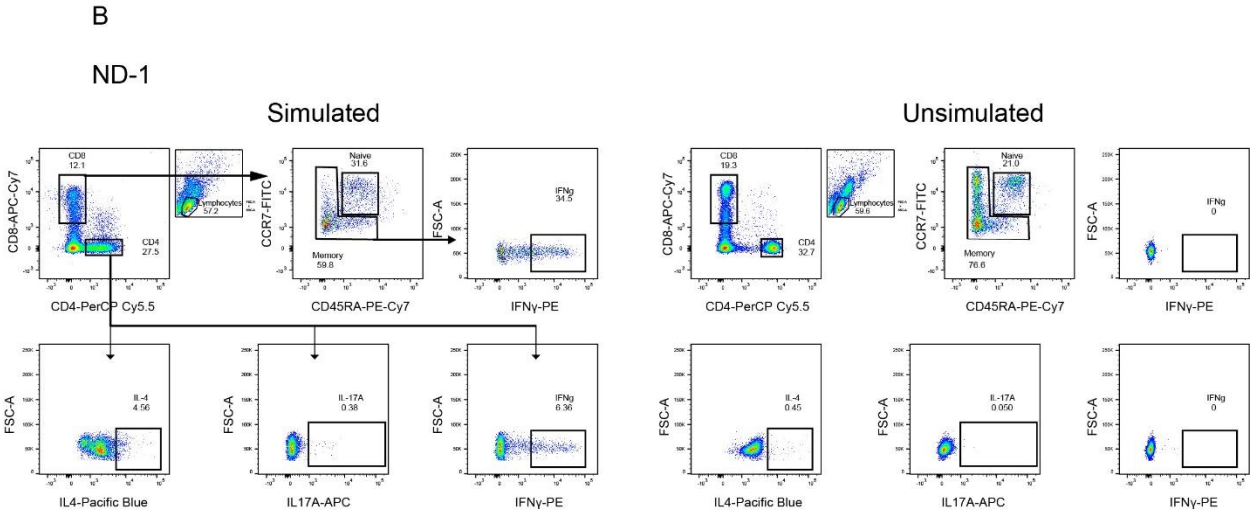
B
ND-1
Simulated
Unsimulated
CD8-APC-Cy7
CD4-PerCP Cy5.5
CCR7-FITC
CD45RA-PE-Cy7
FSC-A
IFNγ-PE
IL4-Pacific Blue
IL17A-APC
Lymphocytes
Naive
Memory
CD8
CD4
IL-4
IL-17A
IFNg

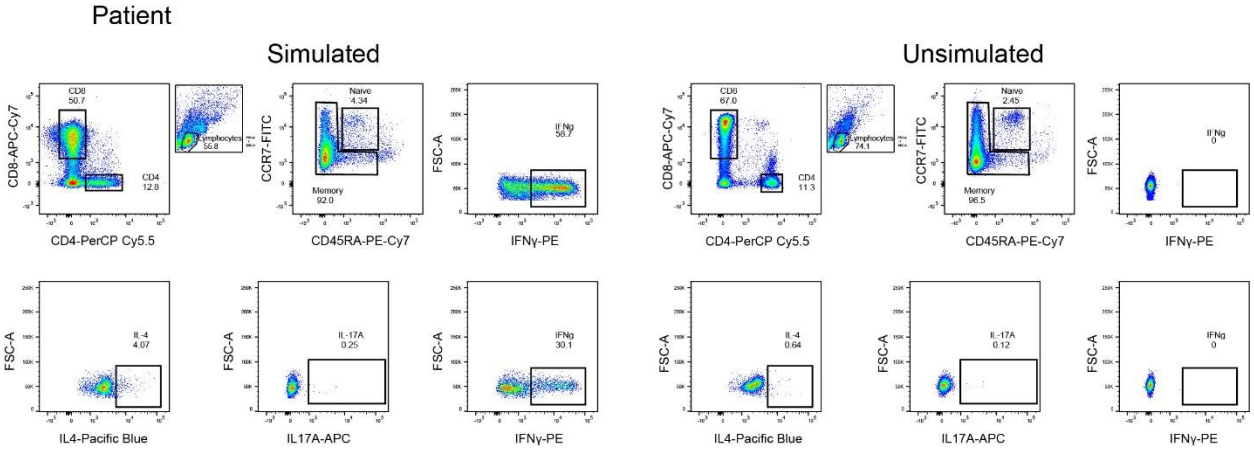
Patient
Simulated
Unsimulated
CD8-APC-Cy7
CD4-PerCP Cy5.5
CCR7-FITC
CD45RA-PE-Cy7
FSC-A
IFNγ-PE
IL4-Pacific Blue
IL17A-APC
Lymphocytes
Naive
Memory
CD8
CD4
IL-4
IL-17A
IFNg

Fig. S16. Intracellular cytokine secretion assay gating strategy. (A) Bar graphs showing the percentage of total $CD4^+$ that produced IL-4, IL-17A and IFNγ and memory $CD8^+$ T cells that produced IFNγ after stimulation of PBMCs with PMA/ionomycin for 5 hours. **(B)** Flow cytometry plots showing percentage of cells positive for the indicated cytokines, gated on $CD4^+$ or memory $CD8^+$ $CD3^+$ T lymphocytes of a normal donor and patient after stimulation of PBMCs with PMA and Ionomycin for 5 hours. Gating corresponds to summary plots in fig. S16A above. Positive cytokine gates were set using the unstimulated cytokine-stained cells as negative controls, whereby the same cytokine gate was used across all samples per experiment.

Figure S17

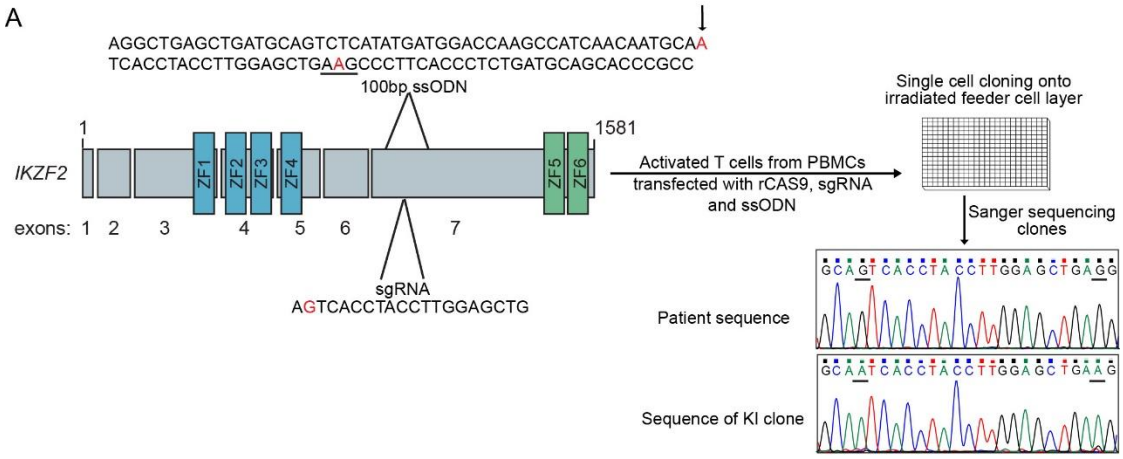
A
AGGCTGAGCTGATGCAGTCTCATATGATGGACCAAGCCATCAACAATGCAA
TCACCTACCTTGGAGCTGAAGCCCTTCACCCTCTGATGCAGCACCCGCC
100bp ssODN
IKZF2
1
1581
ZF1
ZF2
ZF3
ZF4
ZF5
ZF6
exons: 1 2 3 4 5 6 7
sgRNA
AGTCACCTACCTTGGAGCTG
Activated T cells from PBMCs
transfected with rCAS9, sgRNA
and ssODN
Single cell cloning onto
irradiated feeder cell layer
Sanger sequencing
clones
Patient sequence
Sequence of KI clone

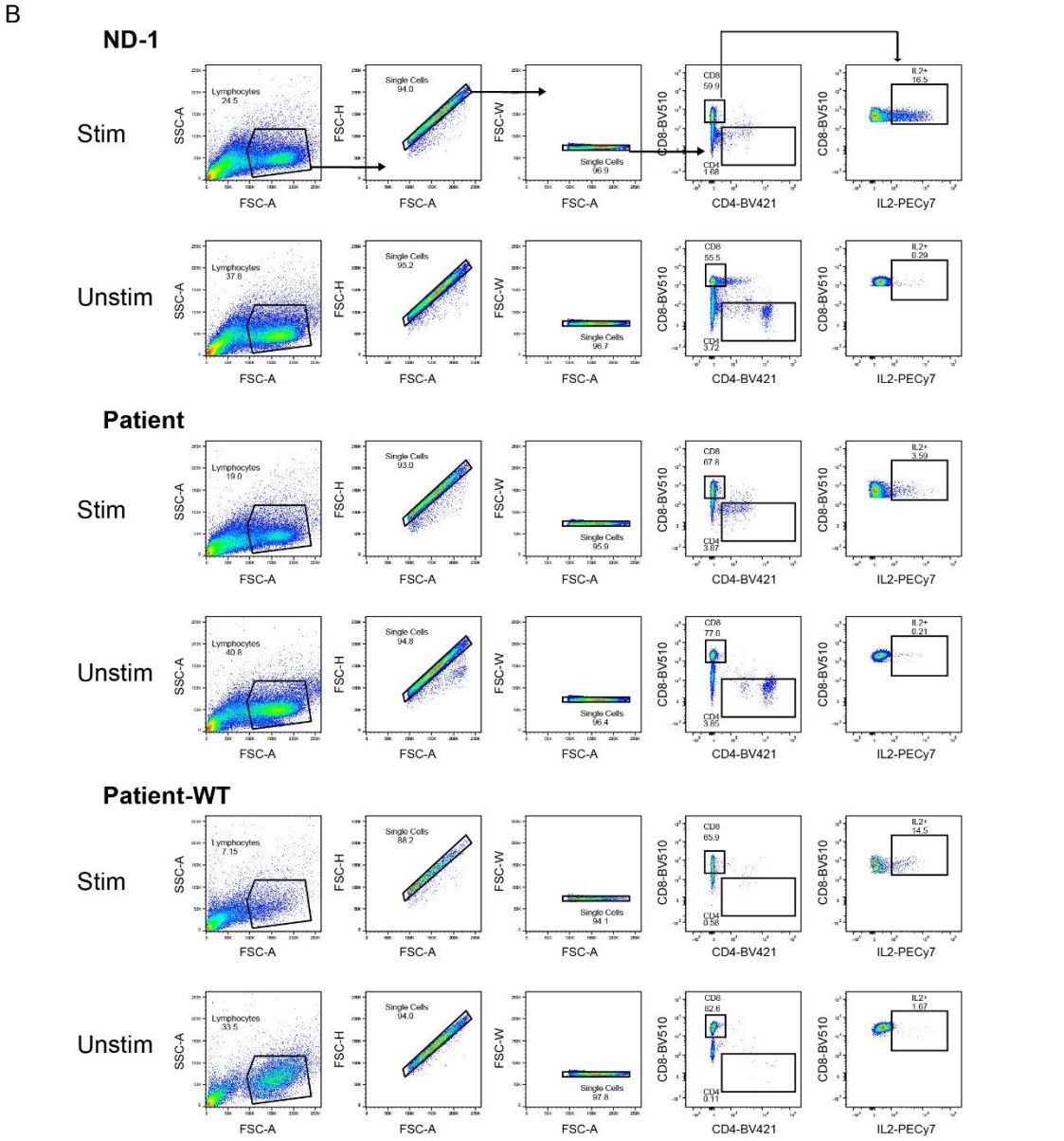
B
ND-1
Stim
Unstim
Patient
Stim
Unstim
Patient-WT
Stim
Unstim
SSC-A
FSC-A
FSC-H
FSC-W
CD8-BV510
CD4-BV421
IL2-PECy7
Lymphocytes
Single Cells
CD8
CD4
IL2+

Fig. S17. Generation of CRISPR-Cas9 edited patient T-lymphoblasts with WT *IKZF2* and rescue of IL-2 production defect. (A) Scheme showing the approach to the generation and screening of a patient-derived T-lymphoblast clone with wildtype *IKZF2* and the chromatogram of the successful clone with the corrected wildtype variant and the silent PAM mutation. **(B)** Flow cytometry plots showing the gating strategy used to calculate the percentage of cells expressing IL-2 after stimulating T-lymphoblasts from the patient, normal donors and patient-wildtype (P-WT) clone with PMA and Ionomycin for 20 hours (or in the unstimulated state). This gating strategy corresponds to the summary graph shown in fig. 6G. Positive IL-2 gates were set using the unstimulated cytokine-stained cells as negative controls, whereby the same cytokine gate was used across all samples per experiment.

Figure S18

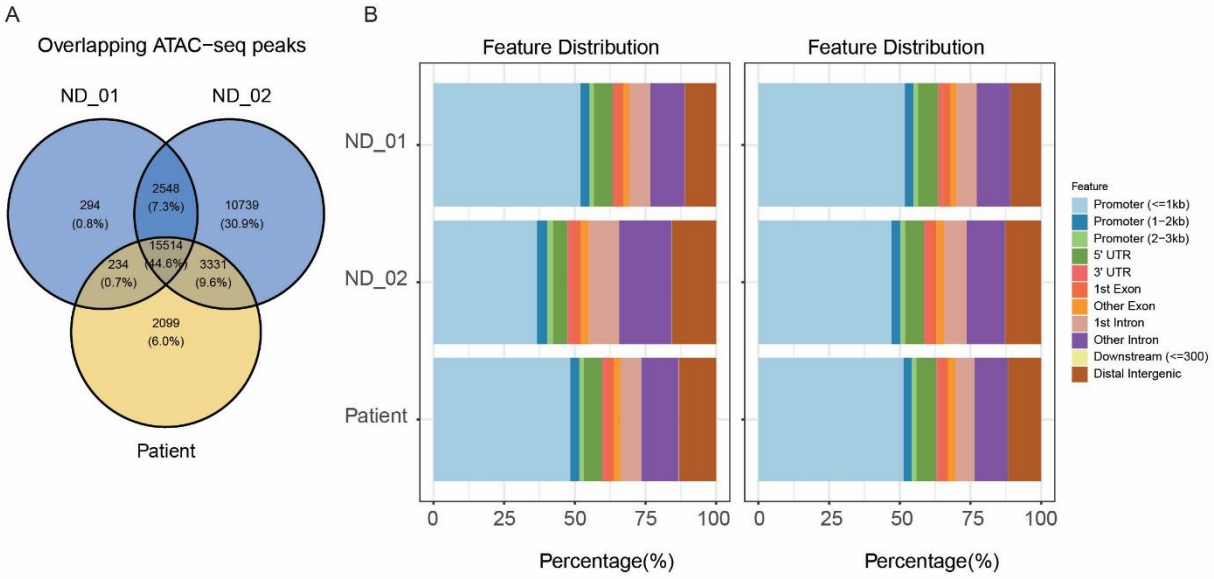
A
Overlapping ATAC−seq peaks
ND_01
ND_02
Patient
294
(0.8%)
2548
(7.3%)
10739
(30.9%)
15514
(44.6%)
234
(0.7%)
3331
(9.6%)
2099
(6.0%)
B
Feature Distribution
Feature Distribution
ND_01
ND_02
Patient
0
25
50
75
100
Percentage(%)
Feature
Promoter (<=1kb)
Promoter (1−2kb)
Promoter (2−3kb)
5' UTR
3' UTR
1st Exon
Other Exon
1st Intron
Other Intron
Downstream (<=300)
Distal Intergenic

Fig. S18. Epigenetic profiling by ATAC-seq. **(A)** Venn diagram showing the overlapping of detected ATACseq peaks between the two normal donors and the patient. (**B**) Per sample distribution of the annotated features for all the detected peaks (left) and for the consensus peaks (right) that were detected in two or more samples.

Supplementary tables

Table S1. Laboratory findings of the patient with homozygous Helios^{I325V} at 4 time-points (reference ranges, when provided, are indicated below the values in brackets).

Age at Evaluation	*7 years*	*12 years*	*13 years*	*17 years*
Blood results				
RBC, mil/µl	4.02 (3.7-5.3)	4.4	4.34 (4.5-6.2)	4.76 (4.2-5.8)
Hemoglobin, g/dL	11.5 (9.4-15.6)	11.9	12.1 (13-17)	14.3 (12-16)
Platelet, g/L	243 (150-450)	243	266 (150-410)	366 (150-400)
WBC, g/L	2.12 (4.5-13.5)	3.08	2.89 (4-11)	4.5 (4.1-10.1)
Neutrophils, g/L (%)	0.34 (16%)	1.01 (32.8%)	0.64 (22%)	0.8 (17.4%) (1.8-7.8)
Eosinophils, g/L (%)	0.02 (1%)	0.03 (1%)		
Monocytes, g/L (%)	0.13 (6%)	0.45 (14.6%)	0.32 (11%)	
Absolute Lymphocyte Count, g/L (%)	1.63 (77%)	1.58 (51.3%)	1.85 (64%)	3.1 (69.6%) (1.1-4.8)
CD3$^+$ T cells, % (cells/µl)	75 (1220) (30-78)	-	94.1 (1740) (35-78)	93.7 (2904) (58-86)

CD4⁺ T cells, % (cells/µl)	16.2 (264) (22-58)	-	19.7 (364) (22-62)	22.5 (653) (32-64)
CD8⁺ T cells, % (cells/µl)	48.2 (786) (10-37)	-	66.3 (1226) (12-32)	62.2 (1806) (13-40)
CD4/CD8	0.34 (1-4)	-	0.3 (1-3)	0.36 (>0.9)
CD16+ NK cells, % (cells/µl)	3 (49) (5-19)	-	4.8 (89) (5-19)	2.63 (76) (6-23)
CD19+ B cells, % (cells/µl)	6.5 (106) (9-38)	-	1.6 (30) (3-14)	0.19 (5.5) (4.6-21.2)
Immunoglobulin				
IgG (mg/dl)	350 (650-1410)	660 (639-1349)	-	383 (658-1837)
IgM (mg/dl)	139 (55-210)	8 (37-286)	-	10.5 (40-263)
IgA (mg/dl)	3 (83-355)	2 (42-295)	-	3.6 (71-360)
IgE (IU/l)	7.0 (up to 90)	-	-	6.5 (up to 182)
Vaccine titers				
Anti-Diphtheria	0.2	0.2		0.05
Anti-Tetanus	0.8	2.1		1.1

[1]At 17 years of age, before taking the monthly IVIG dose, the patient was tested for a large panel of autoantibodies, all being within the normal range: Anti-dsDNA, Anti-nuclear antibodies, P.ANCA (Anti-MPO), C.ANCA (Anti-PR3), Anti-SSA/Ro, Anti-SSB/LA, Anti-phospholipid IgM, Anti-phospholipid-IgG, Anti-cardiolipin IgM, Anti-cardiolipin IgG, Anti-LKM1, Anti-jo.1, Anti-RNP, Anti-TPO., Anti-Thyroglobulin, and Anti-mitochondrial antibodies.

[2]At 17 years of age, negative for EBV, CMV and HIV by Real-time PCR.

Table S2. List of homozygous, non-synonymous rare variants (minor allele frequency (MAF) <0.01 using the ExAC and gnomAD databases (*36, 37*)) found in the patient under study. The CADD score was used to predict functional damage of variants.

Gene	***Chr***	***Position***	***Reference allele***	***Alternative allele***	***Amino acid change***	***dbSNP***	***MAF (ExAC)***	***CADD score***
*ZNF142**	2	219521128	G	A	Q9*	rs200699349	0.002	33
SYTL5	X	37965931	T	A	I436N	.	0.00003	27,9
SVOPL	7	138310725	A	G	Y418H	rs142039722	0.00007	27,4
ADAMTS18	16	77325276	G	A	R1097C	rs142178461	0.0001	25,4
IKZF2	2	213872692	T	C	I325V	.	0.00005	23,5
CDH1	16	68847301	C	T	A408V	rs138135866	0.0001	23,2
PLEC	8	145009449	C	T	R349Q	.	0.0001	20,6
HYAL4	7	123516961	T	G	L400V	rs111907036	0.004	20,4
CCDC108	2	219892970	TCTC	T	E601	.	0.0004	19,85
VPS4A	16	69355000	G	A	A300T	rs370027890	0.001	17,25
CELSR2	1	109808423	T	G	L1932V	rs138787753	0.002	15,79
SLC4A3	2	220494118	A	T	H157P	rs597306	0 hom	13,58

The nonsense variant in ZNF142 (p.Q9) has not been described before, but patients with truncating mutations in ZNF142 have been described to have neurodevelopmental disorder including speech impairment, intellectual disability, dystonia and frequent seizures (*91*), none of which are experienced by our patient.

Tables S3. BioID raw data analysis

Table S4. ScRNA-seq metrics

Table S5. Markers genes of each cluster

Table S6. Differential gene expression analysis data for ScRNA-seq.

Table S7. SMART-seq metrics

Table S8. Differential gene expression analysis data for SMART-seq.

Table S9. GO term enrichment analysis of SMART-seq output

Table S10. ATAC-seq metrics and differential accessibility analysis

Table S11. List of fluorescent antibodies used for flow cytometry

Antibody-Fluorophore	***Clone***	***Producer***
CD3-APC-H7	SK7	BD Biosciences (560176)
CD4-BV605	RPA-T4	BD Pharmigen (562658)
CD4-PerCPCy5.5	RPA-T4	eBioscience (555345)
CD4-BV421	RPA-T4	BD Pharmigen (562424)
CD4-PE	13B8.2	Beckman Coulter (A07751)
CD8-V450	RPA-T8	BD Horizon (560347)
CD8-V500	RPA-T8	BD Pharmigen (560774)
CD8-PECy7	SFCI21Thy2D3	Beckman Coulter (737661)
CD8-FITC	HIT8a	BD Pharmigen (CD8-FITC)
CD16-FITC	3G8	Beckman Coulter (IM0814U)
CD19-PerCPCy5.5	HIB19	eBioscience (746457)
CD19-PECy7	J3-119	Beckman Coulter (IM3628)
CD25-PE	MA-A251	BD Pharmigen (555432)
CD25-BV605	2A3	BD Horizon (562660)
CD27-V450	M-T271	BD Pharmigen (560458)
CD45RA-AF700	HI100	BD Pharmigen (560673)

CD56-V450	B159	BD Pharmigen (560361)
CD57-PE	TB01	Thermo Scientific (12-0577-42)
TCRαβ-FITC	WT31	BD Biosciences (333140)
TCRγδ-PE	11F2	BD Biosciences (333141)
TCR vα24-PECy7	C15	Beckman Coulter (A66907)
TCRvβ11-FITC	C21	Beckman Coulter (IM1586)
CCR7-PE-CF594	150503	BD Pharmigen (562381)
CXCR5-APC	51505	R&D Systems (FAB190A)
Helios-PE	22F6	BD Pharmigen (563801)
FOXP3-APC	PCH101	Thermo Scientific (11-4776-41)
IL-2-PECy7 or FITC	MQ1-17H12	Biozym Scientific (500326)
IL4-APC	8D4-8	Thermo Scientific (12-7049-41)
IFNγ-PE	B27	Bioleged (15824129)
IL-17A-APC	N49-653	BD Pharmigen (15824129)

Table S12. Raw data file